Electronic Supplementary Material (ESI) for Physical Chemistry Chemical Physics.

Supporting information for: Singlet Fission Preserves Polarisation Correlation of Excitons

Jessica M. de la Perrelle, Patrick C. Tapping, Elisabeth Schrefl, Alexandra N. Stuart, David M. Huang, and Tak W. Kee*

Department of Chemistry, The University of Adelaide, South Australia 5005, Australia

E-mail: tak.kee@adelaide.edu.au
Phone: +61-8-8313-5314

Contents

S1 Experimental Methods

S1.1 Steady-state Optical Measurements

Steady-state absorption spectra of our samples in a 2 mm path length quartz cuvette (Starna Cells 21-Q) were obtained using a Cary Varian 1E ultraviolet-visible (UV-Vis) spectrometer. Steady-state fluorescence spectra of our samples (with absorbances of less than 0.1) in a 1 cm path length cuvette (Starna Cells 3-Q) were obtained after excitation of 590 nm by a Perkin Elmer LS 55 fluorescence spectrophotometer, with excitation and emission bandwidths of 5 nm and 15 nm, respectively. Due to the low fluorescence signal, an emission bandwidth of 15 nm was chosen and no cut-off filter was used.

S1.2 Transient Absorption Spectroscopy

The transient absorption (TA) spectrometer (Ultrafast Systems, Helios) used in this study has been described previously.[S1–S4]. An optical parametric amplifier (OPA) (Light Conversion, TOPAS-C), using the second harmonic of the signal at 1180 nm, generated the 590 nm pump pulses (∼0.50 µJ per pulse) to excite the samples. An optical chopper mechanically modulated the pump pulses at a frequency of 500 Hz, thus producing a pump pulse only every two probe pulses to obtain change in absorbance (ΔA). The polarisation of the pump was rotated to magic angle (54.7°) relative to the probe beam to negate anisotropic effects. This pump beam was focused onto the samples with a full width half maximum (FWHM) spot size of ∼0.83 mm or ∼0.82 mm for the visible or near-infrared (NIR) experiments, respectively. The probe was a white light continuum obtained by focusing a small portion of the 800 nm amplifier output onto a 3.2 mm or 12.7 mm sapphire crystal for the visible or NIR range, respectively. A computer controlled delay line was used to delay the arrival of the probe relative to the pump. The probe was split into signal and reference beams, with the signal beam focused onto the samples with a FWHM spot size of ∼0.28 mm or

$\sim$0.22 mm for the visible or NIR experiments, respectively. The linear detectors used were CMOS based in the visible region (Ultrafast Systems, CAM-VIS-2) and InGaAs for the NIR region. The samples, of $\sim$100 ppm 6,13-bis(triisopropylsilylethynyl) pentacene (TIPS-Pn) concentration, were contained in a 0.2 cm quartz cuvette (Starna Cells 21-Q-2) and stirred continuously throughout the experiment. Samples were found to degrade by less than 2% over the entire experiment, which consisted of an average of 10 scans. All experiments were performed at 21°C. All spectra were corrected for the probe's dispersion by adjusting the time-zero for the correct arrival time of the probe at each wavelength, as determined by the pump–probe coherent artefact response from the solvent (water).

The apparatus used for TA anisotropy experiments were the same as that described above. A minimum of 10 consecutive parallel and perpendicular intensity measurements were obtained by rotation of the pump polarisation using a half-wave plate. Time-resolved anisotropy was obtained at 655 nm for fluorescence and for all wavelengths in the visible range (400–800 nm) and NIR range (900–1400 nm) for TA. The measured fluorescence intensities with the emission polariser orientated parallel and perpendicular to the excitation, $I_{\parallel}$ and $I_{\perp}$, respectively, were used to calculate the time-resolved fluorescence anisotropy,[S2,S5,S6]

TA anisotropy as a function of time, t, and wavelength, λ,[S2,S7–S9] were obtained using

$$r(t,\lambda) = \frac{\Delta A_{\parallel}(t,\lambda) - \Delta A_{\perp}(t,\lambda)}{\Delta A_{\parallel}(t,\lambda) + 2\Delta A_{\perp}(t,\lambda)}, \tag{S1}$$

where $\Delta A_{\parallel}(t,\lambda)$ and $\Delta A_{\perp}(t,\lambda)$ were the change in absorbances parallel and perpendicular to the excitation polarisation, respectively.

S1.3 Nanoparticle Preparation

Stock solutions of 400 ppm TIPS-Pn, 400 ppm poly(methyl methacrylate) (PMMA) and 750 ppm poly(oxyethylene)nonylphenylether (CO-520) in freshly distilled tetrahydrofuran (THF) were prepared (Note: different concentrations of stock solutions were used for the 1:100 sample, they are given in Table S1). A volume of each stock solution (given in Table S1) was combined to make a 15 mL mixture stock solution of the desired TIPS-Pn:PMMA mass ratio. This was then rapidly injected in 75 mL of vigorously stirred water and left stirring for $\sim$5 minutes. THF was removed under reduced pressure and the remaining nanoparticle (NP) suspension concentrated down to a TIPS-Pn concentration of $\sim$100 ppm. Lastly, the samples were filtered through a 0.2 µm hydrophilic syringe filter (Sartorius Minisart NML). The approximate final concentration of each component in the NPs is given in Table S1.

Various properties of these NPs are presented in the Calculations section, including a calculation of the "average intermolecular TIPS-Pn separation" within the NPs (S4.3). The average intermolecular TIPS-Pn separation increases with increasing proportion of PMMA (refer to Table S15), ranging from 0.99 nm for the 1:0 TIPS-Pn:PMMA NP sample, to 2.15 nm for the 1:10 sample.

The resulting NP suspensions, as shown in Figure S1, were of clear blue colour with no visible aggregation when compared to TIPS-Pn in THF. No change in absorption was observed when comparing ultraviolet (UV)-visible absorption spectra taken before and after filtration through a filter (250 nm pores), as shown in Figure S2. This result confirms that the NPs were less than 250 nm in size. Hudson et al. have previously shown the effects of NP diameter on the steady-state absorption spectra of TIPS-Pn NPs.[S10] Comparing to the absorption maximum of the neat NPs

Table S1: Quantities used to prepare different TIPS-Pn:PMMA mass ratio NPs.

TIPS-Pn:PMMA mass ratio	Component	Volume used (mL)	Concentration in mixed stock (ppm)	Concentration of NPs (ppm)
1:0	TIPS-Pn	0.75	20	100
	PMMA	-	-	-
	CO-520	0.40	20	100
	THF	13.85	-	-
1:1	TIPS-Pn	0.75	20	100
	PMMA	0.75	20	100
	CO-520	0.80	40	200
	THF	12.70	-	-
1:3	TIPS-Pn	0.75	20	100
	PMMA	2.25	60	300
	CO-520	1.60	80	400
	THF	10.40	-	-
1:5	TIPS-Pn	0.75	20	100
	PMMA	3.75	100	500
	CO-520	2.40	120	600
	THF	8.10	-	-
1:7	TIPS-Pn	0.75	20	100
	PMMA	5.25	140	700
	CO-520	3.20	160	800
	THF	5.80	-	-
1:10	TIPS-Pn	0.75	20	100
	PMMA	7.50	200	1000
	CO-520	4.40	220	1100
	THF	2.35	-	-
1:100	150 ppm TIPS-Pn	0.60	6	30
	1500 ppm PMMA	6.00	600	3000
	1500 ppm CO-520	6.00	600	3000
	THF	2.40	-	-

here to the absorption maxima in that study we estimate the NP size here to be approximately 45 nm. The colloidal NP suspensions were stable for several months, likely due to the NPs being encapsulated by the surfactant, which increases the NP stability in water. However, slight oxidation and photodegradation was observed after a few days.

Figure S1: TIPS-Pn in THF (left) and 1:1 TIPS-Pn:PMMA NPs in water (right). Both have a concentration of ∼100 ppm.

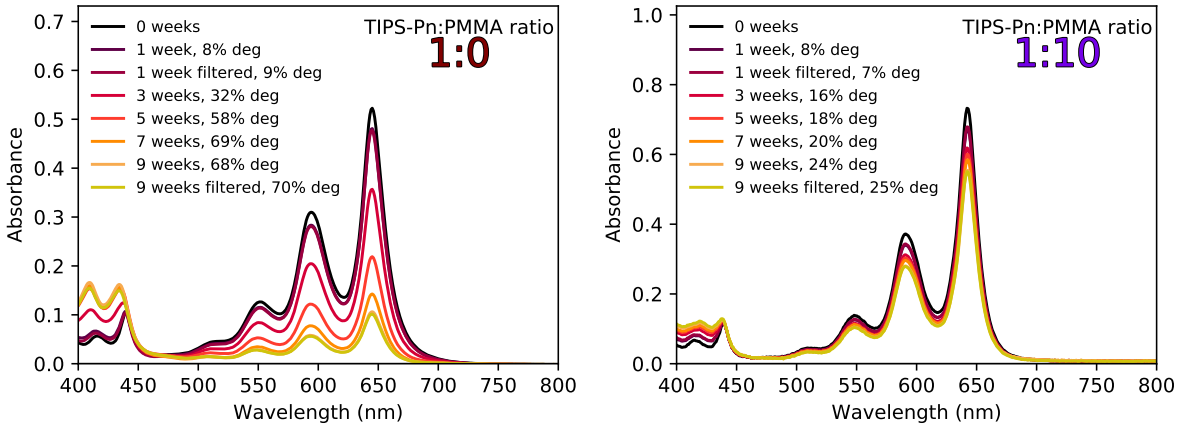

Figure S2: Degradation and colloidal stability of 1:0 and 1:10 TIPS-Pn:PMMA NPs over nine weeks.

S1.4 Polarisation Anisotropy

S1.4.1 Definition of Anisotropy

Consider a partially polarised light travelling in the x direction. The polarised component is defined as $I_z - I_y$. Anisotropy, r, of a light source is defined as the ratio of the polarised component to the total intensity I_T,

$$r = \frac{I_z - I_y}{I_\mathrm{T}} = \frac{I_z - I_y}{I_x + I_y + I_z}. \tag{S2}$$

When the light is polarised along the z-axis, the emission is symmetric around the z-axis, hence $I_x = I_y$. If we define $I_z = I_\parallel$ and $I_y = I_\perp$, we arrive at

$$r = \frac{I_\parallel - I_\perp}{I_\parallel + 2I_\perp}. \tag{S3}$$

A more detailed derivation of the anisotropy is given by Lakowicz.[S5]

S1.4.2 Excitation by Polarised Light

We now consider a sample containing randomly oriented chromophores. Upon illumination of a sample with polarised light, chromophores with absorption transition dipole moments aligned along the electric field vector of the excitation light have the highest probability of excitation. The transition dipole moment of a chromophore does not need to be precisely aligned with the electric field vector to be excited. The probability of excitation is proportional to $\cos^2\theta$, where θ is the angle between the transition dipole moment and the electric field vector of the excitation. This means excitation with polarised light results in photoexcited chromophores with absorption transition moments partially oriented along, and symmetric around, the electric field vector (refer to Figure S3). This phenomenon is termed "photoselection".

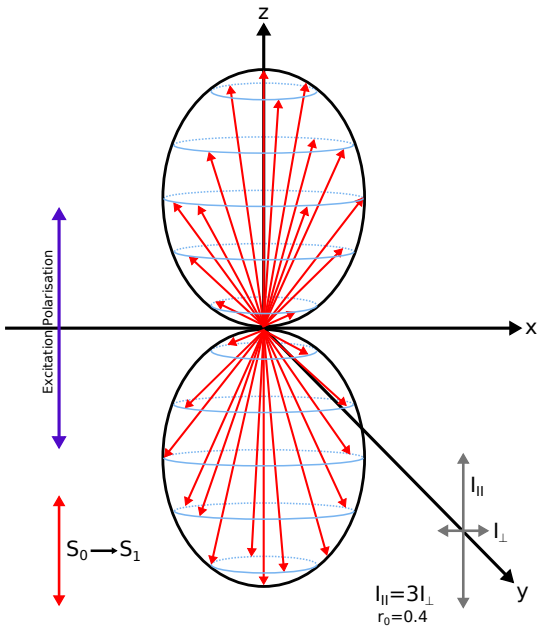

Figure S3: Initial excited-state distribution for a system with randomly orientated chromophores, upon excitation with polarised light.

S1.4.3 Anisotropy from a Homogeneous Sample

The anisotropy is given by

$$r = \left(\frac{3\cos^2\theta - 1}{2}\right), \tag{S4}$$

where θ is the angle between the excitation polarisation and the emission dipole. For random orientation of transition dipole moments with collinear absorption and emission dipoles, averaging over θ gives

$$\langle\cos^2\theta\rangle = \frac{3}{5}. \tag{S5}$$

Upon excitation with polarised light, the emission from many samples is also polarised. The extent of the polarisation of the emission relative to the excitation is described in terms of the anisotropy, r. A single chromophore, with collinear absorption and emission transition dipoles,

that is orientated along the electric field vector of the excitation has an anisotropy of 1. However, the anisotropies are always less than 1 in a homogeneous solution as it is not possible to obtain a perfectly oriented excited-state population. The observed anisotropy of the emission of randomly oriented chromophores is therefore calculated using appropriate averaged intensities based on the excitation photoselection ($\frac{2}{5}$) and the measured intensity emission from the selected chromophores. The anisotropy of emission from selected chromophores depends on the angle between the absorption and emission polarisation. The fundamental anisotropy, r_0, is the anisotropy observed in absence of any depolarisation processes (e.g. rotational diffusion or energy migration). For a sample with randomly oriented chromophores and an angle of β between absorbing and emitting dipole moment directions, the fundamental anisotropy is given by

$$r_0 = \frac{2}{5}\Big(\frac{3\cos^2\beta - 1}{2}\Big). \tag{S6}$$

A maximum anisotropy value of 0.4 occurs for fully correlated absorption and emission ($\beta = 0°$). The anisotropy takes a negative value of -0.2 if the emission polarisation is rotated 90° relative to the excitation polarisation ($\beta = 90°$). An anisotropy value of zero represents emission from completely randomly polarised chromophores, corresponding to an average β of 54.7°, known as the "magic angle".

S1.4.4 Causes of Depolarisation

By observing anisotropy over time, one can monitor the depolarisation of the excitons. As excitons become depolarised, their emission also becomes depolarised. This depolarisation from the initial excitation polarisation can occur in various ways.

A common cause of depolarisation is rotational diffusion. Consider a chromophore with collinear absorption and emission dipoles. If the chromophore rotates by some angle β before it emits, the emission from that exciton has become depolarised with respect to the initial excitation polarisation. The anisotropy is given by Equation S6. Time-resolved polarisation anisotropy measurements can thus reveal the average angular displacement of chromophores between absorption and emission. The rotational correlation time, τ_c, of a sphere is the average time for it to rotate one radian, and is given by

$$\tau_c = \frac{\eta V}{RT}, \tag{S7}$$

where η is the viscosity, T is temperature in °K, R is the gas constant, and V is the volume of the rotating unit. The angular displacement, τ_c, is related to the anisotropy by

$$r(t) = r_0 e^{-\frac{t}{\tau_c}} = r_0 e^{-6Dt}, \tag{S8}$$

where r_0 is the anisotropy at $t = 0$ and D is the rotational diffusion coefficient ($D = \frac{1}{6\tau_c}$). It is only spherical molecules which display single exponential anisotropy decay.[S5]

Therefore, by measuring the anisotropy of a sample in which only rotational diffusion occurs (i.e. no exciton migration), and in which the spherical chromophores have collinear absorption and emission dipoles, the rotational correlation time can be extracted using Equation S8. If the correlation time is much larger than the lifetime ($\tau_c \gg \tau$), then the effect of rotational diffusion is negligible, and the measured anisotropy, r, at any time, t, is equal to r_0.

Depolarisation by rotational diffusion of spheres is given by the Perrin equation:

$$\frac{r_0}{r} = 1 + \frac{\tau}{\tau_c} = 1 + 6D\tau \tag{S9}$$

where r is the anisotropy, r_0 is the fundamental anisotropy, τ is the fluorescence lifetime, τ_c is the rotational correlation time, and D is the rotational diffusion coefficient.

Another cause of depolarisation is exciton migration, such as Förster resonance energy transfer (FRET) or Dexter excitation transfer (DET). Excitons are initially correlated with the polarised excitation light. As excitons "hop" between chromophores in a disordered system, the excitons become less correlated with the excitation light (refer to the illustration in Figure S4). Measuring the exciton polarisation over time can therefore be a direct observation of the migration of excitons. The presence of energy migration can usually be predicted from the concentration of the sample, and if it is the only cause of depolarisation, time-resolved polarisation anisotropy can reveal the average rate of exciton migration.

The two processes above, rotational diffusion and exciton migration, are two common causes of exciton depolarisation. There is another, more subtle way in which anisotropy can change, namely by preferentially eliminating excitons that are more (less) correlated with the initial exciton polarisation. This selective elimination leaves a population of excitons with less (more) correlation, thus acting to decrease (increase) the overall anisotropy. An example of selective elimination of less polarised excitons can occur through diffusion-limited singlet fission (SF) in an amorphous system.

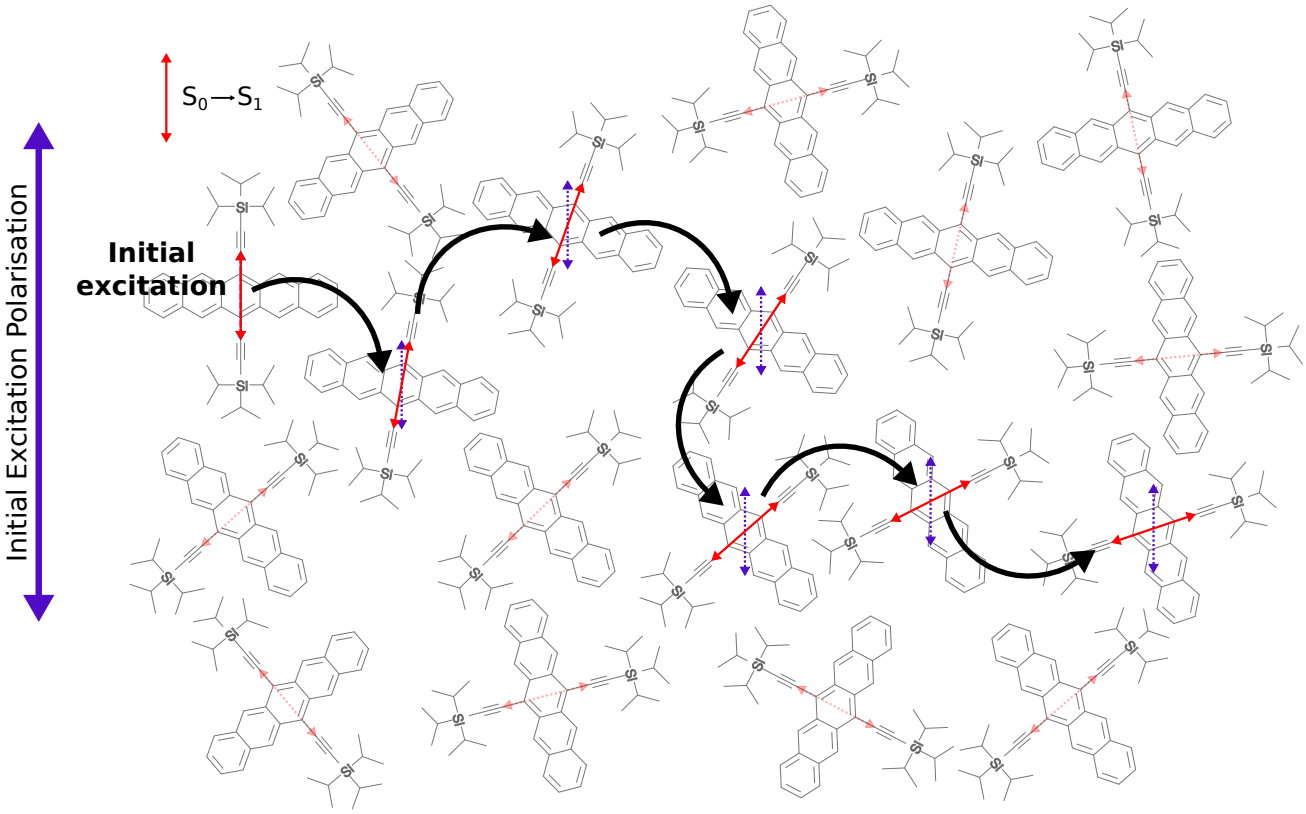

Figure S4: The schematic shows excitation of a single TIPS-Pn molecule and migration of the exciton through the system.

S2 Computational Methods

S2.1 Rate of Singlet and Triplet Migration

The non-radiative singlet energy migration rate between a donor and acceptor, k_{DA}, can be calculated using Fermi's Golden Rule,

$$k_{\mathrm{DA}} = \frac{2\pi}{\hbar} J_{\mathrm{DA}}^2 X_{\mathrm{DA}} \tag{S10}$$

where X_{DA} is the spectral overlap between the donor and acceptor and can be calculated by integrating over the product of the emission spectrum of the donor and absorption spectrum of the acceptor. J_{DA} is the transition dipole coupling term given by

$$J_{\mathrm{DA}} = \frac{\mu_0^2}{4\pi\varepsilon_{\mathrm{r}}\varepsilon_0} \frac{\hat{\mathbf{r}}_{\mathrm{D}} \cdot \hat{\mathbf{r}}_{\mathrm{A}} - 3(\hat{\mathbf{R}}_{\mathrm{DA}} \cdot \hat{\mathbf{r}}_{\mathrm{D}})(\hat{\mathbf{R}}_{\mathrm{DA}} \cdot \hat{\mathbf{r}}_{\mathrm{A}})}{|\mathbf{R}_{\mathrm{D}} - \mathbf{R}_{\mathrm{A}}|^3}, \tag{S11}$$

where μ_0 is the transition dipole moment magnitude, ε_{r} is the relative permittivity of the material, ε_0 is the vacuum permittivity, and $\hat{\mathbf{r}}_{\mathrm{D}}$ and $\hat{\mathbf{r}}_{\mathrm{A}}$ are the unit transition dipole moment vectors of the donor and acceptor molecules, respectively. $\hat{\mathbf{R}}_{\mathrm{DA}}$ is the unit vector between the pair of molecules and $|\mathbf{R}_{\mathrm{D}} - \mathbf{R}_{\mathrm{A}}|$ is the distance between the molecules. Therefore, the rate of singlet migration depends on the distance between the donor and acceptor molecules, the alignment of their transition dipoles, and their spectral overlap.

The rate of Dexter energy migration, k_{Dexter}, is given by

$$k_{\mathrm{Dexter}} = \frac{|J_{\mathrm{DA}}^2|}{\hbar} \sqrt{\frac{\pi}{\lambda k_{\mathrm{B}} T}} \exp\left[- \frac{\lambda}{4 k_{\mathrm{B}} T} \left(1 + \frac{\Delta G}{\lambda}\right)^2 \right], \tag{S12}$$

where J_{DA} is the electronic coupling between the donor and acceptor, λ is the reorganisation energy, T is temperature, k_{B} is the Boltzmann constant, and ΔG is the difference in Gibbs free energy between the donor and acceptor.

S2.2 Simulation Box

The NP systems consisted of a number of TIPS-Pn molecules, corresponding to the required TIPS-Pn:PMMA mass ratio, in a cubic simulation box with periodic boundary conditions (PBCs) enforced. The average number of TIPS-Pn molecules within a certain volume, V_{box}, is determined by

$$N_{\text{TIPS-Pn}} = \frac{V_{\mathrm{box}}}{V_{V_{\text{TIPS-Pn}}}}, \tag{S13}$$

where $V_{V_{\text{TIPS-Pn}}}$ is the average Voronoi volume of a TIPS-Pn molecule (see below for further details), and was dependent on the mass ratio of TIPS-Pn:PMMA=1:α, according to

$$V_{V_{\text{TIPS-Pn}}} = \frac{(\rho_{\mathrm{PMMA}} + \alpha \rho_{\text{TIPS-Pn}}) MW_{\text{TIPS-Pn}}}{\rho_{\text{TIPS-Pn}} \rho_{\mathrm{PMMA}} N_A}. \tag{S14}$$

A 20 nm length cubic box was used for this molecular dynamics (MD) simulation. The number of TIPS-Pn molecules to be placed into the MD simulation box for each of the TIPS-Pn:PMMA mass ratio NPs was calculated using Equations S13 and S14, and given in Table S2.

The Monte Carlo (MC) simulation was run with randomly distributed TIPS-Pn molecules and

Table S2: Average Voronoi volume of TIPS-Pn and number of TIPS-Pn molecules in the MD simulation box for each of the TIPS-Pn:PMMA mass ratio NPs.

Sample (TIPS-Pn:PMMA mass ratio $(1:\alpha)$)	**Average Voronoi volume of TIPS-Pn (nm^3), $V_{V_{\text{TIPS-Pn}}}$**	**Number of TIPS-Pn in the 20 nm MD simulation box, $N_{\text{TIPS-Pn}}$**
1:0	0.96	8322
1:1	1.85	4314
1:3	3.64	2197
1:5	5.43	1474
1:7	7.21	1109
1:10	9.89	809

systems representing different amounts of clustered TIPS-Pn molecules. A MD simulation was run to obtain a representation of these different types of clustered systems.

S2.3 Molecular Dynamics

MD is a computational method to study the physical movements of particles (generally atoms or molecules) in a system. Newton's equations of motion are used to simulate the classical interactions between particles, over timescales up to 1 µs.

Newton's equations of motion state that the force on a particle is equal to its mass times its acceleration, where the acceleration is given by the second derivative of the particle's position. Mathematically, for N particles this is represented as

$$\mathbf{F}_i(\mathbf{r}^N) = m_i \frac{\mathrm{d}^2\mathbf{r}_i}{\mathrm{d}t^2} = -\nabla_i \mathbf{U}(\mathbf{r}^N), \tag{S15}$$

where $\mathbf{F}_i$ is the force vector on particle i, $\mathbf{r}^N$ is the position of the particles, m_i is the mass of particle located at $\mathbf{r}_i$, and $\mathbf{U}$ is the function called the force field.

The force field describes the potential energy surface for all interacting particles, and is generally a sum of bonded and non-bonded particle interactions

$$U = U_{\text{VDW}} + U_{\text{ES}} + U_{\text{bond}} + U_{\text{angle}} + U_{\text{dihedral}}, \tag{S16}$$

where U_{VDW} and U_{ES} are the non-bonded van der Waals (VDW) and electrostatic (ES) interactions. U_{bond}, U_{angle} and U_{dihedral} are the bond stretch, bond angle and dihedral angle potentials, respectively.

The positions of particles can be found by numerical integration of Equation S15, with the period of integration (termed "timestep") chosen to be faster than the fastest phenomena within the system.

S2.4 Coarse-grained Method

Often, MD uses fully atomistic models in which each atom in a molecule is mapped to a particle. A coarse grained model is one which simplifies the system by reducing the number of particles while retaining large-scale physical properties and behaviour. Coarse-graining also eliminates the most rapid degrees of freedom, such as C–H bonds, allowing a longer integration timestep. Fewer particles results in less particle interactions needing to be calculated, and thus the efficiency of the MD simulation can be enhanced because larger systems or longer simulation times can be achieved for the same computing resources. An example of an atomistic to coarse-grained mapping is shown in Figure S5.

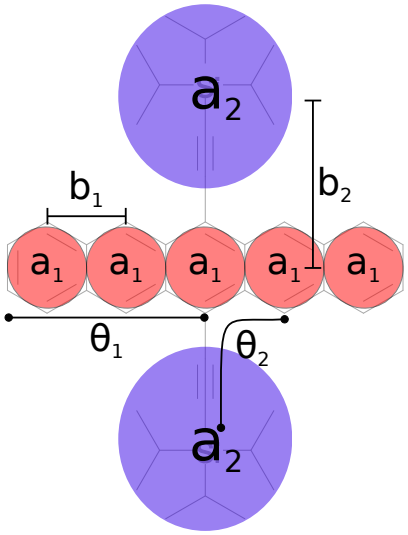

Figure S5: The atomistic to coarse-grained mapping of TIPS-Pn for the MD simulation. Parameters for the non-bonded, the harmonic bond length and the bond angle potentials are given in Tables S3, S4 and S5, respectively.

S2.5 Obtaining TIPS-Pn Input Geometries from Molecular Dynamics Simulations

We required input positions and transition dipole moments of TIPS-Pn molecules for our MC simulation. TIPS-Pn molecules were assumed to be randomly distributed in the NP systems by Stuart et al.[S4] However, it is possible that during the NP formation TIPS-Pn-TIPS-Pn or PMMA-PMMA interactions are favoured, driving some degree of phase separation and so TIPS-Pn molecules could form a more "clustered" distribution within the NPs.

We used MD to crudely simulate clustering of TIPS-Pn molecules during the formation of the NPs. These simulations were performed with the MD simulation package LAMMPS. Rather than a fully atomistic model of TIPS-Pn molecules, we used a coarse-grained model in which a TIPS-Pn molecule was represented by five spherical beads corresponding to the centre of mass of the benzene rings of pentacene (Pn) and two spheres for the triisopropylsilylethnyl (TIPS) groups. The transition dipole moments were defined as the unit vector between the centre benzene ring to one of the TIPS groups. This atomistic to coarse-grained mapping is illustrated in Figure S5.

The bond lengths and angles were represented by a harmonic potential, with the equilibrium bond length/angle and corresponding force constant for the bonded/angle potentials given in

Tables S4 and S5. Non-bonded intramolecular interactions were turned off so Lennard-Jones (LJ) interactions were only calculated between molecules.

The coarse-grained system representing a pure TIPS-Pn NP was run under constant temperature and pressure conditions (NPT ensemble). The homonuclear LJ diameter, σ_{ii}, and homonuclear LJ interaction strength, ε_{ii}, were optimised to achieve a constant volume corresponding to the density of pure TIPS-Pn. The resulting parameters are given in Table S3

Molecules are initially placed at random inside a 20 nm cubic box. The system was simulated at 298 K and 1 atm with PBC enforced to simulate the larger NP system. Langevin dynamics were used in the MD simulation to model an implicit solvent, with the dampening factor set to 1 fs. It roughly represents the PMMA matrix in the NP system.

Overlapping atoms from the randomly input TIPS-Pn molecules were removed by performing an energy minimisation, and thus used as a more realistic representation of "randomly distributed" TIPS-Pn molecules for the MC simulation.

A series of soft potentials were used to equilibrate the system. A LJ force field (parameters given in Table S3) was then applied to the TIPS-Pn molecules to simulate their clustering during NP formation. The MD simulation does not aim to be a true representation of the dynamics of TIPS-Pn molecules during NP formation. Instead, the aim was to obtain representations of different amounts of "clustered" TIPS-Pn molecules in the final NP systems. Consequently, the positions and transition dipole moments were extracted from the MD simulation at various timesteps (corresponding to different degrees of clustering) and used as input for the MC simulation.

Table S3: Parameters used in the non-bonded potential, $U_{\mathrm{non-bonded}}(r_{ij}) = 4\varepsilon_{ij}[(\sigma_{ij}/r_{ij})^{12} - (\sigma_{ij}/r_{ij})^{6}]$, where σ_{ii} is the homonuclear LJ diameter and ε_{ii} is the homonuclear LJ interaction strength.

Site	m ($\mathrm{g\,mol^{-1}}$)	σ_{ii} (Å)	ε_{ii} ($\mathrm{kcal\,mol^{-1}}$)
a_1	55.27	1.5	3.3
a_2	181.37	1.5	3.9

Table S4: Parameters used in the harmonic bond length potential, $U_{\mathrm{bond}}(l) = k_l\frac{(l-l_0)^2}{2}$, where l_0 is the equilibrium bond distance and k_l is the force constant for the bonded potential.

	l_0 (Å)	k_l ($\mathrm{kcal\,mol^{-1}\,Å^{-2}}$)
b_1	2.41	1000
b_2	4.8	100

Table S5: Parameters used in the harmonic bond angle potential, $U_{\mathrm{angle}}(\theta) = k_\theta\frac{(\theta-\theta_0)^2}{2}$, where θ_0 is the equilibrium bond angle and k_θ is the force constant for the angle potential.

	θ_0 (°)	k_θ ($\mathrm{kcal\,mol^{-1}\,rad^{-2}}$)
θ_1	180	1000
θ_2	90	1000

S2.6 Rate Constants for Singlet Migration, Singlet Fission and Singlet Decay

Singlet migration occurs through a FRET process in our model. The singlet migration rate constant used in this MC simulation, k_{DA}, is given in Equation S10.

The hopping rate, k_{DA}, depends on the transition dipole coupling term, J_{DA}, given in Equation S11. This depends on the relative permittivity, ε_{r}, of the 1:α TIPS-Pn:PMMA NP (α ranges from 0 to 10), which was approximated by the weighted average of the permittivities of TIPS-Pn and PMMA,

$$\varepsilon_{\mathrm{r}} = \varepsilon_{\text{TIPS-Pn}}\left(\frac{1}{1+\alpha}\right) + \varepsilon_{\mathrm{PMMA}}\left(\frac{\alpha}{1+\alpha}\right), \tag{S17}$$

where $\varepsilon_{\text{TIPS-Pn}}$ and $\varepsilon_{\mathrm{PMMA}}$ are the relative permittivity of TIPS-Pn and PMMA, respectively. Approximate values for these parameters were taken from literature,[S11–S13] and are given in Table S6.

Table S6: MC simulation parameters.

Parameter	Symbol	Value
Density of TIPS-Pn	$\rho_{\text{TIPS-Pn}}$	$1.104\,\mathrm{g\,cm^{-3}}$
Density of PMMA	ρ_{PMMA}	$1.188\,\mathrm{g\,cm^{-3}}$
Relativity permittivity of TIPS-Pn	$\varepsilon_{\text{TIPS-Pn}}$	3.0
Relativity permittivity of PMMA	$\varepsilon_{\mathrm{PMMA}}$	2.25

A simple model for SF was employed in our MC simulation, as the microscopic details of SF are not yet fully understood.[S14] We assumed SF occurred with a rate k_{SF} if a singlet molecule had a ground-state molecule within a distance of r_{SF}. Mathematically, we described the rate of SF by

$$k_{\mathrm{SF}}^{D,A} = k_{\mathrm{SF}}\Theta(r_{\mathrm{SF}} - r^{D,A}), \tag{S18}$$

where D and A denote the "donor" singlet molecule and "acceptor" ground-state molecule, respectively. $r^{D,A}$ is the distance between those two molecules and Θ is the Heaviside step function. The "SF radius", r_{SF}, was defined as the maximum distance between a donor and acceptor in order for SF to occur. In this model, $k_{\mathrm{SF}}^{D,A} = k_{\mathrm{SF}}$ if $r^{D,A} \leq r_{\mathrm{SF}}$ and $k_{\mathrm{SF}}^{D,A} = 0$ if $r^{D,A} > r_{\mathrm{SF}}$.

The singlet decay rate constant, k_{d}, was taken from the intrinsic lifetime of singlets from time-correlated single photon counting (TCSPC) data of dilute TIPS-Pn in THF.[S4] Therefore,

$$k_{\mathrm{d}} = \frac{1}{12}\ \mathrm{ns^{-1}}. \tag{S19}$$

The event which occurred at a given step in the MC simulation (hopping, SF or decay) was chosen by considering the probability of each event happening in a random time interval, Δt. If k is the probability of a transition occurring per unit time, the probability of the transition *not* happening in a time interval, Δt, is given from Poisson statistics as $P(t) = \exp(-k\Delta t)$. We can therefore define a (random) time interval, Δt, for a transition to occur via $\exp(-k\Delta t) = x$ where x is a uniform deviate, $0 \leq x \leq 1$.[S15]

Therefore,

$$\Delta t = -\frac{\ln(x)}{k}. \tag{S20}$$

A set of time intervals for hopping, SF, or decay was determined by Equation S20 where $k = \{k_{\mathrm{DA}}, k_{\mathrm{SF}}, k_{\mathrm{d}}\}$ was the set of all rate constants for the donor, and x was a random variate over [0,1] chosen for each k.

S2.7 Generation and Parameterisation of Steady-state Absorption and Emission Spectra

The singlet migration rate, k_{DA} was dependent on the spectral overlap, X_{DA}, between the donor and acceptor. This spectral overlap was calculated by integrating over the product of the emission spectrum of the donor and absorption spectrum of the acceptor.

In the MC simulation, the steady-state absorption and emission spectra of the chromophores were simulated by a Franck-Condon progression, with an intensity at detection energy, E, given by

$$I(E) = \sum_{\upsilon=0}^{\upsilon=N-1} \frac{e^{-s} s^{\upsilon}}{\upsilon!} \frac{\gamma}{\pi(\upsilon\hbar\omega - E_0)^2 + \gamma^2)}. \tag{S21}$$

Parameters are defined in Table S7. Chromophores were generated with energies from a normal distribution with a mean E_0 and standard deviation E_α.

The simulated steady-state absorption spectrum was generated by summing over the absorption spectra of all chromophores. The simulated steady-state fluorescence spectrum was generated by summing over only those chromophores which decay during the MC simulation. Both spectra were also scaled by an oscillator strength factor, μ_0^2. The energy of the chromophore was reduced by E_{relax} when calculating emission spectra. The experimental Stokes shift was reproduced by an using appropriate values for E_{relax} and E_α. E_α influences the computed Stokes shift because the Stokes shift is partially caused by the greater probability of migration to and hence the greater probability emission from lower energy sites, and E_α controls the width of the distribution of site energies.

μ_0 was obtained from literature,[S16] E_0 was set to match the 0–0 transition, E_α and E_{relax} were set to produce the most accurate Stokes shift, $\hbar\omega$ was chosen to obtain the best spacing between the peaks, s was chosen to match the peak heights of the vibronic transitions. γ was then optimised so the simulated spectra matched the experimental spectra. The simulated steady-state absorption and emission spectra are primarily used to compute spectral overlap integrals, and hence when parametrising focus was placed on the goodness of fit in the region where the absorption and emission have high overlap. The best fit parameters are summarised in Table S7, and the corresponding steady-state simulated absorption and emission spectra are given along with the experimental spectra in Figure S32.

Table S7: MC simulation parameters for the steady-state absorption and fluorescence spectra.

Parameter	Symbol	Value
Number of vibronic levels (abs)	N_{abs}	4
Number of vibronic levels (flu)	N_{flu}	2
Magnitude of transition dipole moment	μ_0	$1.171 \times 10^{-29}\,\text{Cm}$
0–0 Transition energy	E_0	1.928 eV
Standard deviation of energy	E_α	0.015 eV
Relaxation energy	E_{relax}	0.012 eV
Energy of harmonic vibrational frequency	$\hbar\omega$	0.168 eV
Vibronic linewidth (abs)	γ_{abs}	0.025 eV
Vibronic linewidth (flu)	γ_{flu}	0.080 eV
Huang-Rhys parameter (abs)	s_{abs}	0.45
Huang-Rhys parameter (flu)	s_{flu}	0.1

S2.8 Monte Carlo Simulation Structure

The coordinates and transition dipole moments of the TIPS-Pn molecules for a given mass ratio were extracted from the MD simulation and used as the input for the MC simulation. The chromophores were given a normal distribution of energies about the 0–0 vibronic transition energy, E_0, with a standard deviation of E_α.

For each relevant donor/acceptor pair, the rate constant in Equation S10 was calculated. This required calculation of the transition dipole coupling in Equation S11 and the spectral overlap X_{DA}. k_{DA} is only non-zero when the donor and acceptor are not the same chromophore and the distance between the pair was less than 10 nm. The SF rate, $k_{\text{SF}}^{D,A}$, was also determined for each donor/acceptor pair (i.e. either 0 if $r^{D,A} > r_{\text{SF}}$ or k_{SF} if $r^{D,A} < r_{\text{SF}}$). The singlet decay rate was kept constant at $k_{\text{d}} = \frac{1}{12}\ \text{ns}^{-1}$. Once these relevant rate constants for each donor/acceptor pair were determined, Δt for each could be calculated using Equation S20.

A MC process was then used to simulate the system, via repetition of a series of steps:

1. A chromophore was chosen at random to be excited to its singlet state.

2. The singlet could then hop to a new chromophore, undergo SF or decay to the ground state. The process chosen was the one with the smallest Δt.

3. If a hop was chosen, the total time was incremented by that Δt. The acceptor was then excited and step 2) is repeated for the new chromophore.

4. If singlet decay or SF was chosen, energy and time fluorescence and anisotropy histograms were populated and a new chromophore is excited. Steps 1) – 4) were repeated from 1×10^4 excitations.

To reduce computational time, if a chromophore remained excited at 2 ns, the current trajectory was stopped and a new chromophore was excited. The SF rate constant, k_{SF}, and the SF radius, r_{SF}, were input parameters of the MC simulation. To find the best fit to the experimental

fluorescence magic-angle and anisotropy data, the MC simulation was run for numerous values of k_{SF} and r_{SF} for systems with randomly and clustered TIPS-Pn distributions.

S2.9 Histogram Binning

A fluorescence event may only be observed upon singlet decay. Consequently, the fluorescence histogram should be populated by accordingly binning the emission spectrum of the chromophores on which singlet decay occurred. The anisotropy histogram should also be binned upon a singlet decay. The numerator of the anisotropy is given by $\frac{1}{2}I_0(3\cos(\theta)^2 - 1)$, where θ is the angle between the transition dipole moments of the initially excited chromophore and the chromophore decaying, and I_0 is the fluorescence intensity of the decaying chromophore. The denominator of the anisotropy is the total fluorescence intensity.

However, the singlet decay rate was $\frac{1}{12}$ ns^{-1}, meaning decay events were infrequent. Consequently, binning only at decay events would require an enormous amount of excitations to obtain statistically valid results. As the fluorescence signal is proportional to the singlet exciton population, it is valid to instead populate the fluorescence histogram bins at all times up until the exciton is lost through SF or radiative decay. Using this method reduced the number of excitations required to produce reliable data. The fluorescence histogram bins were populated using the emission spectrum of the chromophore the singlet was on at the time. The anisotropy histogram was binned in a similar way, with θ the difference between the transition dipole moment of the initially excited chromophore and the chromophore the singlet was on at the time, and I_0 is the fluorescence intensity of that chromophore. The histogram bin corresponding to a decay or SF event was only populated with a fraction of the corresponding fluorescence or anisotropy.

The anisotropy was scaled by 0.4 to account for the photoselection phenomenon observed in the experimental results. By selection of a wavelength from the two-dimensional (2D) simulated fluorescence and anisotropy histograms, fluorescence and anisotropy kinetics could be generated to compare to the experimental data.

S3 Results

S3.1 Steady-state Absorption

The UV-visible absorption spectra of the different TIPS-Pn:PMMA NPs, along with pure TIPS-Pn in THF, are shown in Figure S6. The absorption spectrum of TIPS-Pn in THF has vibronic peaks at 650, 590 and 550 nm representing the $S_0 \rightarrow S_1$ 0–0, 0–1, and 0–2 vibronic transitions. The smaller series from 440 nm represent the $S_0 \rightarrow S_2$ transitions. These peaks are slightly red-shifted in the TIPS-Pn:PMMA NPs, with the red-shift decreasing as the amount of PMMA is increased. This trend suggests that the TIPS-Pn molecules become more "solution-like" as the amount of PMMA increases (i.e. the average intermolecular TIPS-Pn separation decreases). Additionally, the amplitude of the vibronic transitions tend towards that of the isolated chromophores in solution, similarly observed in a previous study of pentacene NPs.[S17]

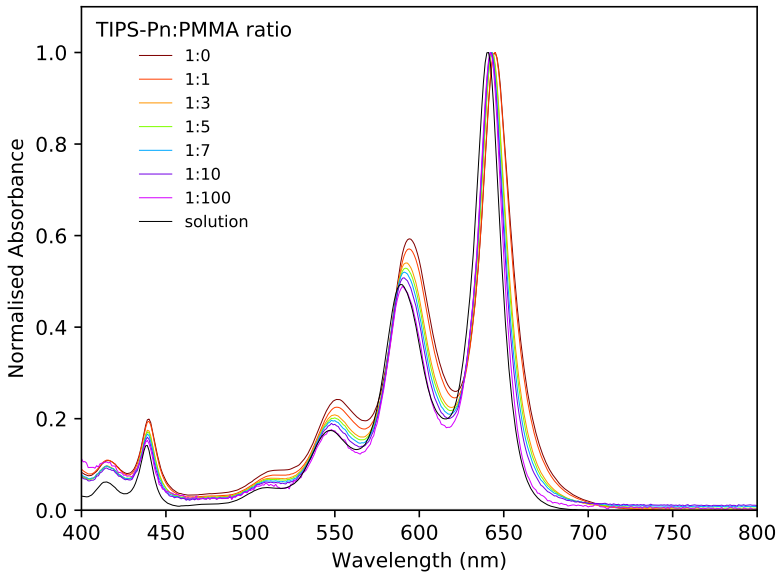

Figure S6: Steady-state UV-visible absorption spectra of the NPs with different TIPS-Pn:PMMA mass ratios and pure TIPS-Pn in THF. All spectra have been corrected for PMMA scattering.

Previous studies on TIPS-Pn have shown that the type of molecular packing and strength of coupling between molecules affect the steady-state spectra.[S18,S19] The absorption spectrum of crystalline TIPS-Pn appears significantly different to that of amorphous TIPS-Pn.[S18,S20–S22] The similarity of the TIPS-Pn:PMMA NPs absorption spectra to that of TIPS-Pn in THF suggests relatively weak electronic coupling between TIPS-Pn molecules, implying they were arranged amorphously throughout the NPs. No additional peaks at 700 nm, which are representative of aggregation features, are observed. We therefore conclude that our NPs did not form significant amounts of strongly coupled chromophores and that a negligible amount of TIPS-Pn molecules were arranged in a slip-stacked brickstone packing motif as found in crystalline TIPS-Pn films.[S23–S25] We have further confirmed that this method of TIPS-Pn NP preparation leads to amorphous packing using powder x-ray diffraction in a previous study.[S20]

The mass ratio and densities of TIPS-Pn and PMMA can be used to calculate an "average intermolecular TIPS-Pn separation", d, in each NP (See Section S4.3). These values are given in Table S8 and are representative values which can be used to compare the average separation of

TIPS-Pn molecules across the NP samples of different TIPS-Pn:PMMA mass ratios. We emphasise that this is only an *average* separation, and the molecules were not necessarily evenly spaced throughout the nanoparticle. We similarly note that although our nanoparticles were largely amorphous, this does not necessarily mean than the molecules are randomly distributed. The NPs may have instead consisted of amorphous clusters of TIPS-Pn, as is discussed in the main text. Regardless of the amount of clustering, the overall trend of average intermolecular separation with proportion of PMMA in Table S8 is the same. Clustering may change the median d, but the average d will remain the same no matter what the distribution of TIPS-Pn molecules is.

Table S8: Range of different TIPS-Pn:PMMA mass ratios used to prepare NPs and the corresponding average intermolecular TIPS-Pn separation, d.

Sample(TIPS-Pn:PMMA)	**Average intermolecular TIPS-Pn separation, d** (nm)
1:0	0.99
1:1	1.23
1:3	1.54
1:5	1.76
1:7	1.93
1:10	2.15

S3.2 Steady-state Fluorescence

Steady-state fluorescence spectra of the different TIPS-Pn:PMMA NPs are shown in Figure S7. Upon excitation at 590 nm, fluorescence was detected with a peak at ∼650 nm and a slight shoulder ∼710 nm, reflecting the 0–0 and 0–1 vibronic transitions, respectively. To correct for varying concentrations of the NP samples, the fluorescence intensity was corrected for the fraction of light absorbed by dividing the fluorescence intensity by the absorption at 590 nm. It can therefore be seen that decreasing the average intermolecular TIPS-Pn separation decreases the steady-state fluorescence intensity, with negligible change in spectral shape.

The steady-state fluorescence spectra were collected from NP samples with a less than 0.1 absorbance. Therefore, self-absorption in these NP samples was minimal and cannot account for the trend we observe in the steady-state fluorescence intensity. The quenching of the steady-state fluorescence intensity as the average intermolecular TIPS-Pn separation is decreased must therefore be due to an increase of a non-radiative decay, namely SF, pathway competing with fluorescence, as has been discussed in a previous study.[S4]

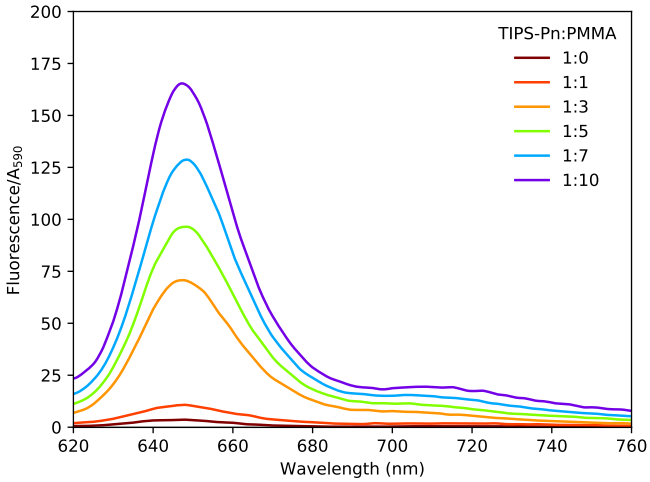

Figure S7: Steady-state fluorescence of the TIPS-Pn:PMMA NPs. To account for varying concentrations, the fluorescence was divided by the 590 nm absorption peak.

S3.3 Multi-exponential Fits of Time-resolved Fluorescence of TIPS-Pn:PMMA NPs

Table S9: Fitting parameters for the time-resolved fluorescence data of the TIPS-Pn:PMMA NPs.[a]

Sample	A_1[b]	τ_1 (ps)	A_2	τ_2 (ps)	A_3	τ_3[†] (ps)
1:0	1.00±0.05	2.6±0.2	-	-	-	-
1:1	0.87±0.05	3.3±0.4	0.13±0.05	32±17	-	-
1:3	0.73±0.03	5.3±0.5	0.22±0.03	67±19	0.04±0.01	12000
1:5	0.70±0.03	5.3±0.5	0.21±0.03	148±44	0.09±0.01	12000
1:7	0.61±0.02	5.2±0.5	0.29±0.02	296±75	0.09±0.02	12000
1:10	0.37±0.02	7±1	0.47±0.02	426±77	0.16±0.02	12000

[a] Data fitted to a multi-exponential function $I(t) = \sum_n A_n e^{-t/\tau_n}$ with an instrument response function (IRF) of 0.45 ps. [b] Normalised amplitudes so $\sum_n |A_n| = 1$. [†] Fixed to the intrinsic singlet lifetime. Unconstrained parameters are shown with a 90% confidence interval.

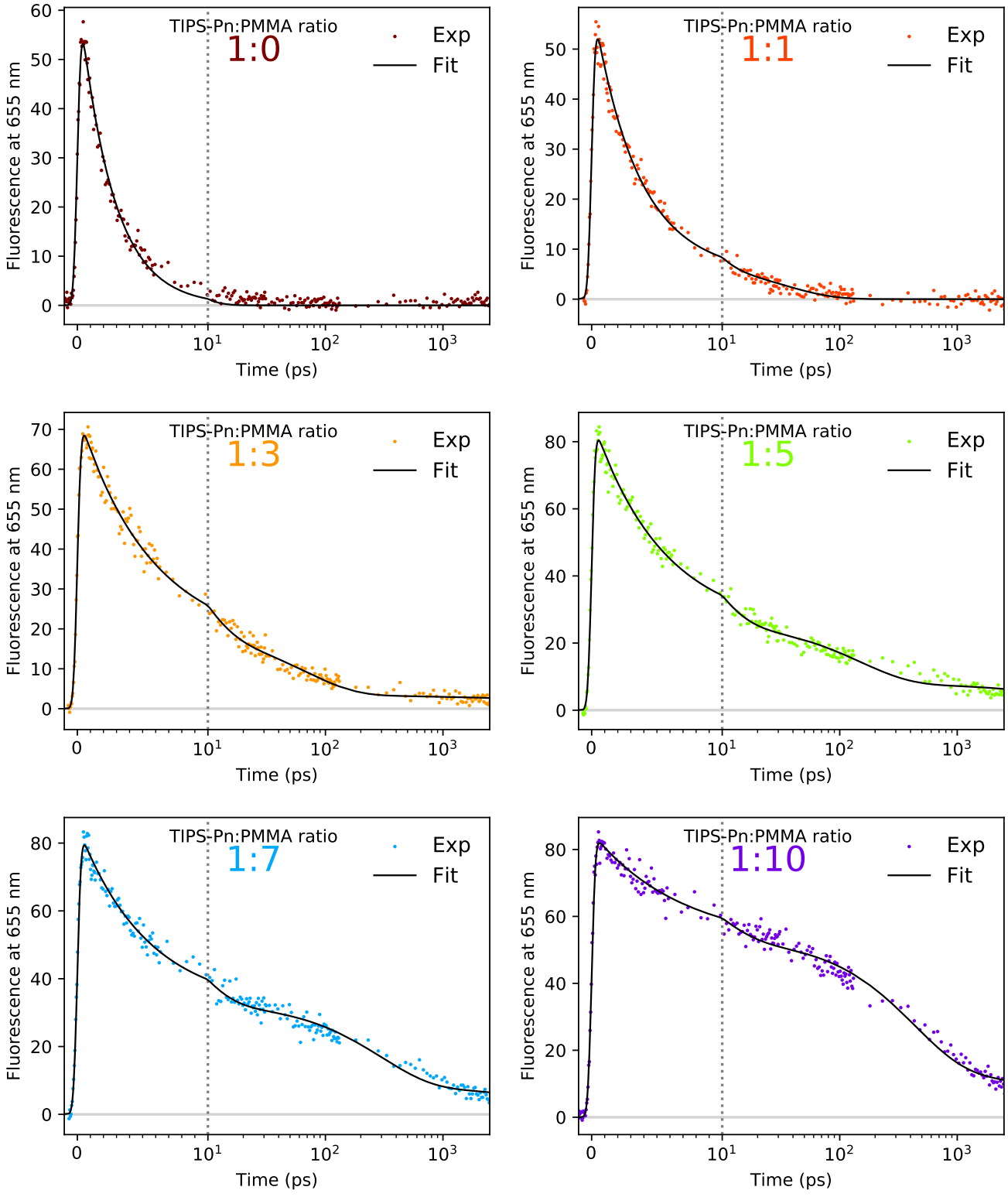

Figure S8: Fitted time-resolved fluorescence data for the TIPS-Pn:PMMA NPs. Experimental data are shown as coloured points, and the multi-exponential fits as the solid black curves. Fit parameters are given in Table S9. The dotted grey vertical lines indicate a change from a linear to logarithmic time scale.

S3.4 Time-resolved Fluorescence Anisotropy

The fluorescence intensity is detected parallel, $I_{\parallel}$, and perpendicular, $I_{\perp}$, to the excitation polarisation. The correlation of the fluorescence emission at some time, t, after the initial excitation is described by anisotropy, $r(t)$, given by

$$r(t) = \frac{I_{\parallel}(t) - I_{\perp}(t)}{I_{\parallel}(t) + 2I_{\perp}(t)}. \tag{S22}$$

We note that the rotation of the excitation polarisation from vertical to horizontal caused slight changes in power incident on the sample due to the differing reflectivities of mirrors when using s- or p-polarised light. This power difference was measured and the perpendicular intensity scans were multiplied by 0.954 before the fluorescence anisotropy was calculated using Equation S22.

Due to the photoselection phenomena in a sample with randomly oriented chromophores, the maximum anisotropy value is 0.4 and corresponds to a fully correlated emission. An anisotropy value of -0.2 corresponds to an emission rotated by 90°. When the anisotropy is zero, the emission has lost all correlation with the initial excitation polarisation.

The initial anisotropy value, also known as the fundamental anisotropy and denoted as r_0, is slightly lower than the expected maximum value of 0.4 for randomly oriented chromophores. There are several factors which can decrease the initial measured anisotropy. Firstly, any depolarisation occurring on a timescale faster than the time resolution of the detectors can result in a lower r_0. Furthermore, the measured anisotropy requires polarisers to be precisely in the vertical/horizontal orientations. Any misalignment would result in a decrease of the measured anisotropy. A slightly lower initial anisotropy than expected does not affect the anisotropy decay dynamics, which is what will be discussed.

S3.4.1 Parallel and Perpendicular Fluorescence Traces

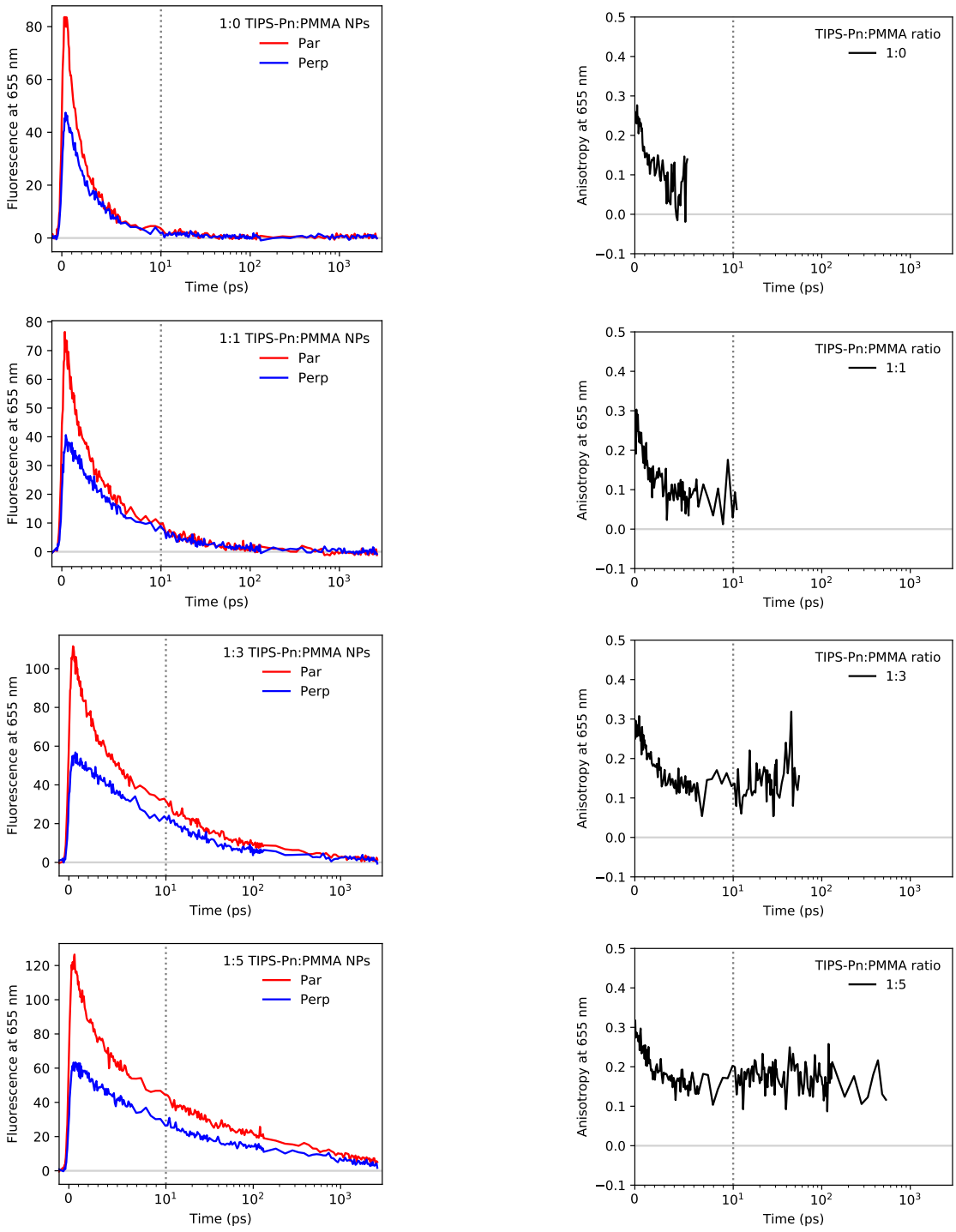

Figure S9: Fluorescence emission detected parallel and perpendicular to the excitation polarisation, and the corresponding anisotropy for the 1:0 to 1:5 TIPS-Pn:PMMA NPs.

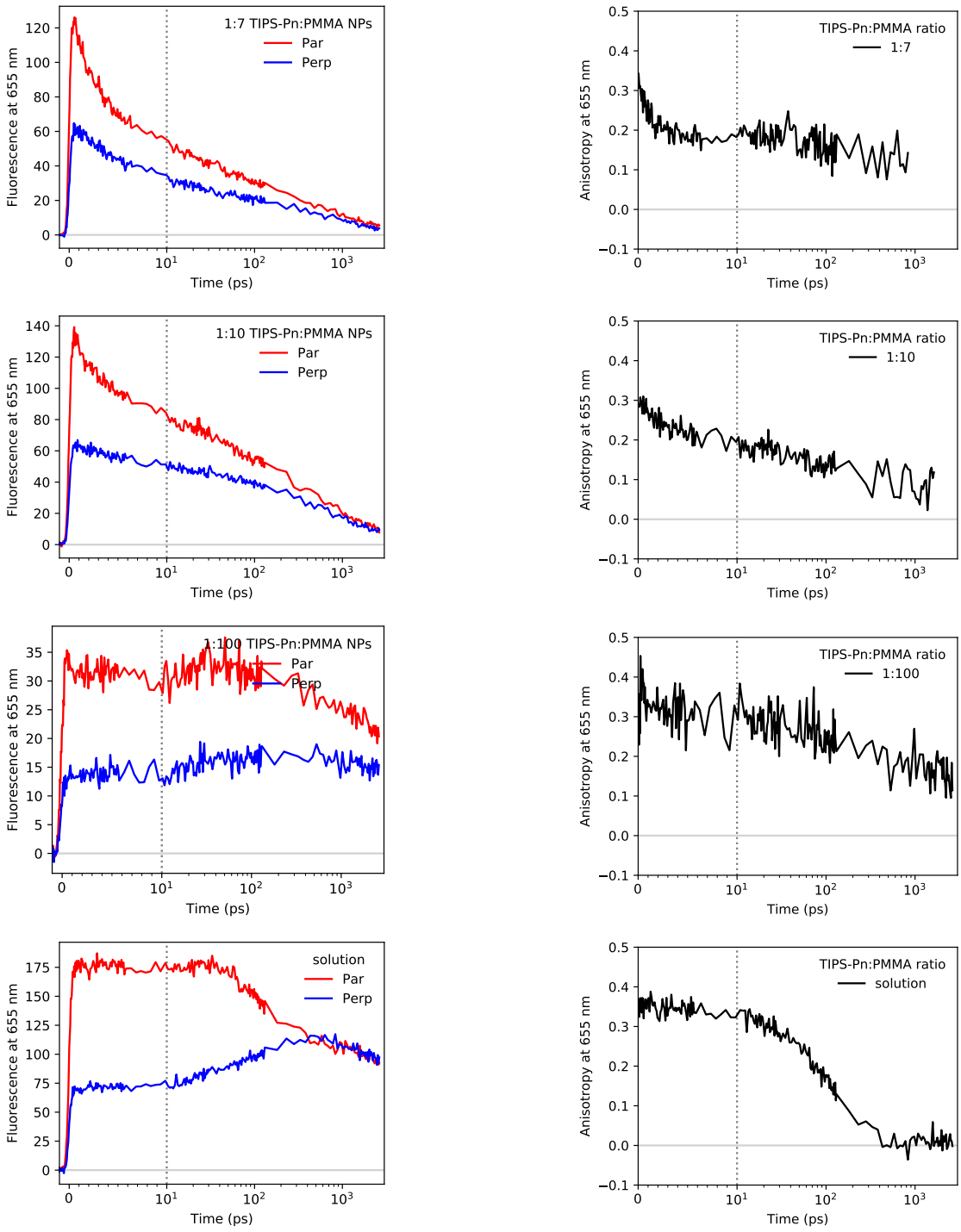

Figure S10: Fluorescence emission detected parallel and perpendicular to the excitation polarisation, and the corresponding anisotropy for the 1:7 to 1:100 TIPS-Pn:PMMA NPs as well as $\sim 10^{-4}$ M TIPS-Pn in THF.

S3.4.2 Multi-exponential Fits of Fluorescence Anisotropy of TIPS-Pn:PMMA NPs

Table S10: Fitting parameters for the fluorescence anisotropy data of TIPS-Pn:PMMA NPs and TIPS-Pn in THF.[a]

Sample	A_1 [b]	τ_1 (ps)	A_2	τ_2 (ps)	A_3	τ_3 [†] (ps)
1:0	0.80±0.09	1.5[†]	-	-	0.20±0.04	∞ [‡]
1:1	0.72±0.06	1.5[†]	-	-	0.28±0.03	∞ [‡]
1:3	0.56±0.06	1.5[†]	-	-	0.44±0.02	∞ [‡]
1:5	0.41±0.05	1.5[†]	-0.09±0.03	20[†]	0.50±0.02	1500[†]
1:7	0.41±0.05	1.5[†]	0.02±0.04	20[†]	0.56±0.02	1500[†]
1:10	0.24±0.05	1.5[†]	0.28±0.03	20[†]	0.49±0.02	1500[†]
1:100	0.29±0.08	47±48	-	-	0.71±0.07	4800±3900
solution	1.00±0.01	134±5	-	-	-	-

[a] Unconstrained parameters are shown with a 90% confidence interval. [b] Normalised amplitudes.
[†] Fixed time constants. [‡] $\tau_3 \rightarrow \infty$ indicates a constant offset in the time-resolved curve.

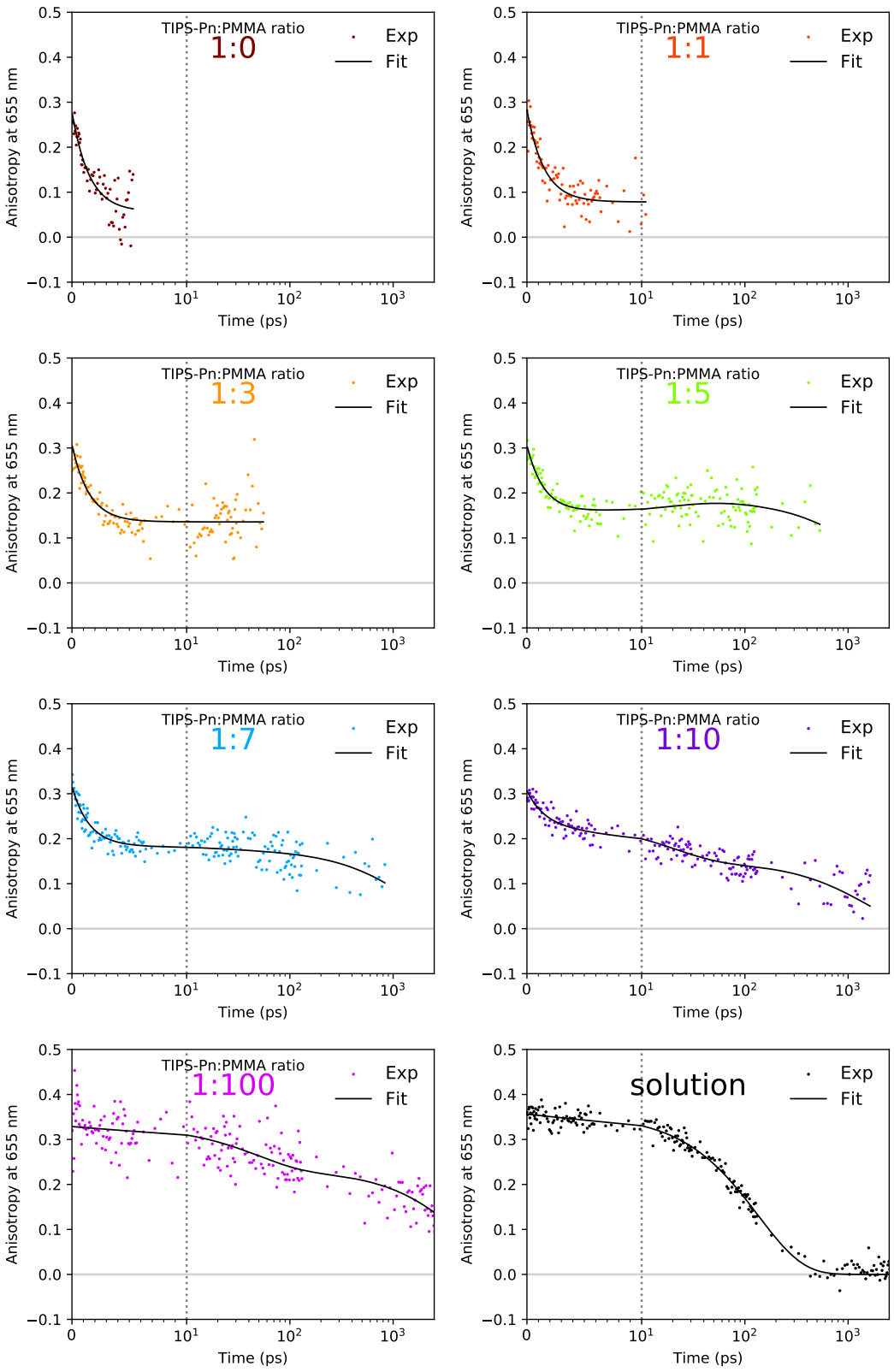

Figure S11: Fitted time-resolved fluorescence anisotropy for all TIPS-Pn:PMMA NPs and TIPS-Pn in THF. Experimental data are shown as points, and the multi-exponential fits as the solid black curves. Fit parameters are given in Table S10. The dotted grey vertical lines indicate a change from a linear to logarithmic time scale.

S3.5 Transient Absorption Spectroscopy

While the bulk of the analysis of this paper was on time-resolved fluorescence and fluorescence anisotropy, we also performed transient absorption experiments for comparison. We excite the $S_0 \rightarrow S_1$ transition of TIPS-Pn with 590 nm and monitor the ΔA in the visible (450–800 nm) and NIR (800–1400 nm) regions. TA pump power dependence studies are given below, and we note that negligible exciton–exciton annihilation occurred for the chosen pump power of the following experiments.

S3.5.1 Visible Transient Absorption

TA on TIPS-Pn/PMMA NPs has already been described in the visible region by Stuart et al., exciting the $S_0 \rightarrow S_2$ transition of TIPS-Pn with 440 nm.[S4] As the $S_2 \rightarrow S_1$ relaxation occurs rapidly in TIPS-Pn, the excitation energy has minor impact on the exciton dynamics and decay products.[S4] However, the relaxation from $S_2 \rightarrow S_1$ changes the singlet dipole moment,[S24,S26,S27] which is not ideal for the anisotropy measurements. For completeness and consistency with the excitation wavelength for the anisotropy data, we present the TA data at magic angle for our NPs upon excitation of the $S_0 \rightarrow S_1$ transition.

Direct excitation of $S_0 \rightarrow S_1$ to the lowest S_1 vibrational state would be achieved by 650 nm. However, we did not want to obstruct our spectra at this wavelength as this corresponds to the ground-state bleach (GSB) of TIPS-Pn. We therefore excited the $S_0 \rightarrow S_1$ to a higher S_1 vibrational state with 590 nm. Thus, we cannot analyse our data between 580 and 600 nm because the excitation wavelength interferes with ΔA in this region.

The 2D TA heat maps, as well as spectra taken at various times, are presented for the different TIPS-Pn:PMMA mass ratios in Figures S12 and S13. All samples show a negative GSB around 650 nm, corresponding to the $S_0 \rightarrow S_1$ 0–0 vibronic transition seen in the steady-state absorption (Figure S6). The stimulated emission (SE) around 725 nm is most evident at early times for the NP samples with a higher proportion of PMMA, and corresponds to the weaker 0–1 shoulder in the steady-state fluorescence (Figure S7). The stronger 0–0 SE component should be close to 650 nm, therefore overlapping with the GSB. Further overlap with the GSB region occurs from positive excited-state absorption (ESA) features due to several species, dominating over the 450–650 nm region. At early times and for the NP samples with a high proportion of PMMA, there are prominent ESA peaks around 450 nm and 508 nm. These peaks have been attributed to $S_1 \rightarrow S_n$ transitions.[S28] For the 1:10 sample, the decay of the 450 nm peak reveals a peak around 475 nm and is accompanied with a rise in the ESA peak around 508 nm (refer to Figure S13). These peaks are attributed to the $T_1 \rightarrow T_3$ transition,[S29,S30]. Therefore, the rise of the $\sim$508 nm peak indicates the production of triplets.[S4,S28,S31,S32] The rise of this triplet peak occurs within 10 ps, which is too fast to be attributed to intersystem crossing (ISC), so we attribute the increase in the triplet ESA to the production of triplets by SF.

To further distinguish singlet and triplet features in the TA spectra of the TIPS-Pn:PMMA NP samples we next determined singlet and triplet TA basis spectra. Figure S14 shows the TA spectra for a solution of TIPS-Pn and the 1:100 TIPS-Pn:PMMA NPs. The concentration of the $\sim 10^{-4}$ M TIPS-Pn in THF sample was dilute enough not to undergo significant amounts of SF in 3 ns. Consequently, the TA spectrum can, over the timescale of our experiments, be considered to be due to singlets only. Although a singlet spectrum could be extracted from the dilute TIPS-Pn in THF sample, it is not a representative of a singlet spectrum in the NP environment. Hence, we turn to the 1:100 NP sample. The spectra of the 1:100 and solution sample match closely,

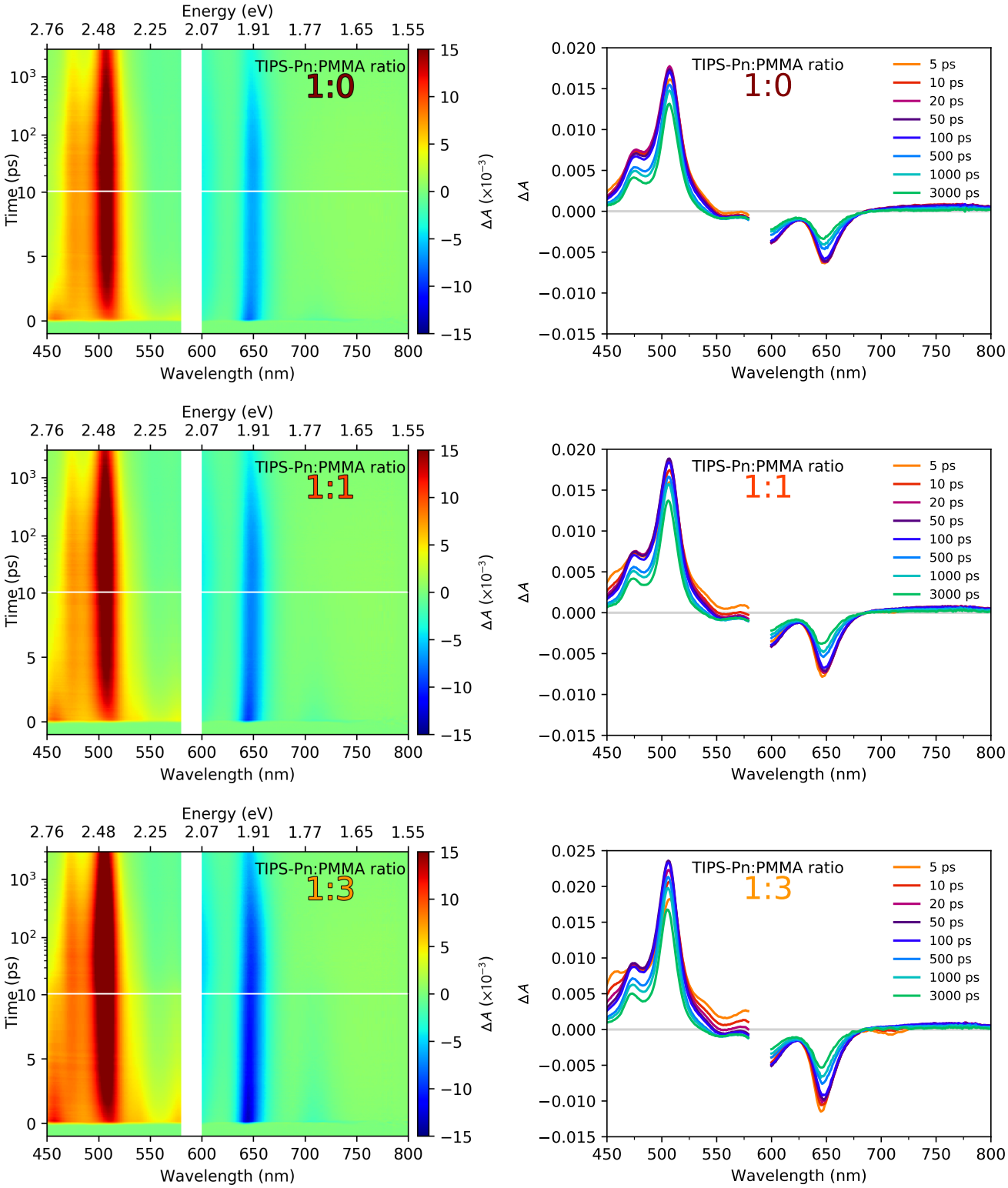

Figure S12: TA spectra for the 1:0 to 1:3 TIPS-Pn:PMMA NPs. 2D heat maps are shown on the left, with spectra taken at various times on the right. Data are cut from the 580–600 nm region due to interference with the excitation wavelength. The horizontal white lines on the left plots indicate a change from a linear to logarithmic scale.

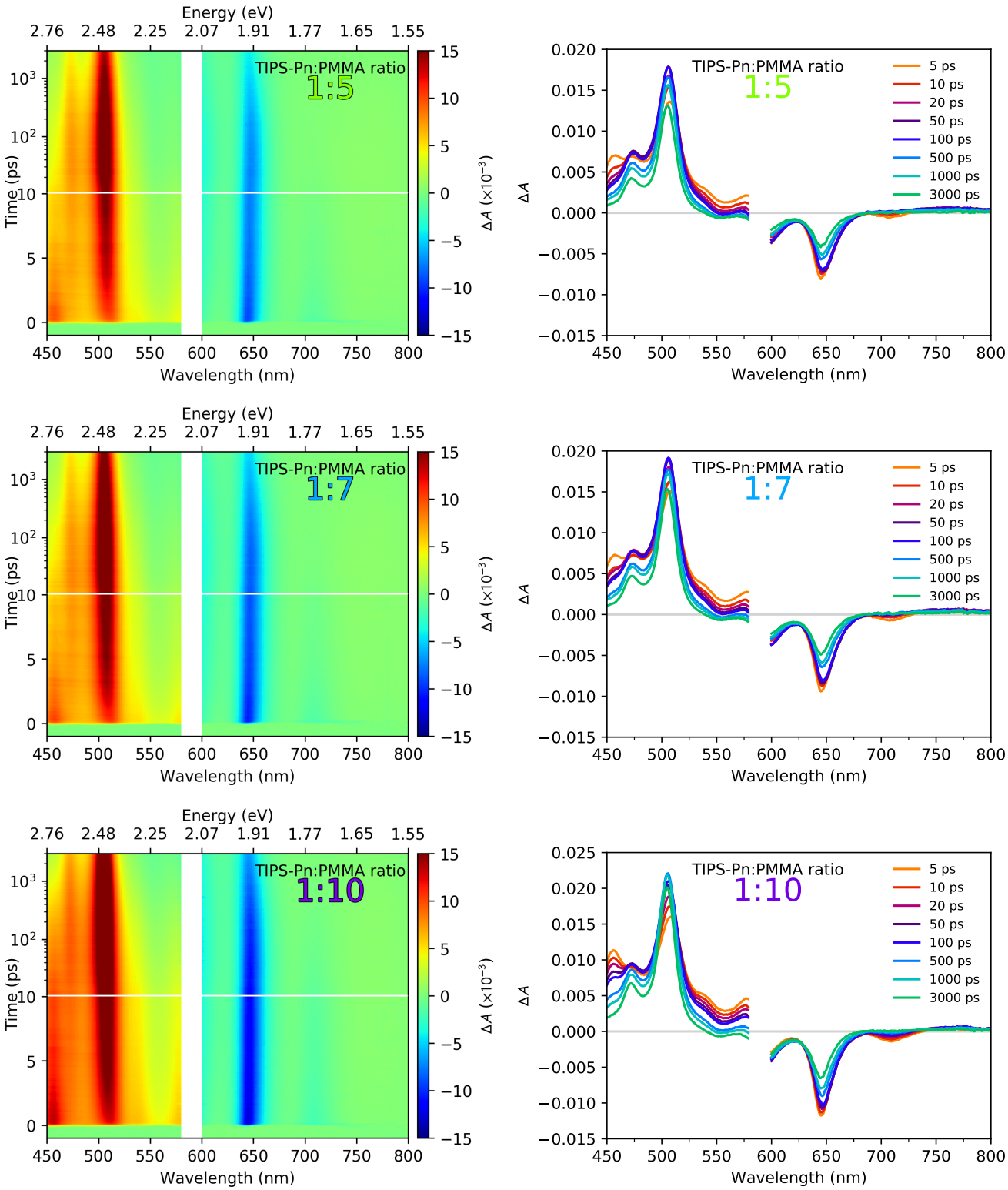

Figure S13: TA spectra for the 1:5 to 1:10 TIPS-Pn:PMMA NPs. 2D heat maps are shown on the left, with spectra taken at various times on the right. Data are cut from the 580–600 nm region due to interference with the excitation wavelength. The horizontal white lines on the left plots indicate a change from a linear to logarithmic scale.

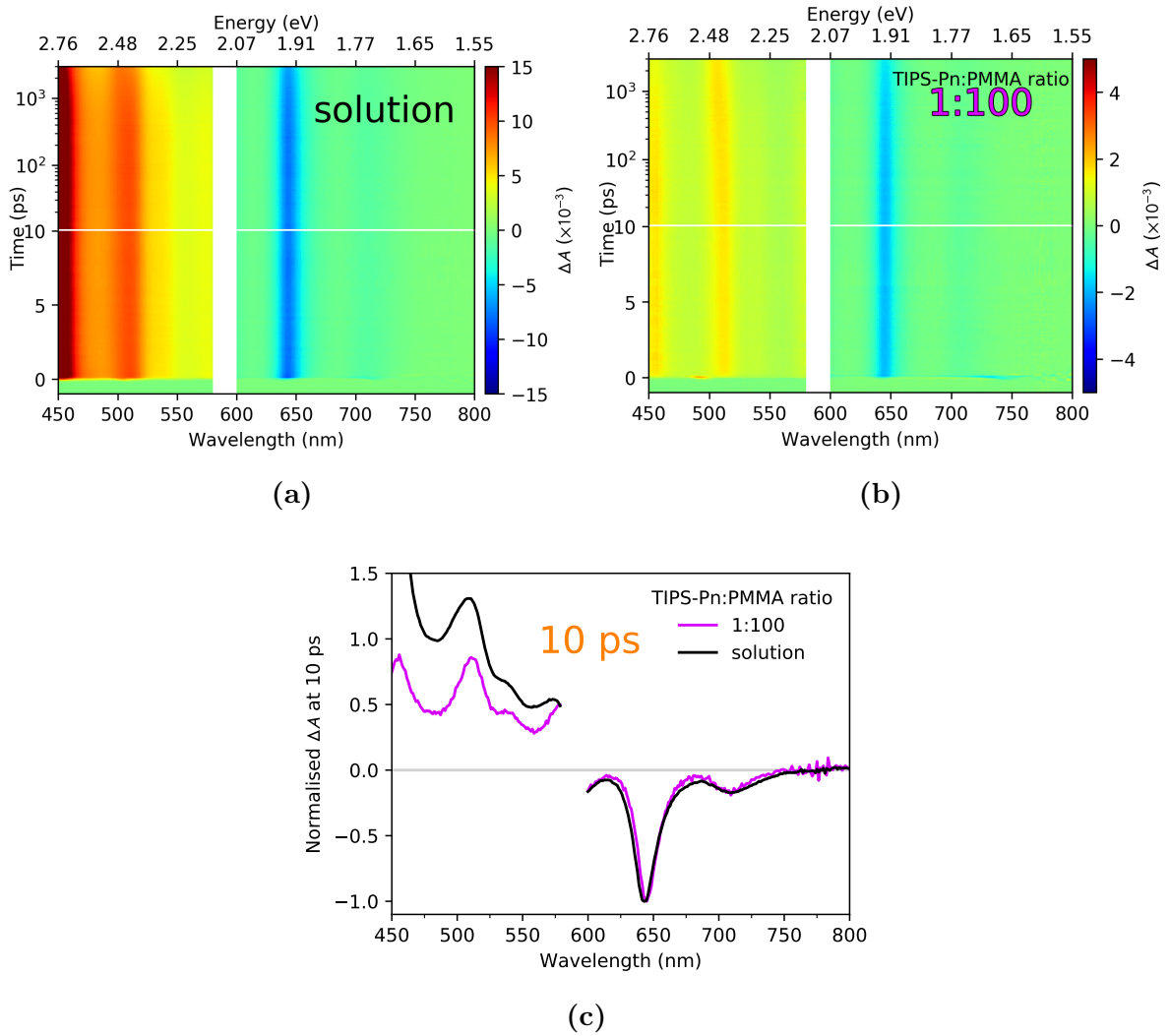

Figure S14: TA spectra for **(a)** $\sim 10^{-4}$ M TIPS-Pn in THF and **(b)** TIPS-Pn:PMMA NPs. Data are cut from the 580–600 nm region due to interference with the excitation wavelength. The horizontal white lines on these plots indicate a change from a linear to logarithmic scale. **(c)** ΔA at 10 ps for each sample, normalised to the 650 nm peak.

with subtle difference being attributed to differences in environment (PMMA versus THF). The dynamics of both samples are also nearly identical. We therefore use the 1:100 NP sample, at 10 ps, as a representative of a singlet spectrum in the NP environment. For a triplet spectrum, a sample which undergoes SF rapidly is required. For the 1:0 sample, fluorescence upconversion (UC) shows all singlets had decayed by ~50 ps. As this sample is considered to have a small enough TIPS-Pn separation for SF to occur rapidly, the TA spectrum from this time forward should be largely due to triplets. The extracted shape of the singlet and triplet contributions are shown in Figure S15. The triplet-pair intermediate, ^{1}(TT), has also been shown to have a distinct absorption spectrum for this system, but we do not attempt to characterise this here. For a more qualitative analysis of the singlet and triplet absorption spectra, (including details of the ^{1}(TT) absorption) the reader is referred to the detailed study by Stuart et al.[S4]

Referring to the shape of the extracted triplet and singlet spectra, we can now see that in each sample, the singlet features decay over time, while the triplet features grow (Figures S12

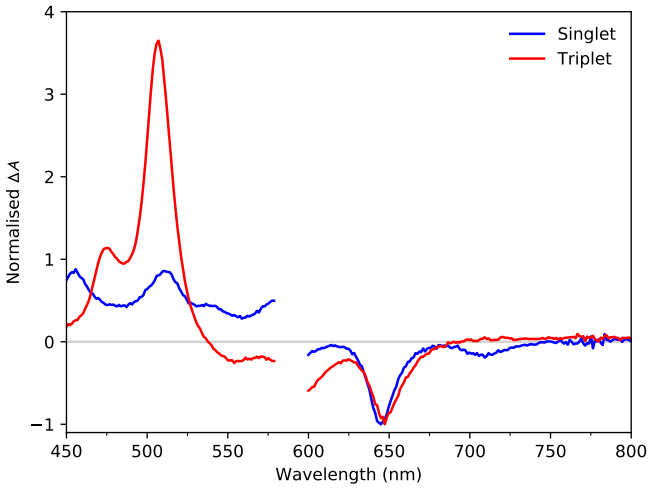

Figure S15: The singlet and triplet spectra extracted at 10 ps from the 1:100 sample and 3000 ps from the 1:0 sample, respectively. For simplicity, the GSB is incorporated into these spectra.

and S13). As the proportion of PMMA increases, the decay of singlets and concurrent rise of triplets becomes slower, indicating that singlet fission becomes, on average, slower with increasing average intermolecular separation. The slower decay of the singlet features as the average intermolecular TIPS-Pn separation increases is consistent with the increase in fluorescence lifetimes with increasing proportion of PMMA.

This trend can be seen clearly in Figure S16, which shows the spectra at 5 ps of all the TIPS-Pn:PMMA NP samples studied. It can be seen that the 1:10 sample still contains strong singlet features at this time while the 1:0 sample has already adopted a mainly triplet spectrum. This highlights the faster singlet to triplet conversion as the average intermolecular TIPS-Pn separation of the NPs decreases. The apparent isosbestic points at ∼530 and ∼670 nm are indicative of a conversion of one species to another,[S31] further supporting the conversion of singlet to triplets.

Figure S16 also labels the various contributions of each excited state species. As each wavelength has contributions from at least two different components, it is not valid to use a single wavelength as a representative kinetic trace for a single species. It is thus necessary to deconvolute the spectra into a linear combination of basis spectra of all species contributing to the TA spectra. Stuart et al. presented a detailed deconvolution of spectra to calculate SF rates and quantum yields.[S4] A comprehensive kinetic model is also presented to explain trends in SF rates and efficiency losses of our system.[S4]

The aim here is to present time-resolved fluorescence and TA data to demonstrate that SF occurred in our NPs and that it occurred faster for decreasing TIPS-Pn separation. The reader is referred to the study by Stuart et al. for quantitative SF rates and yields of the TIPS-Pn:PMMA NPs studied here.[S4]

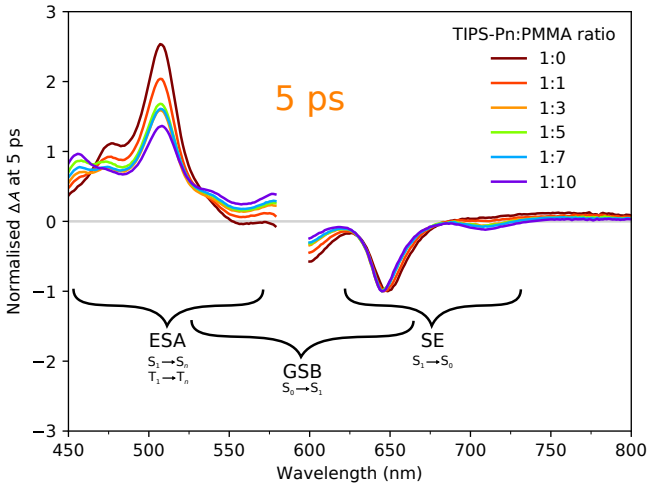

Figure S16: TA spectra at 5 ps for different TIPS-Pn:PMMA NPs. The shape of the spectra at early times is significantly different for the various average intermolecular TIPS-Pn separations. The overlapping contributions from the GSB, SE and ESA are shown.

S3.5.2 NIR Transient Absorption

In Figure S17 we present TA in the NIR region, where the singlet and triplet features are more clearly separated.[S22] As mentioned earlier, the dilute TIPS-Pn in THF sample can be a representative of a singlet spectrum. This matches the singlet spectrum for neat TIPS-Pn amorphous NPs presented by Pensack et al.[S22], and is similar to the dilute TIPS-Pn chloroform solution TA by Dvořák et al.[S33] In contrast to the broad singlet spectrum, the triplet spectrum has a distinct peak at ∼990 nm[S22] (or 970 nm in chloroform solution).[S33]

We only present the TIPS-Pn:PMMA NP samples which represent the shortest and longest average intermolecular TIPS-Pn separation, respectively, of the NPs studied. Both samples show a concurrent rise of the triplet peak at ∼990 nm and decay of the broad singlet feature at ∼1350 nm. Again, the triplet feature appears within 10 ps, too fast to be attributed to ISC. As concluded from TA data in the visible region, this is strong proof that SF is occurring in our NPs.

For the 1:0 sample, the broad singlet spectral feature at ∼1350 nm is evident immediately after the pump pulse and decays rapidly, to about half its signal, within 10 ps. The triplet feature at ∼990 nm rises instantly, reaching a peak within 10 ps and then decays slightly over the 3 ns time window. The 1:10 sample displays a strong singlet feature which lasts much longer. The triplet feature also takes longer to rise, reaching its peak only after ∼100 ps. In contrast to the 1:0 sample which has no singlet contributions after 1 ns, the 1:10 sample still shows some singlet presence at 3 ns. This suggests not all singlets have undergone SF by this time, presumably because of the larger TIPS-Pn separation, or the presence of singlet trap sites.

The NIR TA data presented here confirms the presence of SF in our TIPS-Pn:PMMA NPs, and as found from the visible TA data, SF occurs faster for NP samples with a shorter average intermolecular TIPS-Pn separation.

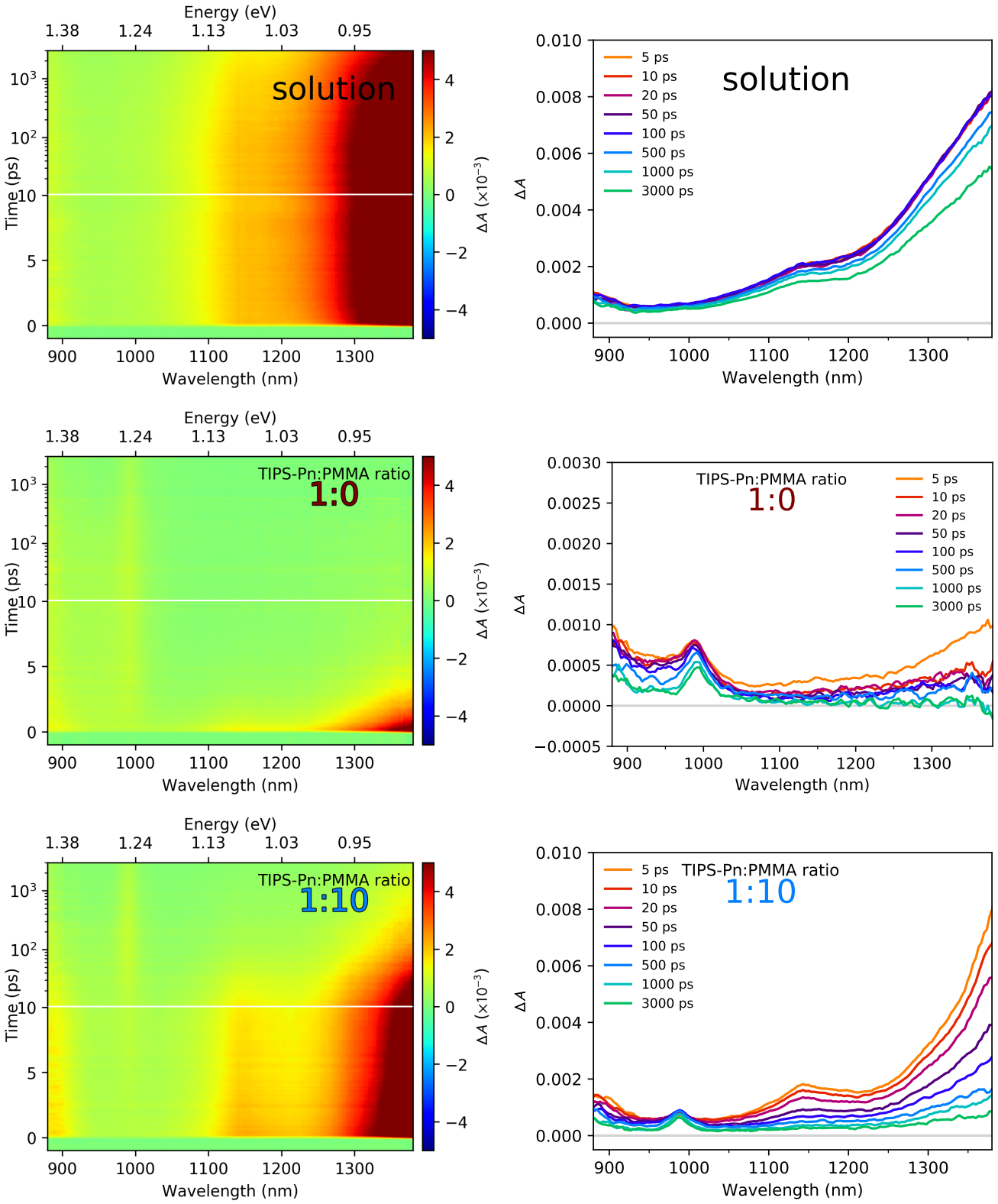

Figure S17: NIR TA spectra for $\sim 10^{-4}$ M TIPS-Pn in THF, and 1:0 and 1:10 TIPS-Pn:PMMA NPs. 2D heat maps are shown on the left, with spectra taken at various times on the right. The horizontal white lines on the left plots indicate a change from a linear to logarithmic scale.

S3.6 Pump Power Dependence

S3.6.1 Fluorescence Pump Power Dependence

For the 1:0 sample, no dependence on the pump power was observed (over 0.05–2.00 mW). This indicates that negligible singlet–singlet annihilation occurred for these pump powers. For the 1:10 sample, a very slight dependence on pump power can be observed. A pump power of 0.10 mW was chosen for subsequent time-resolved fluorescence experiments to minimise singlet–singlet annihilation contributions to fluorescence dynamics.

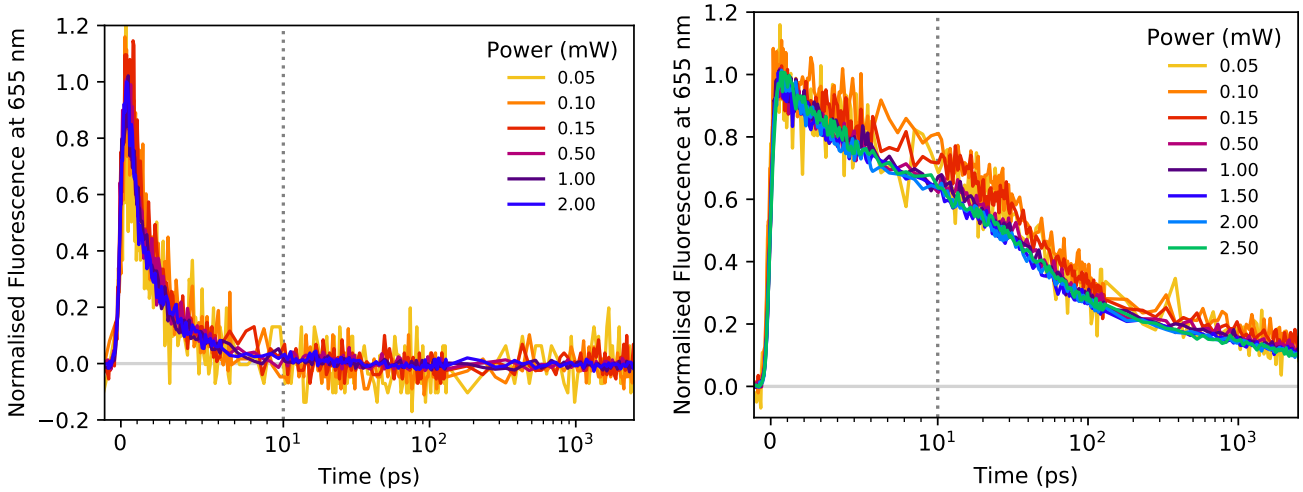

Figure S18: Pump power dependence of the fluorescence for **(a)** 1:0 and **(b)** 1:10 TIPS-Pn:PMMA NPs.

S3.6.2 Visible Transient Absorption Pump Power Dependence

For the 1:0 sample, a slight dependence on pump power can be observed for the GSB at 650 nm and ESA at 508 nm. The 1:10 sample, however, shows negligible dependence on pump power (over 0.15–2.00 mW).

A pump power dependence (i.e. an increase in exciton decay with increasing exciton concentration, or equivalently, an increasing pump power), suggests exciton–exciton annihilation was present. The 1:0 sample had the shortest average intermolecular TIPS-Pn separation, so this sample would be the most likely of all samples to show pump power dependence due to triplet exciton–exciton annihilation. Regarding singlet exciton annihilation, SF was expected to outcompete exciton–exciton annihilation for the 1:0 sample, whereas in the higher-ratio NPs, reduced SF caused longer-lived singlet excitons, which may exhibit power-dependence at high excitation densities. As no pump power dependence was evident for the 1:0 sample at 0.50 mW, we chose this pump power for our visible TA experiments to minimise exciton–exciton annihilation contributions to excited-state dynamics.

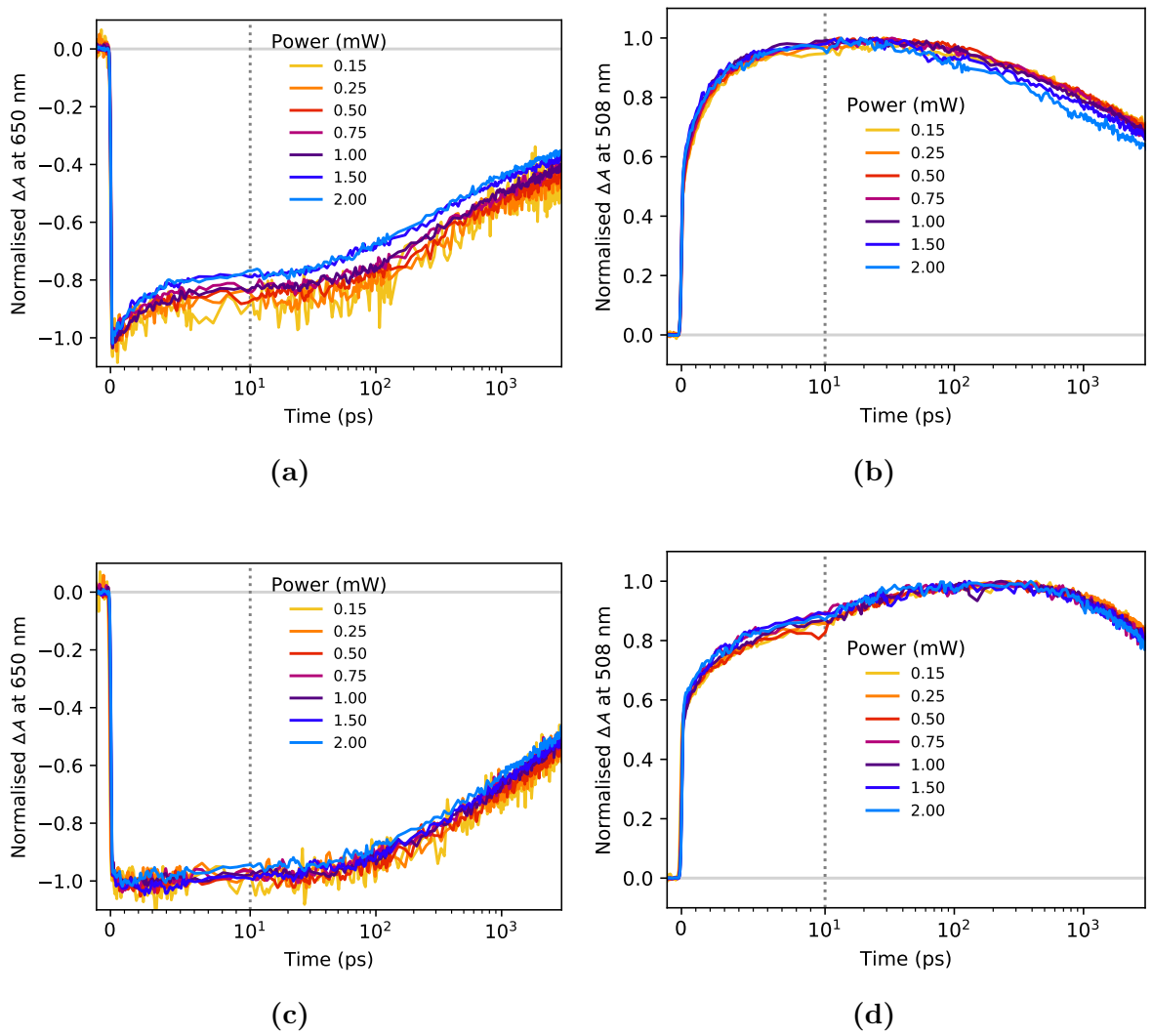

Figure S19: Pump power dependence of **(a)** the GSB at 650 nm for the 1:0 NPs, **(b)** the ESA at 508 nm for the 1:0 NPs, **(c)** the GSB at 650 nm for the 1:10 NPs, and **(d)** the ESA at 508 nm for the 1:10 NPs.

S3.6.3 NIR Transient Absorption Pump Power Dependence

Neither the 1:0 nor 1:10 samples showed pump power dependence at 1350 nm over 0.50–2.50 mW. As this ESA is due to the singlets, this confirms that negligible singlet-singlet annihilation occurred for these pump powers.

The 1:10 sample did not show pump power dependence at 990 nm (which is a peak mostly due to triplet ESA). This result suggests that the average intermolecular TIPS-Pn separation in these NPs was large enough for there to be negligible triplet–triplet annihilation. The 1:0 sample however shows pump power dependence at 990 nm, suggesting that the average intermolecular TIPS-Pn separation in these NPs is small enough for triplet–triplet annihilation to exist at higher pump powers.

A pump power of 0.75 mW was chosen for subsequent NIR TA experiments to minimise triplet–triplet annihilation contributions to excited-state dynamics.

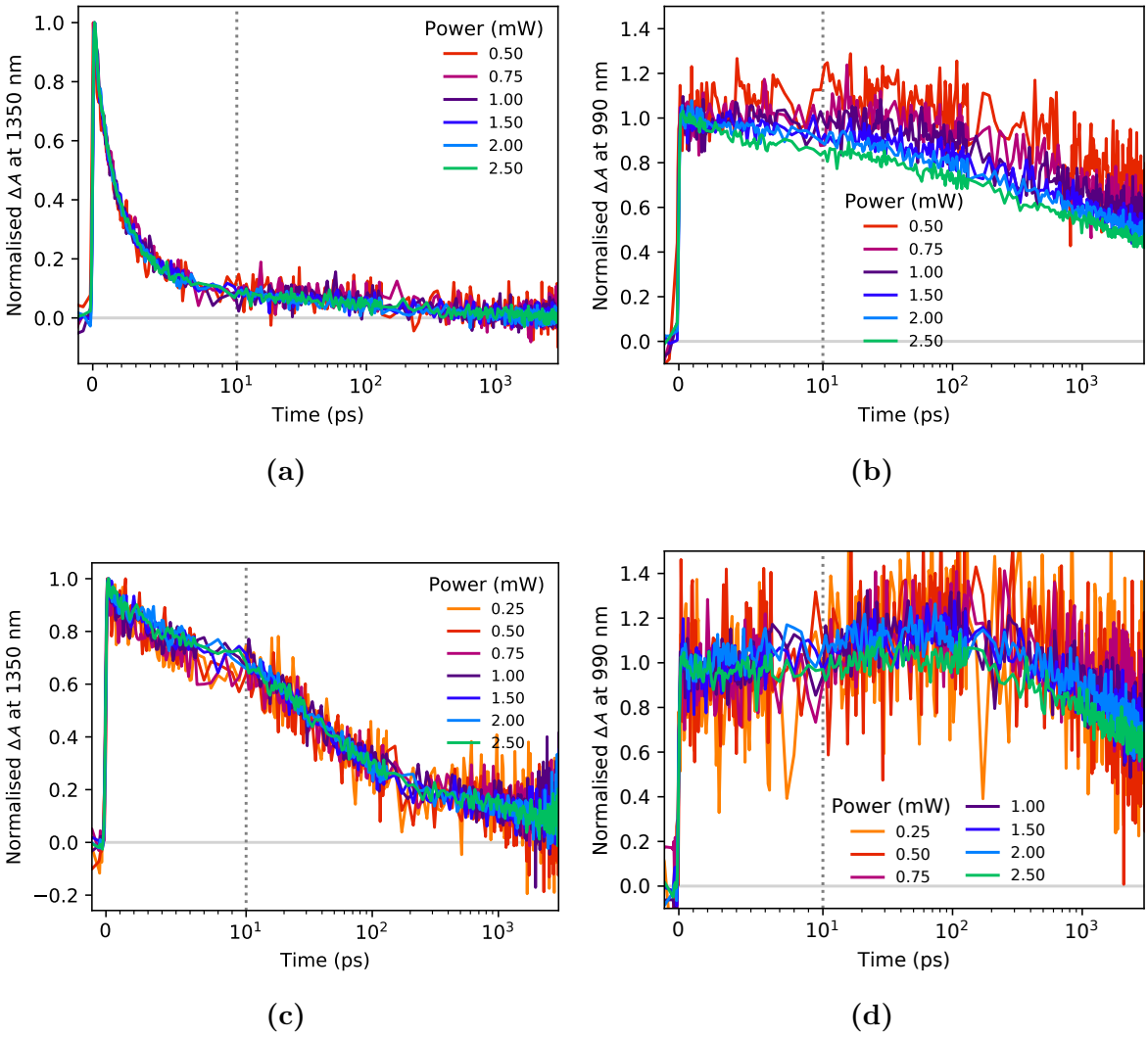

Figure S20: Pump power dependence of the TA **(a)** at 1350 nm for the 1:0 NPs, **(b)** at 1350 nm for the 1:0 NPs, **(c)** at 990 nm for the 1:10 NPs, and **(d)** at 990 nm for the 1:10 NPs.

S3.7 Pump Wavelength Dependence

For both visible and near-IR transient absorption dynamics, there was no difference between exciting at 650 nm and 590 nm. The kinetics are also consistent with visible TA data previously conducted exciting at 440 nm.[S4]

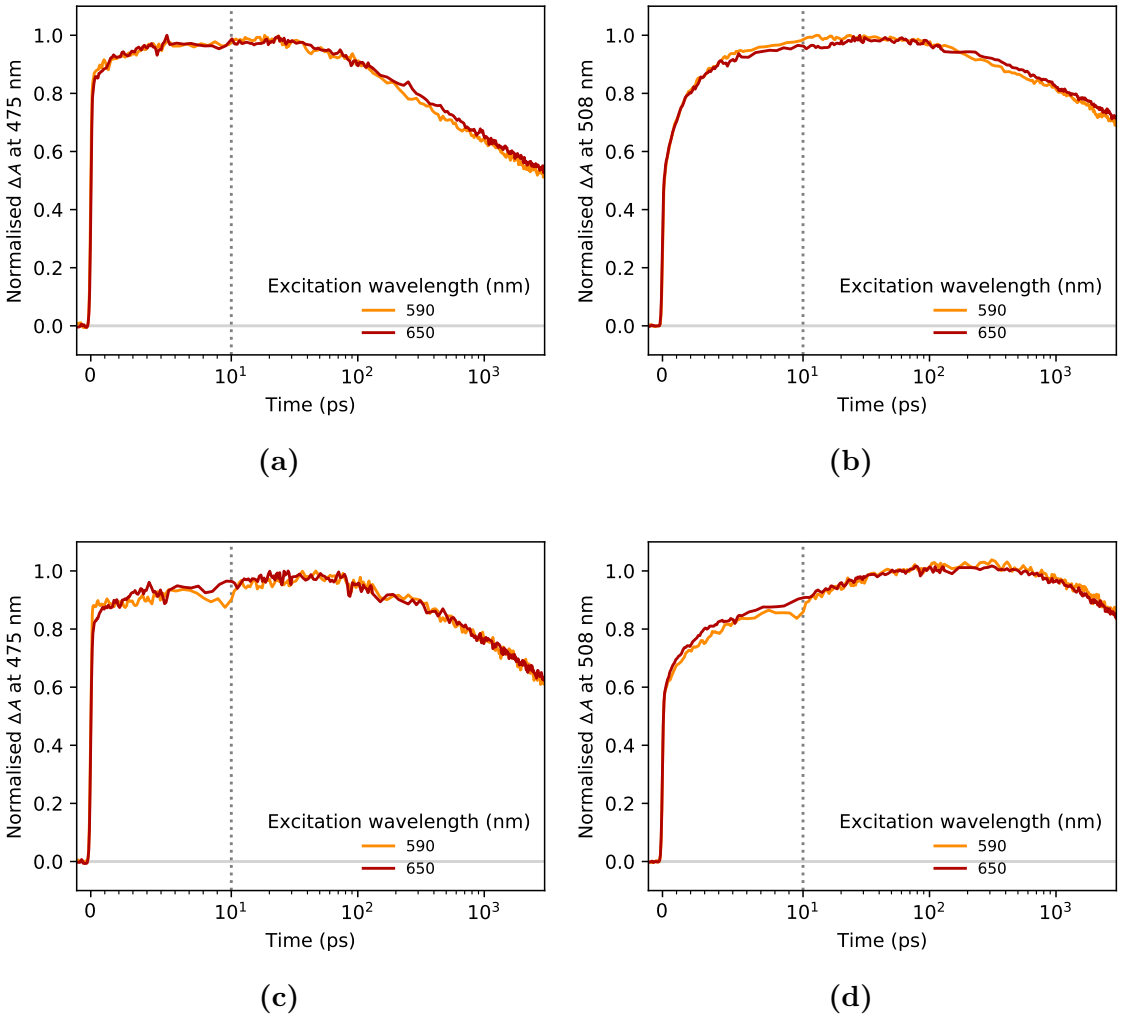

Figure S21: Pump wavelength dependence of the ESA features for **(a)** 1:0 NPs at 475 nm, **(b)** 1:0 NPs at 508 nm, **(c)** 1:10 NPs at 475 nm, and **(d)** 1:10 NPs at 508 nm. Exciting the sample at 590 nm has the same effect as exciting at 650 nm.

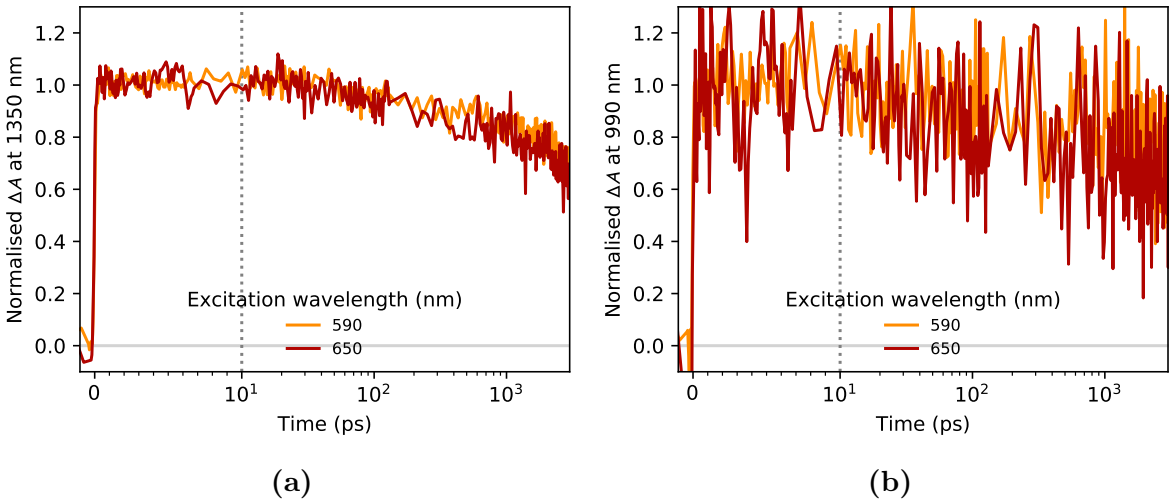

Figure S22: Pump wavelength dependence for $\sim 10^{-4}$ M TIPS-Pn in THF of the TA **(a)** at 1350 nm and **(b)** at 990 nm. Exciting the sample at 590 nm had the same effect as exciting at 650 nm.

S3.8 Transient Absorption Anisotropy

Time-dependent TA anisotropy is defined as

$$r(t,\lambda) = \frac{\Delta A_{\parallel}(t,\lambda) - \Delta A_{\perp}(t,\lambda)}{\Delta A_{\parallel}(t,\lambda) + 2\Delta A_{\perp}(t,\lambda)}, \tag{S23}$$

where $\Delta A_{\parallel}(t,\lambda)$ and $\Delta A_{\perp}(t,\lambda)$ are the change in absorbances measured when the probe and pump are polarised parallel and perpendicular to each other, respectively.[S2,S7–S9]

We note that the rotation of the excitation polarisation from vertical to horizontal caused slight changes in power incident on the sample due to the differing reflectivities of mirrors when using s- or p-polarised light. This power difference was measured and the perpendicular intensity scans were multiplied by 0.975 before the TA anisotropy was calculated using Equation S23.

Time-resolved fluorescence anisotropy gives a measure of depolarisation of singlets by monitoring the fluorescence emission at one specific wavelength. However, TA anisotropy monitors the polarisation of the ΔA for a range of wavelengths, λ, over time. The absorption spectra of excited-state species are distinct, and if ΔA at a specific λ can be assigned to just one excited-state species, then the TA anisotropy at that λ is a representation of the depolarisation of that species. As such, the TA anisotropy offers the opportunity to monitor the migration of different excited-state species (e.g. triplets).

However, in reality and in the case of our TIPS-Pn:PMMA NPs, ΔA at most wavelengths has contributions from the GSB, SE and ESA, and there is typically a lack of correspondence between λ and any one excited-state species. The TA anisotropy at a given wavelength, λ, can be described as a sum of the different contributions,

$$r(t) = f_{\mathrm{GSB}}(t)r_{\mathrm{GSB}}(t) + f_{\mathrm{SE}}(t)r_{\mathrm{SE}}(t) + f_{\mathrm{ESA}}(t)r_{\mathrm{ESA}}(t), \tag{S24}$$

where r_{GSB}, r_{SE} and r_{ESA} are the weighted average anisotropy of the GSB, SE and ESA components in the TA signal, respectively, and f_{GSB}, f_{SE} and f_{ESA} are the fraction of the GSB, SE and ESA contributions to the TA signal at a certain λ, respectively.[S34,S35]

The TA anisotropy becomes more complicated to analyse if time-dependent spectral shifts of absorption/emission bands are involved. These can arise from vibronic relaxation and/or intra- and intermolecular reorganisation processes (e.g. solvation). For example, Min et al. noticed that a red-shift in the excited state SE spectrum decreases the contribution of the excited state SE component in the overall TA signal and thus a rise in the anisotropy was observed.[S34]

In the case of our TIPS-Pn:PMMA NPs, only an insignificant amount of spectral shift was observed. Additionally, the TA anisotropy kinetics presented at a single wavelength were almost identical to those when averaged over a wavelength range (5 nm either side of the reported wavelength), confirming negligible effect of any spectral shifts that may be present.

The TIPS-Pn:PMMA NP samples were excited with polarised 590 nm light to promote TIPS-Pn from the S_0 to S_1 state. ΔA from the TIPS-Pn:PMMA NPs was detected parallel and perpendicular to the excitation polarisation. The TA anisotropy was then calculated as a function of time, t, and wavelength, λ. The anisotropy ranges from -0.2 to 0.4 as explained previously. The factors causing depolarisation include those discussed for fluorescence anisotropy.

We now present the anisotropy data of the TIPS-Pn:PMMA NP samples at two different wavelengths, 650 nm and 508 nm. We note that at ∼710 nm there is a large contribution from SE and therefore this would be an interesting region to explore the SE anisotropy decay. However, the signal strength at this wavelength was too weak to obtain meaningful anisotropy results.

Again, we note that ISC in TIPS-Pn occurs on a much longer timescale than our anisotropy experiments[S19] and therefore ISC is expected to have minimal effect on the anisotropy decay kinetics presented in this work.

S3.8.1 Parallel and Perpendicular Transient Absorption Traces

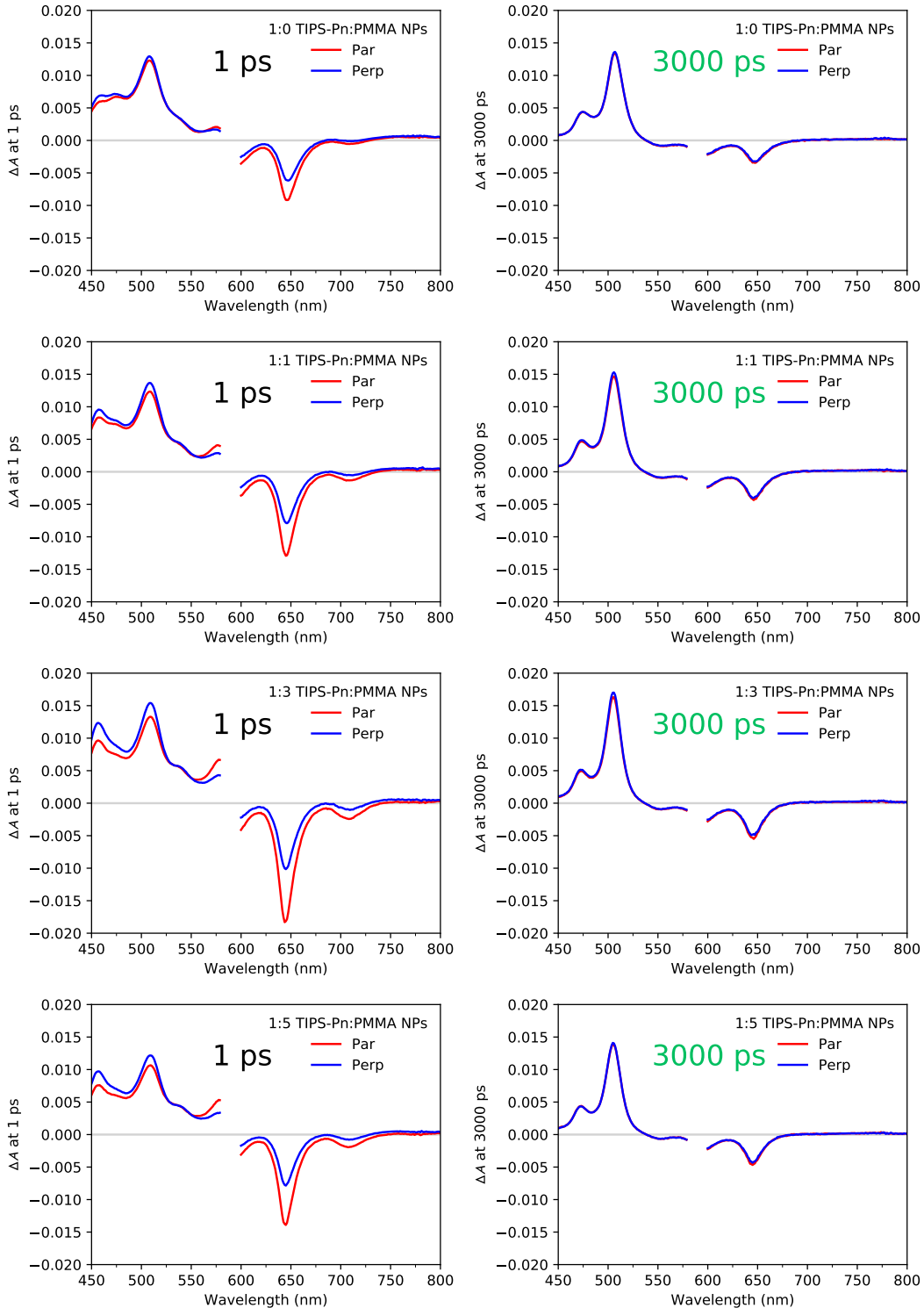

Figure S23: ΔA detected parallel and perpendicular to the excitation polarisation for the 1:0 to 1:5 TIPS-Pn:PMMA NPs.

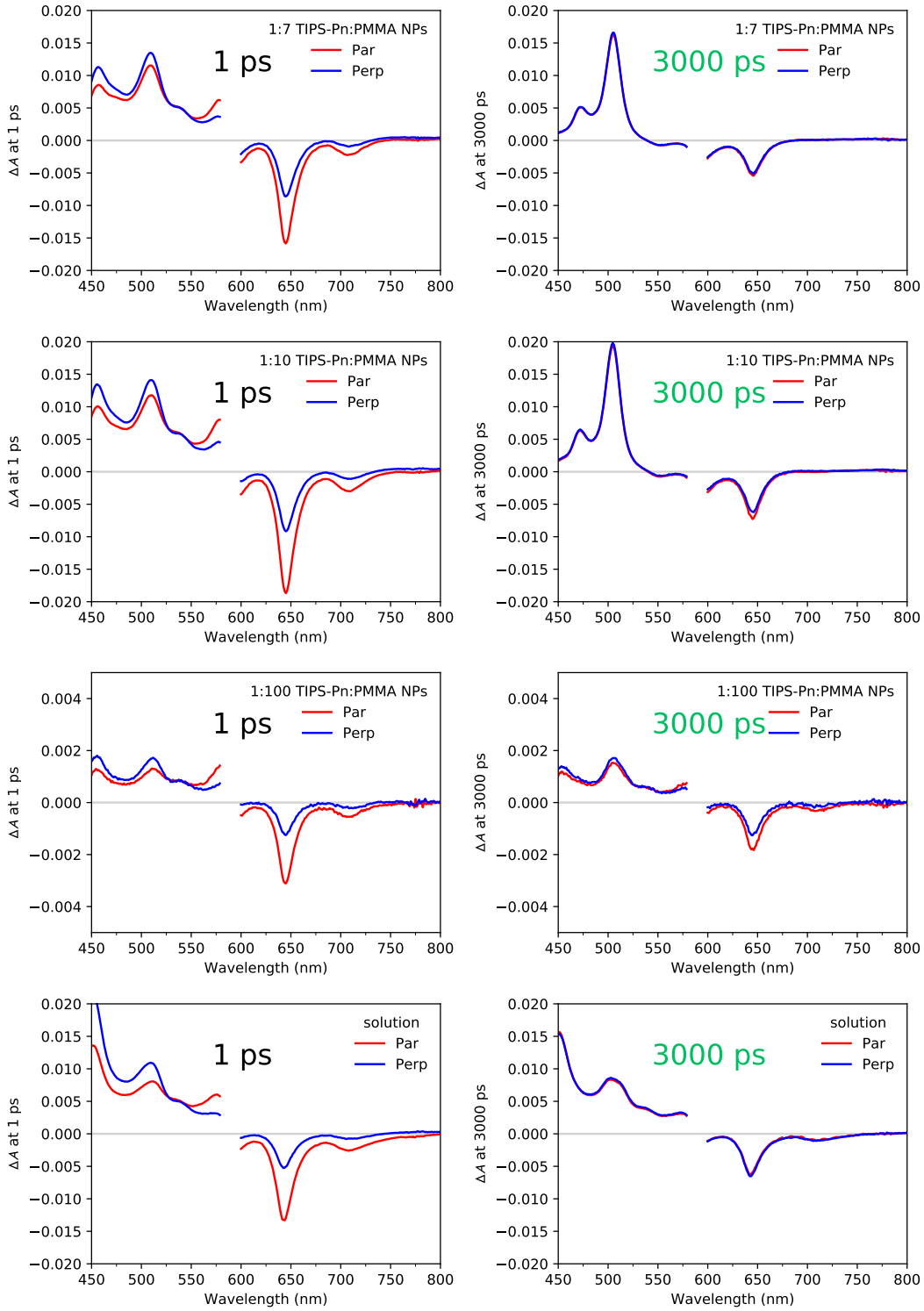

Figure S24: ΔA detected parallel and perpendicular to the excitation polarisation for the 1:7 to 1:100 TIPS-Pn:PMMA NPs as well as $\sim 10^{-4}$ M TIPS-Pn in THF.

S3.8.2 Trends in the Transient Absorption Anisotropy at 650 nm

The TA anisotropy of the TIPS-Pn:PMMA NP samples at 650 nm is presented in Figure S25. At 650 nm ΔA has contributions from GSB, SE and ESA. The experimental data are fit to a sum of exponentials, with parameters given in Table S11.

Table S11: Fitting parameters for the TA anisotropy data at 650 nm of TIPS-Pn:PMMA NPs and TIPS-Pn in THF.[a]

Sample	A_1 [b]	τ_1 (ps)	A_2	τ_2 (ps)	A_3	τ_3 (ps)
1:0	0.78±0.02	1.1±0.07	-	-	0.220±0.004	2700±200
1:1	0.69±0.03	0.93±0.08	0.14±0.03	11±3	0.165±0.005	3500±300
1:3	0.64±0.03	1.3±0.1	0.20±0.03	12±3	0.163±0.005	4600±500
1:5	0.65±0.02	1.7±0.1	0.15±0.02	38±13	0.198±0.008	7200±1500
1:7	0.62±0.02	1.9±0.1	0.18±0.02	41±10	0.206±0.008	4800±600
1:10	0.53±0.01	2.7±0.2	0.25±0.01	69±9	0.219±0.008	6500±1000
1:100	0.31±0.02	63±12	-	-	0.69±0.02	5400±500
solution	1.000±0.004	118±2	-	-	-	-

[a] Unconstrained parameters are shown with a 90% confidence interval. [b] Normalised amplitudes.

We first focus on the TIPS-Pn in THF sample. As discussed earlier, this sample underwent neither SF nor a significant amount of singlet migration. Accordingly, only singlets should have been present and the depolarisation should have only been due to the rotation of TIPS-Pn molecules in solution. The TA anisotropy of the this sample at 650 nm can be fit to a single exponential of (118 ± 2) ps, consistent with the fluorescence anisotropy. Our results are also consistent with those of Pensack et al., who measured an anisotropy decay time constant of ∼150 ps for the GSB feature of 6,13-bis(triisobutylsilylethynyl) pentacene (TIBS-Pn) in THF, with observations consistent with re-orientational dynamics of chromophores in a dilute solution.[S32] As was the case for the fluorescence anisotropy, the initial anisotropy value is below the maximum of 0.4 for reasons discussed previously.

We now focus on the 1:100 NP sample, in which SF was largely absent. The TA anisotropy of this sample fits to a sum of two exponentials. The short time constant is on the order of ∼60 ps while the long time constant is on the order of a few nanoseconds. This result is consistent with what was observed from the fluorescence anisotropy, where we attributed the time constants to singlet migration.

The anisotropy decay of the 1:0 sample can be fit to two exponentials, while those of the 1:1 to 1:10 samples were fit to three time components. These results are summarised in Table S11. The short time constant, τ_1, is ∼1 ps and it increases as the proportion of PMMA is increased, while the corresponding amplitude decreases. The intermediate time constant, τ_2, also increases slightly as the proportion of PMMA is increased. The results show that the TA anisotropy at 650 nm decays faster for NP samples with a shorter average intermolecular TIPS-Pn separation, as highlighted in Figure S26. The long time constant, τ_3, is on the order of nanoseconds. Because this time constant is significantly longer than the timescale of these experiments, no concrete conclusions can be made. It is possible that this time constant represents slow singlet or triplet migration.

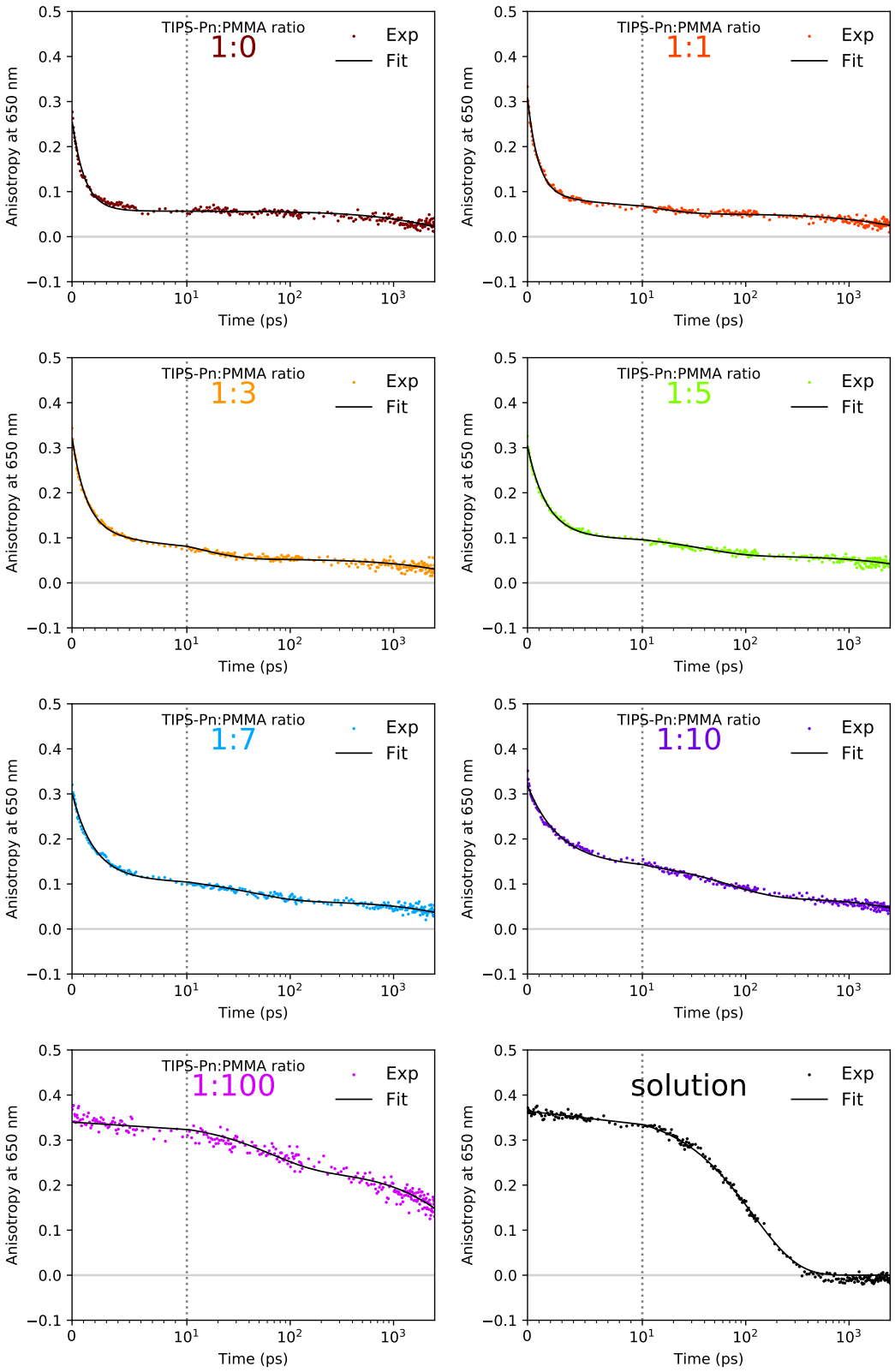

Figure S25: Experimental TA anisotropy at 650 nm for all TIPS-Pn:PMMA NPs and TIPS-Pn in THF. All data were fit to a sum of exponentials with parameters given in Table S11. The dotted grey lines indicate a change from a linear to logarithmic scale.

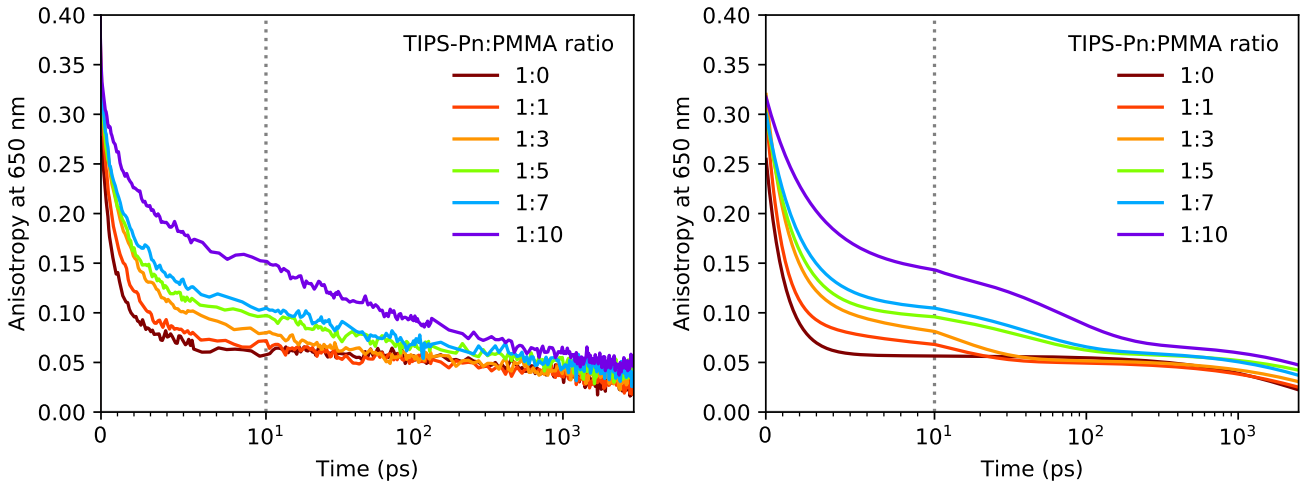

Figure S26: Experimental (left) and fitted (right) TA anisotropy at 650 nm for TIPS-Pn:PMMA NPs. The dotted grey lines indicate a change from a linear to logarithmic scale.

Pensack et al. measured the TA anisotropy decay of the GSB feature of TIPS-Pn NPs and other NPs of pentacene derivatives. The GSB anisotropy decay of their TIPS-Pn NPs seeming to be consistent with our neat 1:0 NP sample. The aim of their anisotropy measurements was purely to differentiate between the morphology of their NPs. NPs displaying a rapid anisotropy decay were explained to have little long-range order. NPs with a slower anisotropy decay, however, had extensive long-range solid-state order, as energy migration in an ordered system is expected to involve transition dipole moments that are aligned.[S32]

Although significant evidence suggests our NPs to be amorphous, we cannot conclude that the TIPS-Pn molecules were evenly dispersed within our NPs. As singlet migration occurs through a FRET mechanism, the singlet migration rate depends on the distance between chromophores (refer to Equations S10 and S11). As clustering results in a larger proportion of neighbours with a shorter distance from the initially excited chromophore, an increased singlet migration rate, and thus a faster initial anisotropy decay, would be expected compared to a random distribution of TIPS-Pn molecules. To test whether TIPS-Pn molecules were clustered in our NPs, the fluorescence anisotropy dynamics of random and clustered distributions were compared.

S3.8.3 Trends in the Transient Absorption Anisotropy at 508 nm

The TA anisotropy of the TIPS-Pn:PMMA NP samples at 508 nm is presented in Figure S27. These data were also fit to a sum of exponentials, with parameters given in Table S12. At 508 nm ΔA is mainly due to ESA, namely from singlet and triplet absorptions.

First, we note the TA anisotropy at 508 nm has a negative amplitude. The negative anisotropy is due to ΔA at 508 nm consisting of excited-state contributions from both singlet and triplet excitons. The transition dipole moments of the singlet and triplet ESA ($S_1 \rightarrow S_n$ and $T_1 \rightarrow T_n$) are both perpendicular to the $S_0 \rightarrow S_1$ transition,[S24,S26,S27] as illustrated in Figure S28. This means that singlet and triplet ESA result in a 90° rotation in the detected polarisation relative to the initial excitation polarisation. Therefore, the initial anisotropy value would be -0.2, if there was no loss in polarisation during the initial excitation and the detection of the TA anisotropy at this wavelength. However, the direction of the transition dipole moment of the ESA may change due to vibronic coupling to higher states that changes as vibrational and spin relaxation occurs.[S35] This

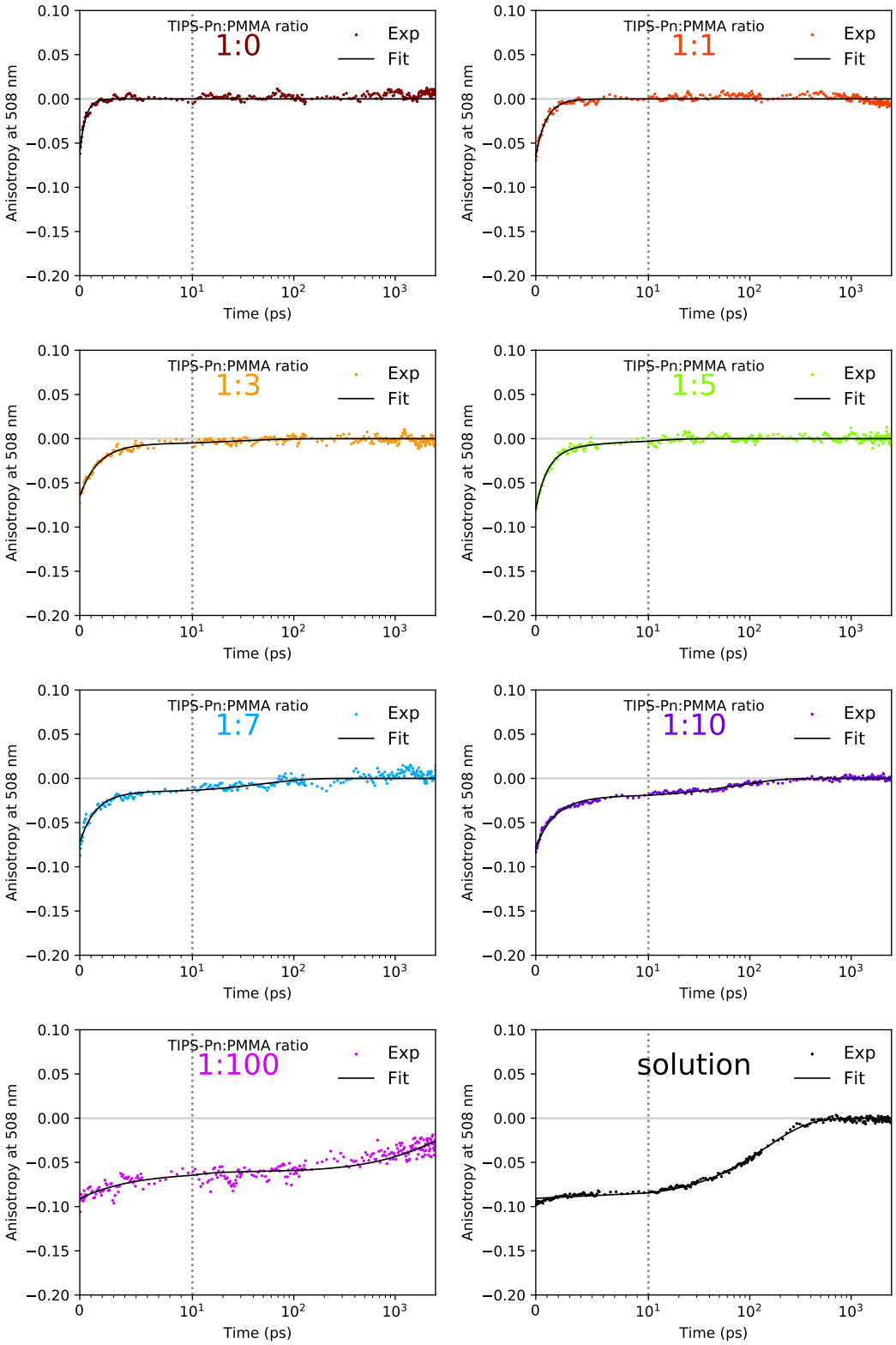

Figure S27: Experimental TA anisotropy at 508 nm for all TIPS-Pn:PMMA NPs and TIPS-Pn in THF. All data were fit to a sum of exponentials with parameters given in Table S12. The dotted grey lines indicate a change from a linear to logarithmic scale.

Table S12: Fitting parameters for the TA anisotropy data at 508 nm of TIPS-Pn:PMMA NPs and TIPS-Pn in THF.[a]

Sample	A_1[b]	τ_1 (ps)	A_2	τ_2 (ps)
1:0	-1.00±0.09	0.51±0.08	-	-
1:1	-1.00±0.05	0.94±0.09	-	-
1:3	-0.90±0.05	1.6±0.2	-0.10±0.05	31±28
1:5	-0.8±0.1	1.0±0.2	-0.2±0.1	6±3
1:7	-0.77±0.05	1.4±0.3	-0.23±0.05	49±28
1:10	-0.72±0.02	1.7±0.1	-0.28±0.01	74±8
1:100	-0.33±0.04	5±2	-0.67±0.02	2900±200
solution	-1.000±0.005	143±3	-	-

[a] Unconstrained parameters are shown with a 90% confidence interval. [b] Normalised amplitudes.

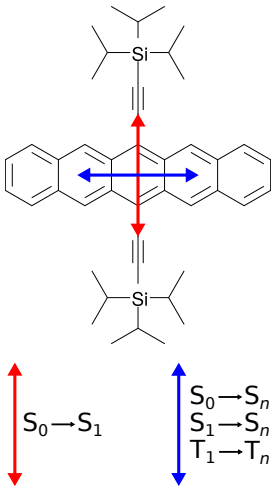

Figure S28: The various transition dipole moment directions of TIPS-Pn.[S24,S26,S27]

would then result in excited-state transition dipole moments not being exactly perpendicular to the $S_0 \rightarrow S_1$ transition, and thus result in a lower (in magnitude) initial anisotropy than expected. However, as stated previously, this should not affect the anisotropy decay dynamics.

The negative TA anisotropy observed in our NPs at 508 nm is consistent with a previous study on pentacene. McDonough et al. performed the first TA measurements on pentacene,[S36] observing a negative anisotropy at 507 nm and 545 nm. McDonough et al. argued that a negative anisotropy is consistent with pumping the $S_0 \rightarrow S_1$ state and probing the triplet $T_1 \rightarrow T_3$ transition, as these dipole moments are perpendicular.[S36] They therefore use these anisotropy results to assign the 507 nm and 545 nm absorptions to the triplet transition. However, since the $S_1 \rightarrow S_n$ transition is also perpendicular to the $S_0 \rightarrow S_1$ transition,[S24,S26,S27] a negative anisotropy alone is not a valid basis on which to assign a transition to be purely due to triplets. Furthermore, the poor quality anisotropy data did not allow for any other analysis apart from the magnitude of the anisotropy.[S36]

We now comment on the trends of the TA anisotropy at 508 nm. The 1:0 and 1:1 samples can be fit with a single exponential, while the rest are fit with two exponentials. These results are summarised in Table S12. The short time constant, τ_1, is ∼1 ps and it increases as the proportion of

PMMA is increased, while the corresponding amplitude decreases. Correspondingly, the amplitude of the longer time constant, τ_2, increases. The results show that the TA anisotropy at 508 nm decays faster for NP samples with a shorter average intermolecular TIPS-Pn separation, as highlighted in Figure S29.

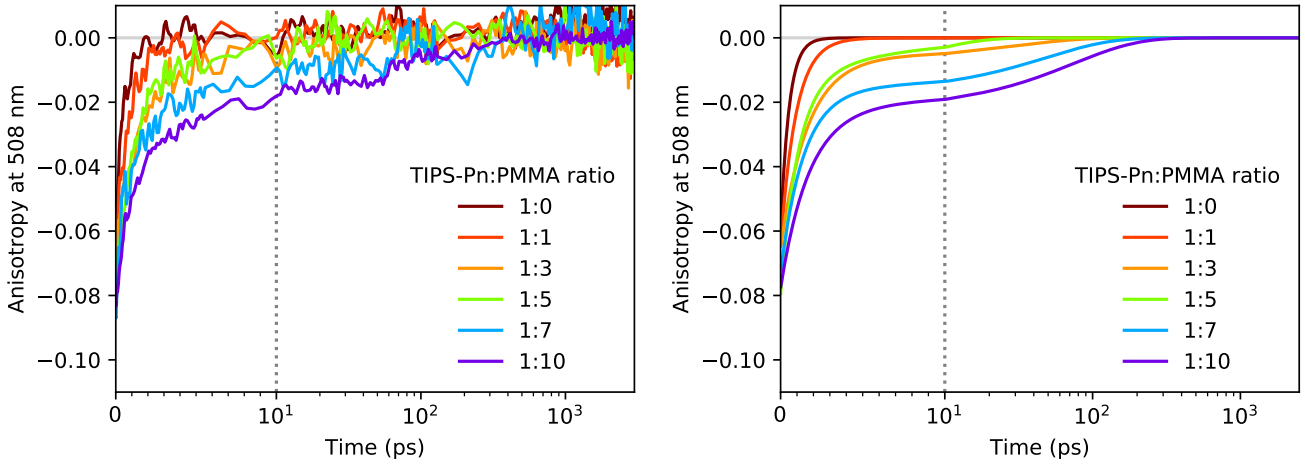

Figure S29: Experimental (left) and fitted (right) TA anisotropy at 508 nm for TIPS-Pn:PMMA NPs. The dotted grey lines indicate a change from a linear to logarithmic scale.

Unlike the fluorescence anisotropy and the TA anisotropy at 650 nm, the TA anisotropy at 508 nm decays to zero within the timescale of the experiment. This is due to the lower initial anisotropy amplitude at 508 nm, corresponding to an already slightly depolarised system, and so the time taken to reach an anisotropy value of zero (corresponding to a completely depolarised system) is faster. An anisotropy value of zero means ΔA has lost all correlation with the initial excitation polarisation. Consequently, no long time component exists, and any further depolarisation (e.g. from slow singlet or triplet migration) would not be observed at this wavelength.

The τ_1 value is slightly lower than that at 650 nm for a given NP sample. It is evident that the ΔA depolarisation rate is different at these two wavelengths (650 nm versus 508 nm). This is due to different components affecting these wavelengths, each causing a different contribution to the depolarisation. In an attempt to obtain TA anisotropy decays associated with a single species only, we turn towards measurements in the NIR region, where the singlet and triplet features are more clearly separated.

S3.8.4 NIR Transient Absorption Anisotropy

The overlapping contributions from the GSB, SE and ESA in the visible spectral region have been discussed. In the NIR region there are no influences from the GSB or SE. Therefore, analysis of the spectrum is relatively straightforward. From the magic-angle TA data presented in Figure S17, we assigned the wavelength at 1350 nm to singlet absorption, and the wavelength at 990 nm to have mainly a triplet (but also some singlet) contribution. Obtaining NIR TA anisotropy data may therefore make analysis of exciton migration straightforward as the TA anisotropy at 1350 nm and 990 nm is a representation of the singlet and triplet depolarisation, respectively.

Figure S30 displays the anisotropy decay of the fluorescence (at 655 nm) and TA (at 990 nm and 1350 nm) for $\sim 10^{-4}$ M TIPS-Pn in THF. All data were fit to a single exponential, with parameters given in Table S13. The same information is displayed for the 1:10 sample in Figure S31 and

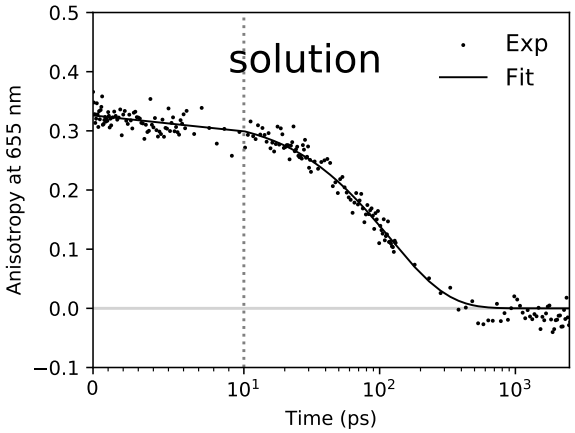

(a)

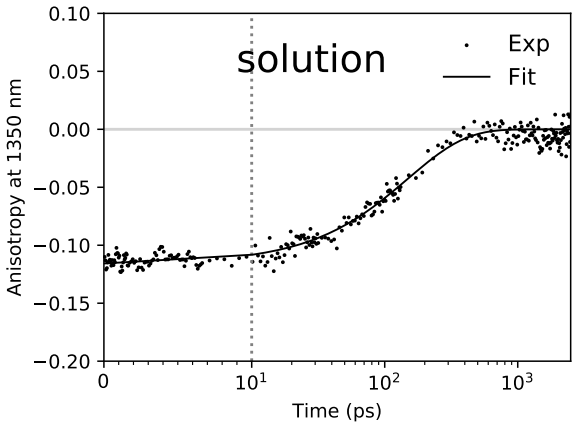

(b)

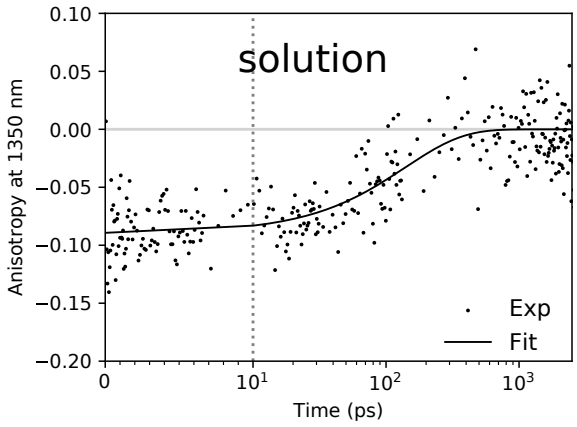

(c)

Figure S30: Experimental and fitted **(a)** fluorescence anisotropy, **(b)** TA anisotropy at 1350 nm and **(c)** TA anisotropy at 990 nm, for $\sim 10^{-4}$ M TIPS-Pn in THF. The dotted grey lines indicate a change from a linear to logarithmic scale.

Table S14, where the data are fit to a sum of two exponentials. The short time constant, τ_1, for the TA anisotropy at 1350 nm fits well when fixed to τ_1 of the fluorescence anisotropy data. The time constants and amplitudes of the fluorescence anisotropy and TA anisotropy at 1350 nm, are the same, within error, for each sample. This suggests that there are no major contributions from other species at 1350 nm, confirming that ΔA at 1350 nm is mainly due to singlets.

As mentioned previously, the ΔA at 990 nm is mostly due to triplets, but a small proportion of singlets also contribute to this wavelength. The TA anisotropy of the TIPS-Pn in THF sample at 990 nm showed similar kinetics to that at 1350 nm. As this sample did not undergo SF, the 990 nm TA anisotropy decay is also a representation of singlet depolarisation. However, the TA anisotropy at 990 nm is significantly lower in quality than that at 1350 nm due to a lower ΔA signal amplitude. For the 1:10 sample, an attempt to analyse the TA anisotropy kinetics at 990 nm was made in order to obtain the anisotropy decay due to triplets. However, nearly all correlation is lost at this wavelength at early times, and so triplet migration cannot be analysed using this signal.

The loss of polarisation anisotropy at 990 nm can be explained as follows. Fast singlet migration to SF sites results in depolarisation, and then SF results in two triplets. Only one of these

Table S13: Fitting parameters for the fluorescence anisotropy and TA anisotropy data at 1350 nm of $\sim 10^{-4}$ M TIPS-Pn in THF.[a]

Sample	A_1[b]	τ_1
Solution (Fluorescence)	1.000±0.008	118±4
Solution (TA at 1350 nm)	-1.00±0.01	150±7
Solution (TA at 990 nm)	-1.00±0.05	140±32

[a] Unconstrained parameters are shown with a 90% confidence interval. [b] Normalised amplitudes.

triplets (the one previously in the S_1 state) may possibly still display a slight correlation to the initial excitation, while the other (previously a ground-state molecule), would show no correlation assuming SF has no orientational dependence. The combination of triplets resulting from already depolarised singlets and one of the formed triplets showing no correlation, results in a close to zero anisotropy at early times.

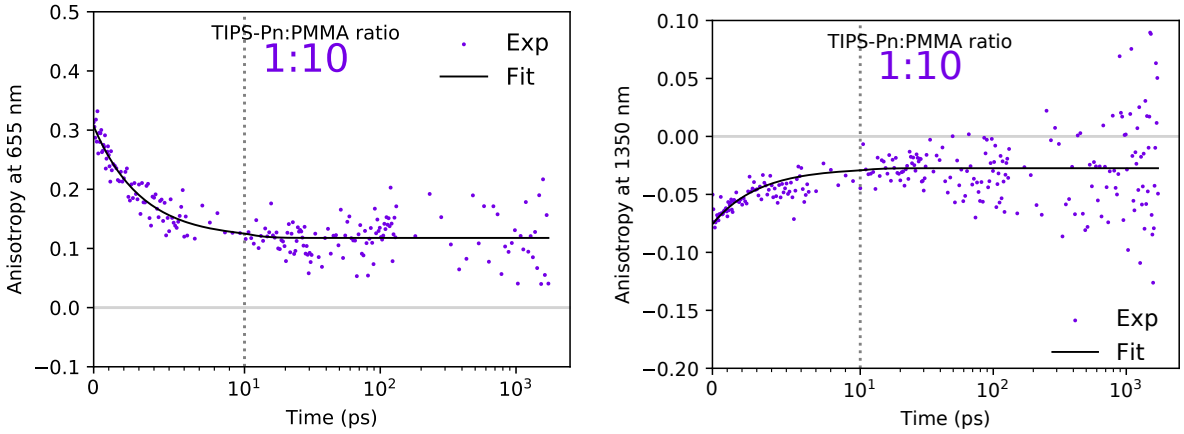

(a) **(b)**

Figure S31: Experimental and fitted **(a)** fluorescence anisotropy and **(b)** TA anisotropy at 1350 nm, for the 1:10 TIPS-Pn:PMMA NPs. The dotted grey lines indicate a change from a linear to logarithmic scale.

Table S14: Fitting parameters for the fluorescence anisotropy and TA anisotropy data at 1350 nm of 1:10 TIPS-Pn:PMMA NPs.[a]

Sample	A_1[b]	τ_1 (ps)	A_2	τ_2[‡] (ps)
1:10 (Fluorescence)	0.62±0.05	3.1±0.5	0.39±0.01	∞
1:10 (TA at 1350 nm)	-0.6±0.2	3.1[†]	-0.36±05	∞

[a] Unconstrained parameters are shown with a 90% confidence interval. [b] Normalised amplitudes. [†] Fixed time constant. [‡] $\tau_2 \rightarrow \infty$ indicates a constant offset in the time-resolved curve.

S3.9 Monte Carlo Simulations

S3.9.1 Simulated Steady-state Absorption and Emission Spectra

The singlet migration rate depends on the spectral overlap between the donor and acceptor, calculated by integrating over the product of the emission spectrum of the donor and absorption spectrum of the acceptor.

The steady-state absorption and emission spectra of the TIPS-Pn molecules were simulated by a Franck-Condon progression (Equation S21 with parameters in Table S7). The simulated steady-state absorption spectrum was generated by summing over the absorption spectra of all TIPS-Pn molecules. The simulated steady-state fluorescence spectrum was generated by summing over only those that decay during the MC simulation.

Figure S32 shows the simulated and experimental steady-state absorption and fluorescence spectra of the 1:10 TIPS-Pn:PMMA NPs. The characteristic 0–0 and 0–1 transitions, along with the distinct vibrational features, are well represented by the MC simulation.

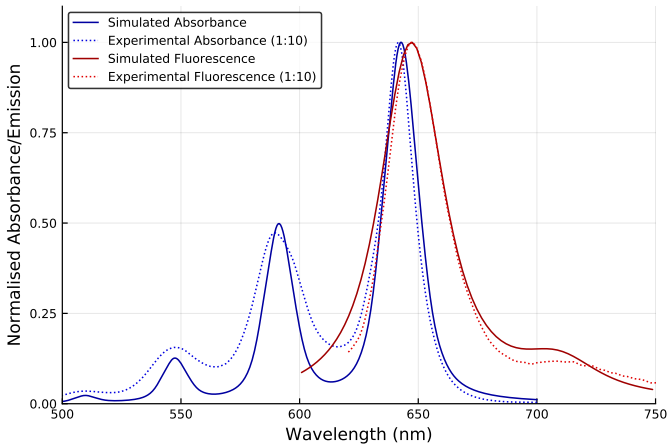

Figure S32: Experimental and simulated steady-state absorption and fluorescence emission for the 1:10 TIPS-Pn:PMMA NPs. Section S2.7 contains a detailed description of the method employed to obtain the simulated data.

S3.9.2 Simulation of Random TIPS-Pn Distributions

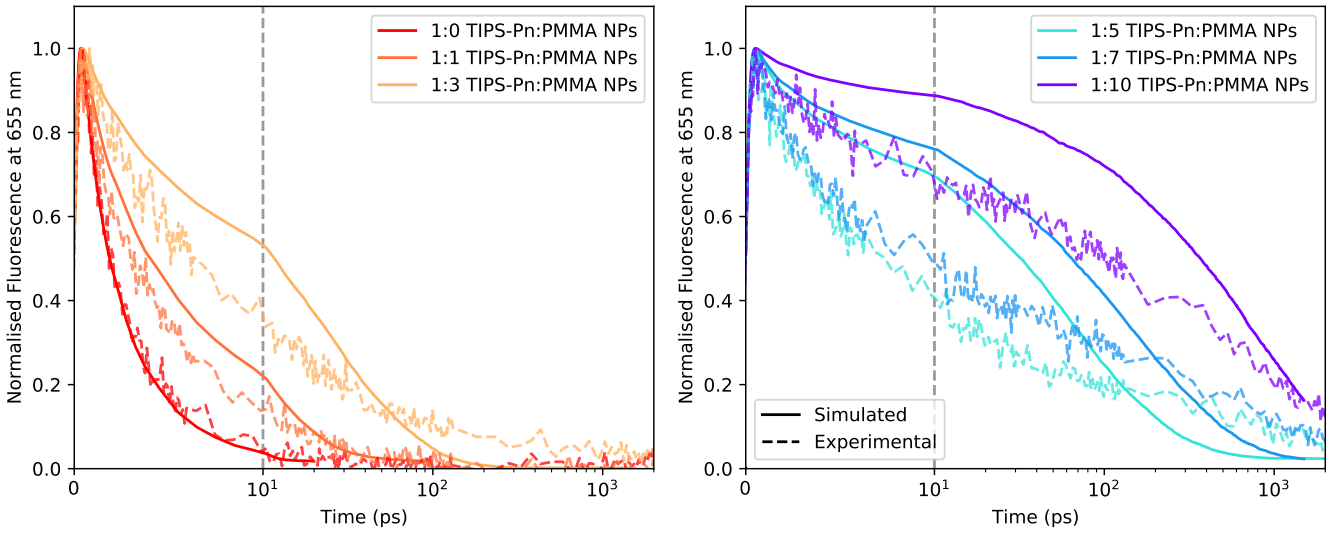

Figure S33: Experimental and simulated magic-angle fluorescence data for various TIPS-Pn:PMMA NPs. The simulated data was obtained assuming a random distribution of TIPS-Pn molecules, with $r_{SF} = 0.7\,\text{nm}$ and $k_{SF} = 4.5 \times 10^{11}\,\text{s}^{-1}$. The dotted grey lines indicate a change from a linear to logarithmic scale.

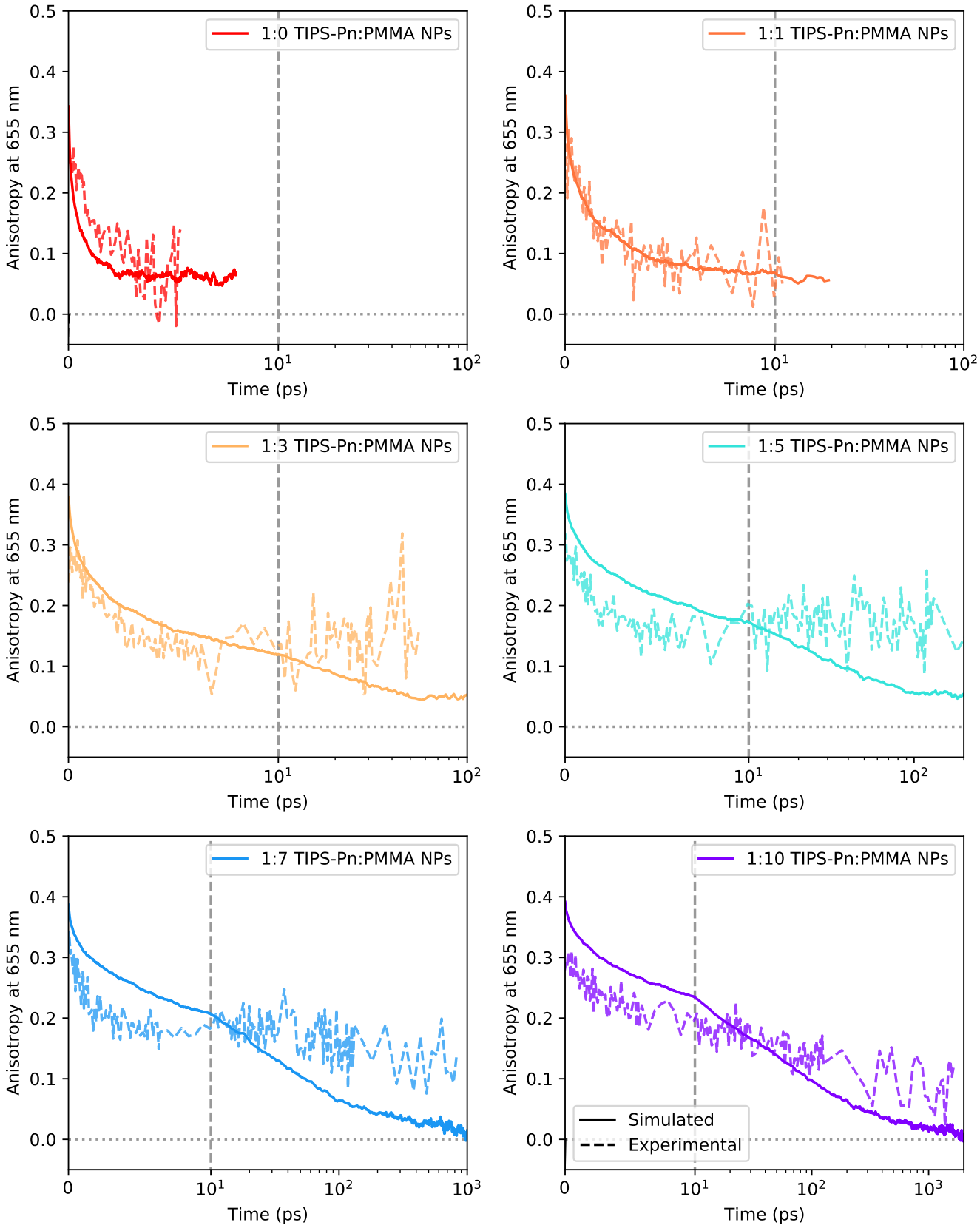

Figure S34: Experimental and simulated time-resolved fluorescence anisotropy for various TIPS-Pn:PMMA NPs. The simulated data was obtained assuming a random distribution of TIPS-Pn molecules, with $r_{SF} = 0.7\,\text{nm}$ and $k_{SF} = 4.5 \times 10^{11}\,\text{s}^{-1}$. The dotted grey vertical lines indicate a change from a linear to logarithmic time scale.

S3.9.3 Simulation of Clustered TIPS-Pn Distributions

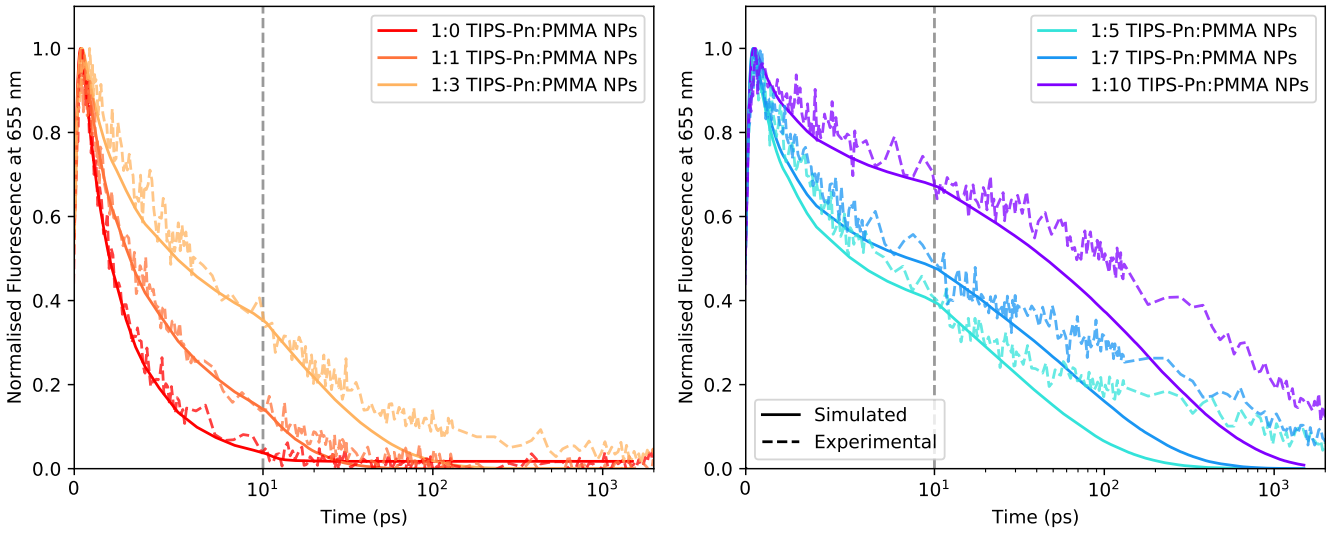

Figure S35: Experimental and simulated magic-angle fluorescence data for various TIPS-Pn:PMMA NPs. The simulated data was obtained assuming a clustered distribution of TIPS-Pn molecules, with $r_{SF} = 0.7\,\text{nm}$ and $k_{SF} = 4.5 \times 10^{11}\,\text{s}^{-1}$. The dotted grey vertical lines indicate a change from a linear to logarithmic time scale.

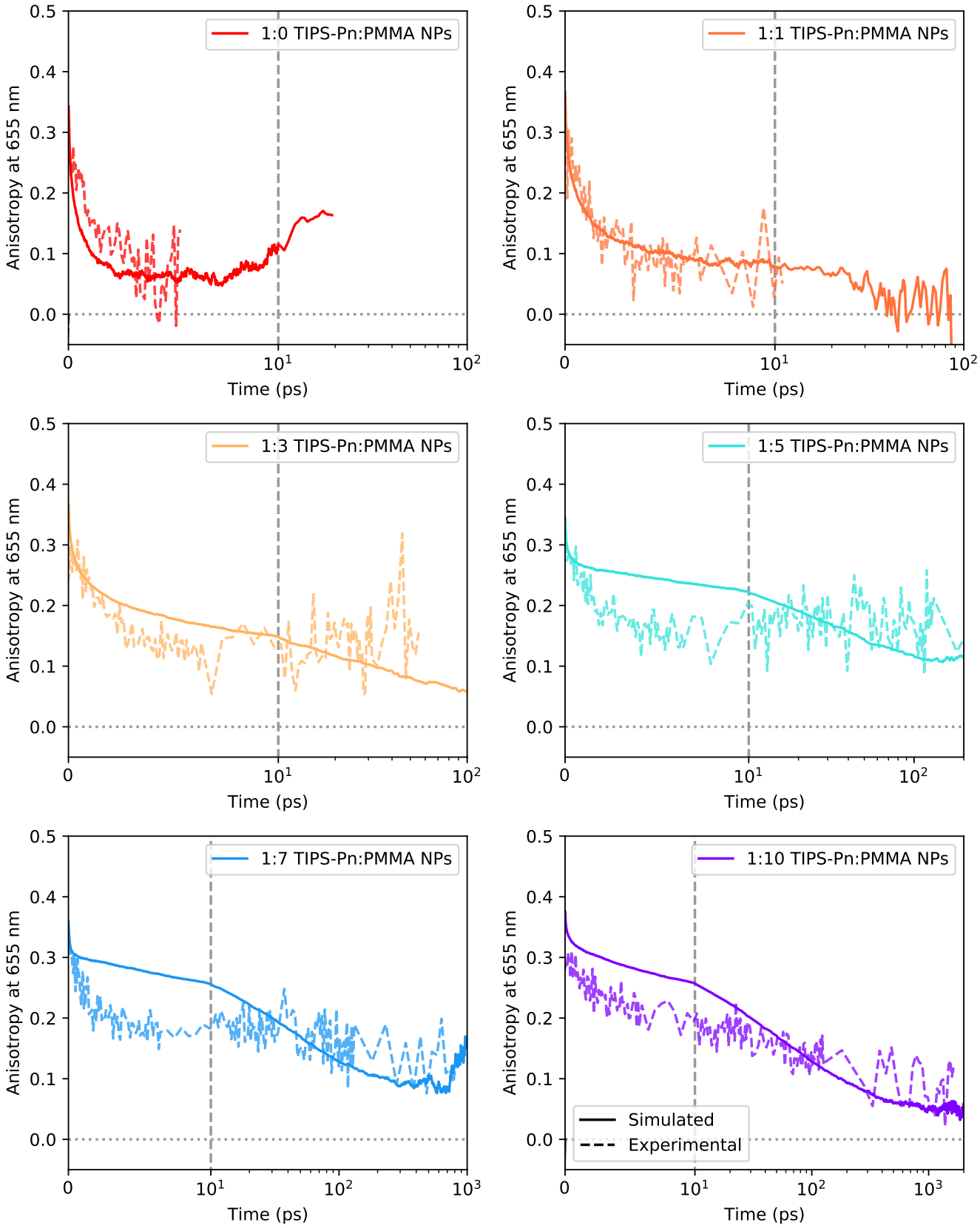

Figure S36: Experimental and simulated time-resolved fluorescence anisotropy for various TIPS-Pn:PMMA NPs. The simulated data was obtained assuming a clustered distribution of TIPS-Pn molecules, with $r_{SF} = 0.7\,\text{nm}$ and $k_{SF} = 4.5 \times 10^{11}\,\text{s}^{-1}$. The dotted grey vertical lines indicate a change from a linear to logarithmic time scale.

S3.9.4 Simulation of Clustered TIPS-Pn Distributions with Traps Sites

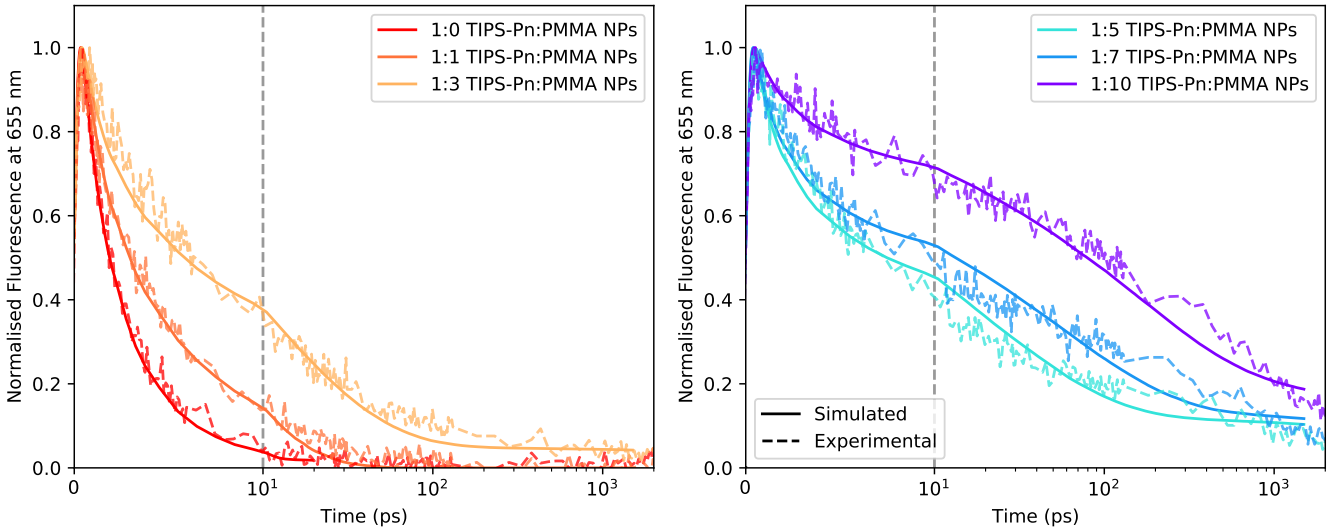

Figure S37: Experimental and simulated magic-angle fluorescence data for various TIPS-Pn:PMMA NPs. The simulated data was obtained assuming a clustered distribution of TIPS-Pn molecules, a percentage of trap sites as described in the main text, $r_{SF} = 0.7\,\text{nm}$, and $k_{SF} = 4.5 \times 10^{11}\,\text{s}^{-1}$. The dotted grey vertical lines indicate a change from a linear to logarithmic time scale.

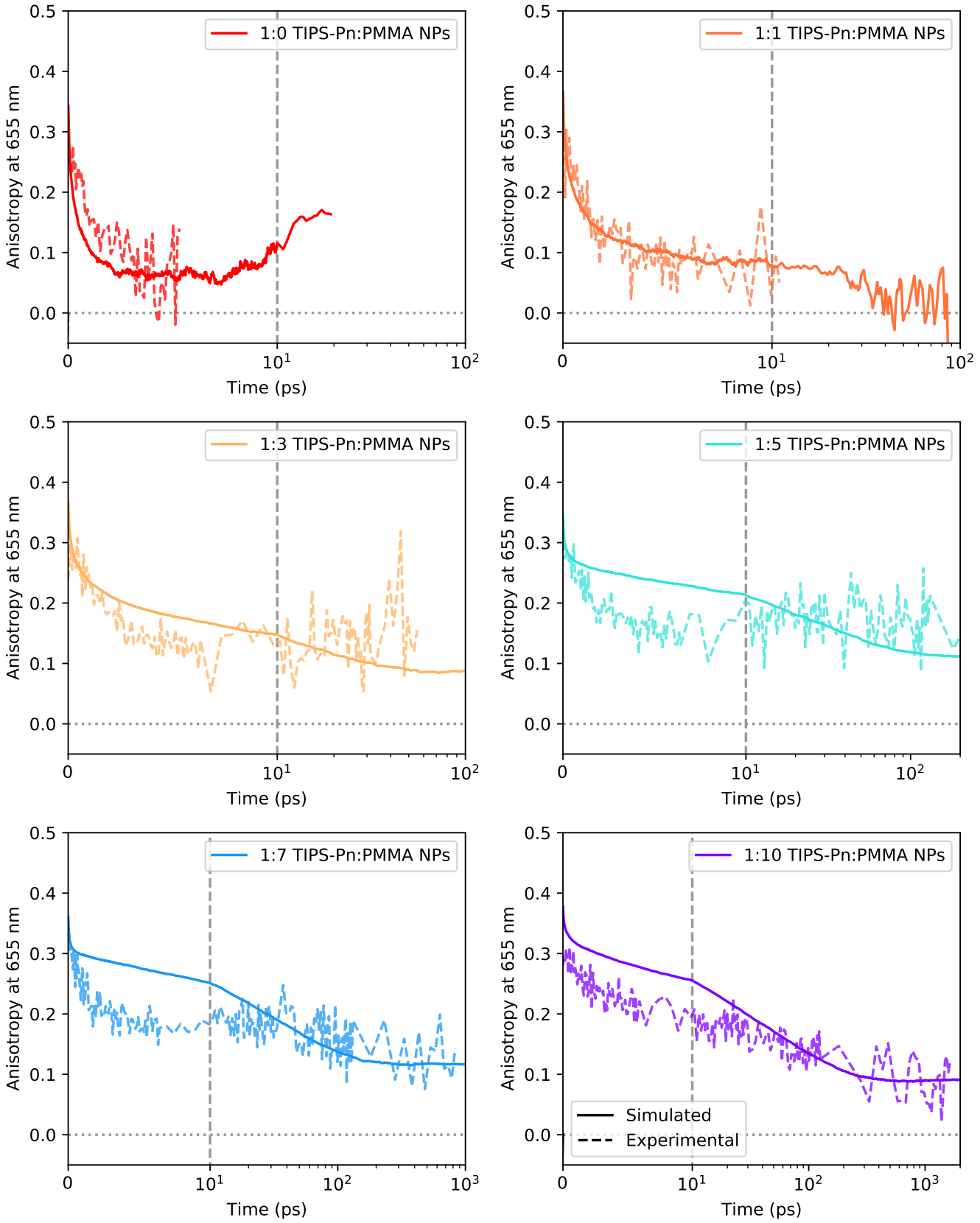

Figure S38: Experimental and simulated time-resolved fluorescence anisotropy for various TIPS-Pn:PMMA NPs. The simulated data was obtained assuming a clustered distribution of TIPS-Pn molecules, a percentage of trap sites as described in the main text, $r_{SF} = 0.7\,\text{nm}$,and $k_{SF} = 4.5 \times 10^{11}\,\text{s}^{-1}$. The dotted grey vertical lines indicate a change from a linear to logarithmic time scale.

S3.9.5 Voronoi Analysis of the TIPS-Pn Molecules in the TIPS-Pn:PMMA Nanoparticles

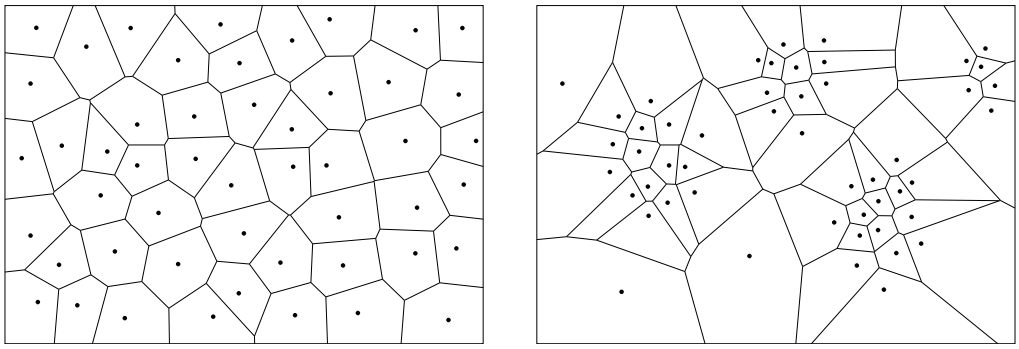

Figure S39: Voronoi diagrams for a random (left) and clustered (right) TIPS-Pn distribution, where TIPS-Pn are represented as points. Note that this diagram is a 2D representation of the three-dimensional (3D) NP system. Although the average Voronoi volume is equal for both distributions, the *distributions* of Voronoi volumes are different. The system with a random TIPS-Pn distribution has Voronoi volumes which can be described by a normal distribution. The system with a clustered TIPS-Pn distribution has a Voronoi volume distribution with a larger number of smaller volumes and consequently also a higher proportion of larger volumes than the random TIPS-Pn distribution. These different distributions are evident in Figure S40.

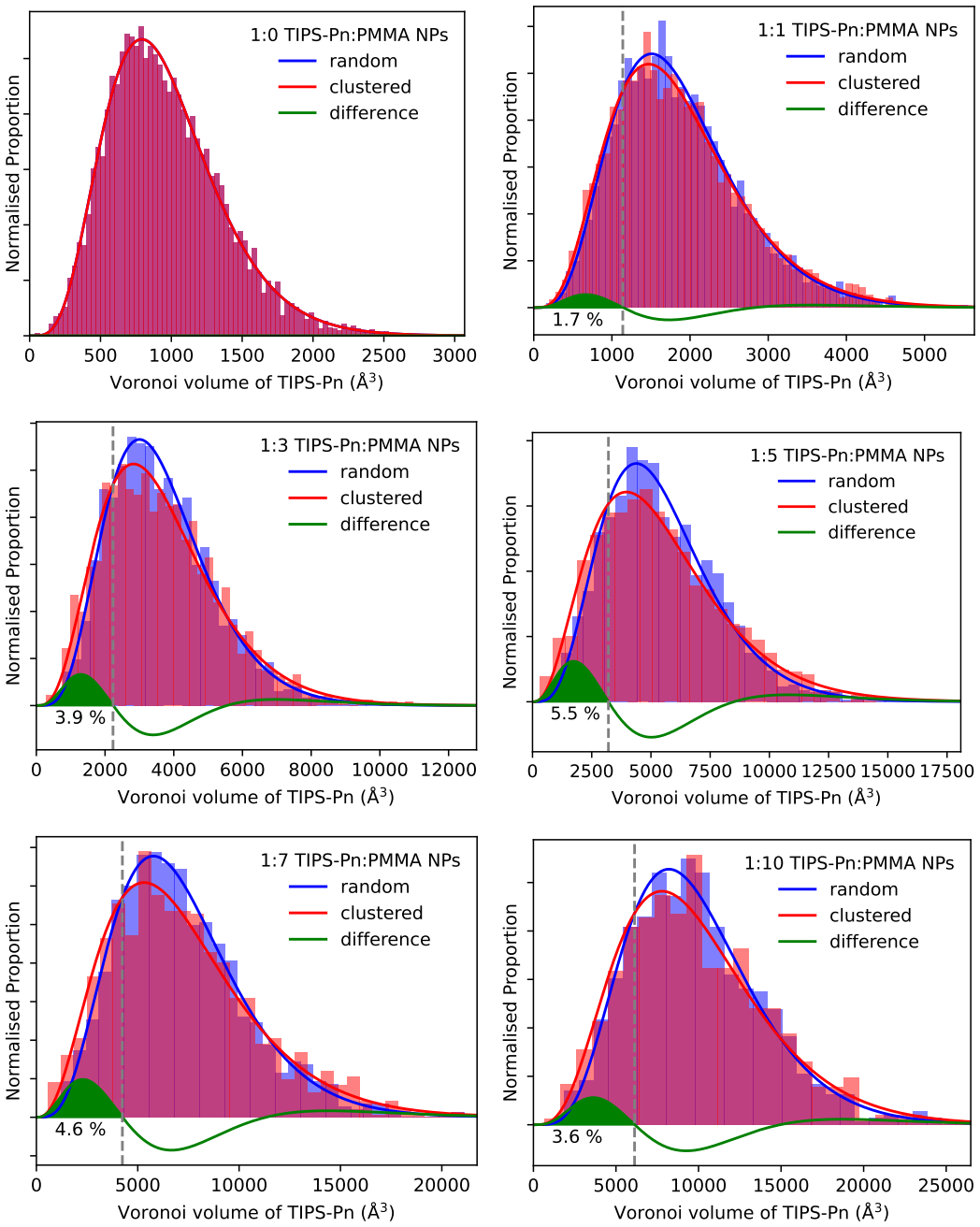

Figure S40: Voronoi analysis of the TIPS-Pn molecules in the TIPS-Pn:PMMA NPs. The random distribution for each NP sample was taken from the MD simulation just after energy minimisation and the clustered distribution taken at a timestep corresponding to the best MC simulated fit to the experimental fluorescence data. TIPS-Pn molecules were considered "clustered" if they were not likely to belong to the random distribution. This was calculated by integrating the difference between the clustered and randomly distributed curves from 0 up to v_{thresh} (dashed grey line), as indicated by the green shaded area.

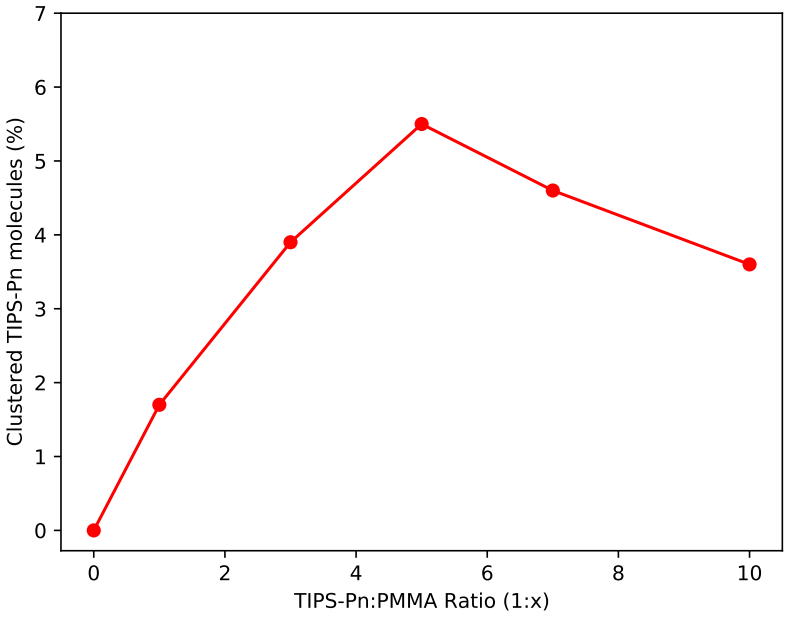

Figure S41: The percentage of TIPS-Pn molecules which were required to be "clustered" within each of the TIPS-Pn:PMMA NP systems in order for the MC simulation to fit the experimental data. TIPS-Pn molecules were considered "clustered" if they were not likely to belong to the random distribution.

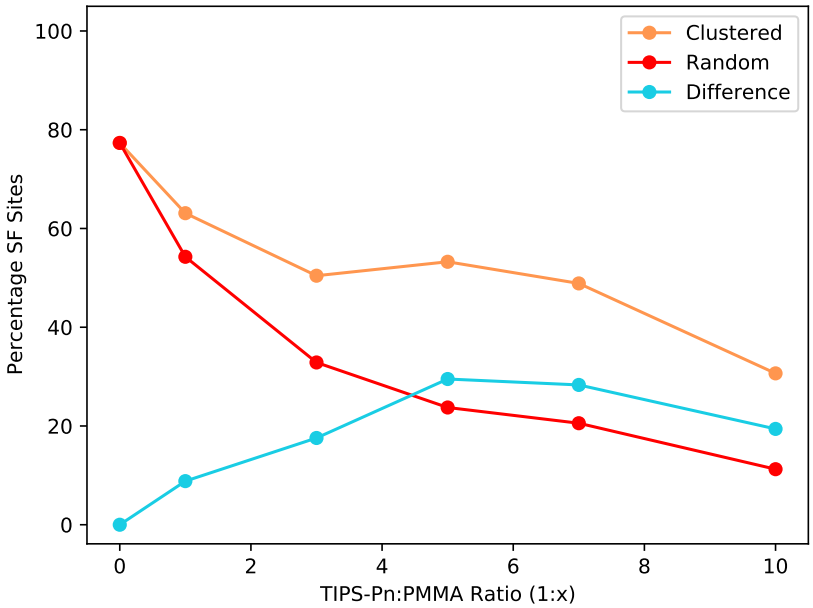

Figure S42: The percentage of SF sites for each of the TIPS-Pn:PMMA NPs for random and clustered TIPS-Pn distributions. A chromophore was considered to be a "SF site" if it had another chromophore within 0.7 nm of it (as $r_{\mathrm{SF}} = 0.7\,\mathrm{nm}$ is used in the MC simulation).

S3.9.6 Number and Size of TIPS-Pn Clusters

To quantify the number and size of TIPS-Pn clusters in the random and clustered distributions, the clustering algorithm DBSCAN was used[S37]. DBSCAN takes two input parameters, ϵ and n. n is the minimum number of molecules in a cluster, and ϵ is a distance parameter that determines how close points need to be to be considered part of the same cluster. A molecule belongs to a cluster if it is within ϵ of another molecule in that cluster. We considered the effect of clustering on the number of TIPS-Pn molecules with a neighbour within the SF radius $r_{\mathrm{SF}} = \epsilon = 0.7\,\mathrm{nm}$, with $n = 2$. Hence, all molecules that were considered part of a cluster were able to undergo SF. Figure S43 shows the distribution of cluster sizes in the input geometries for the MC simulation with either a random or clustered distribution of TIPS-Pn. In the random geometry most clusters were ≤ 6 molecules in size, with a shift to lower cluster sizes observed for lower TIPS-Pn amounts. At this ϵ and n, the clustered geometries showed a modest but general increase in cluster size compared to the random geometries.

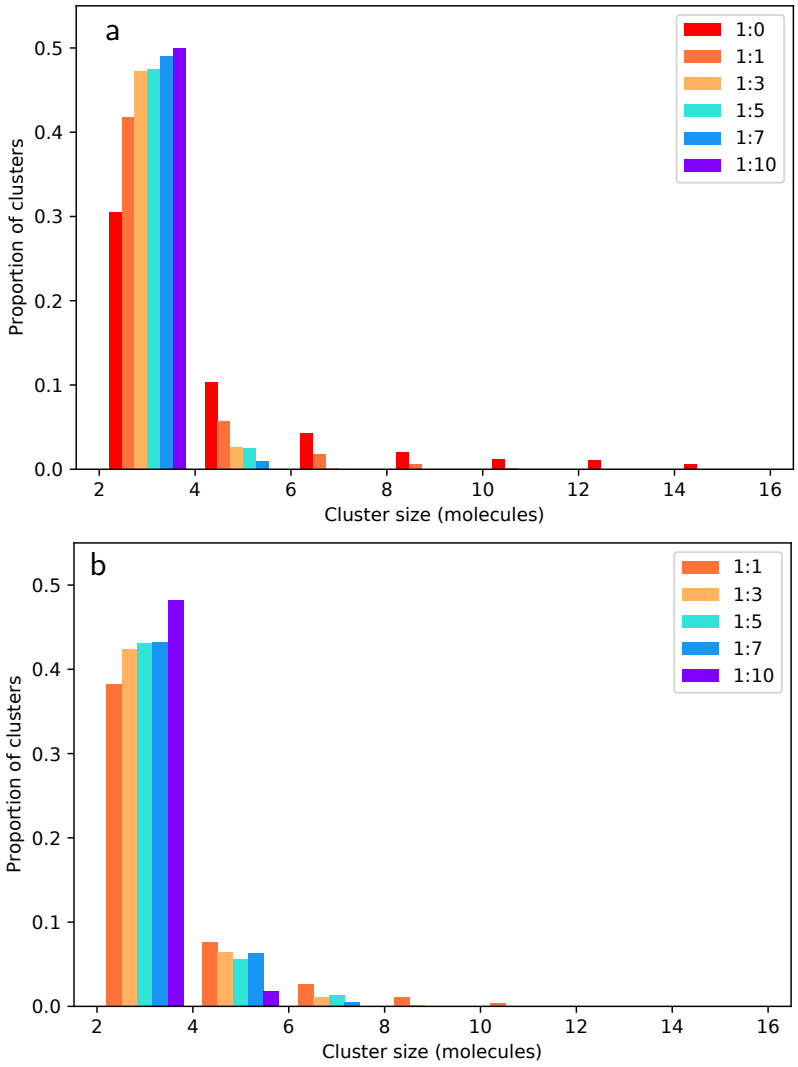

Figure S43: Histograms showing the number of clusters of various sizes generated by analysis with DBSCAN for (a) random and (b) clustered distributions ($\epsilon = 0.7$, $n = 2$).

By plotting the proportion of molecules assigned to clusters, we could quantify the proportion of

TIPS-Pn molecules that had a neighbour within r_{SF}, which were hence capable of SF (Figure S44). This analysis produced results equivalent to Figure S42, and again demonstrated that clustering increases the proportion of molecules capable of SF, particularly for the NPs with less TIPS-Pn. Hence, clustering the TIPS-Pn molecules resulted in both a modest increase in cluster size and an increase in the number of clustered molecules compared to the random geometry, which increased the proportion of TIPS-Pn molecules which were considered "SF sites".

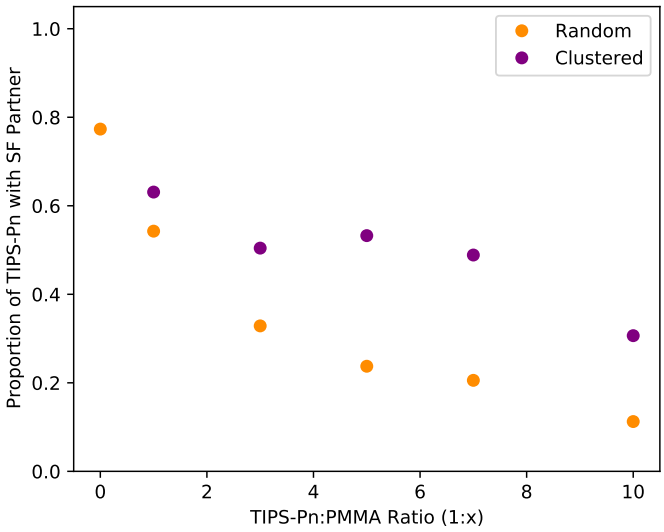

Figure S44: Proportion of TIPS-Pn molecules with a neighbour within 0.7 nm ("SF sites") as a function of TIPS-Pn:PMMA mass ratio in the random and clustered geometries. For the 1:0 ratio the clustered and random geometries were equivalent.

S3.9.7 Singlet Fission Rate with Exponential Dependence on Distance

The simulated results presented in the main text used a simple Heaviside step function to model the dependence of the SF rate on the separation between chromophore pairs. The SF rate was constant ($k_{SF} = 4.5 \times 10^{11}$ s^{-1}) for pairs separated by up to $r_{SF} = 0.7$ nm and zero otherwise. An alternative model is a SF rate that has an exponential dependence on the pair separation,

$$k_{SF}^{D,A} = k_{SF_0} e^{-\beta r^{D,A}}, \tag{S25}$$

where $r^{D,A}$ is the distance between the pair of molecules undergoing SF. This model takes two parameters: k_{SF_0}, which controls the amplitude of the SF rate, and β, which controls how quickly the SF rate drops as the distance between the pair increases. Although the Heaviside SF rate model with the clustered TIPS-Pn geometry was able to replicate the experimental data quite well, the exponential model may provide more physically meaningful information about the rate and distance scale of SF. To determine if the exponential model could be used replicate the experimental data, a range of k_{SF_0} and β were trialled for fitting the 1:10 TIPS-Pn:PMMA time-resolved fluorescence with clustered input geometries and no traps sites. Some examples of the best sets of k_{SF_0} and β are shown in Figure S45. However, the exponential model with these parameters did not produce an acceptable fit to the experimental fluorescence, and generally performed worse than the Heaviside model (Figure S45). Hence, this form of exponential distance dependence does not accurately reflect the SF rate in TIPS-Pn:PMMA NPs.

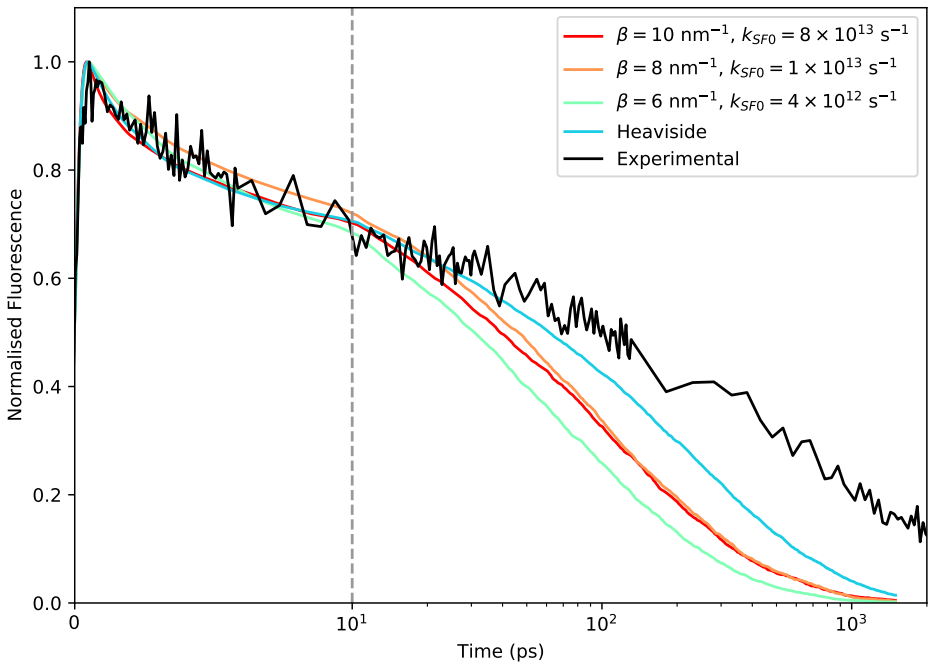

Figure S45: Time-resolved fluorescence of 1:10 TIPS-Pn:PMMA NPs at 655 nm, compared with the output of the MC simulation with the Heaviside SF rate model and the exponential SF rate model.

S4 Calculations

S4.1 Mass Ratio of TIPS-Pn and PMMA

The mass ratio of TIPS-Pn and PMMA and their respective densities can be used to calculate various properties of our NPs.

We define:
$m_{\text{TIPS-Pn}}$ and m_{PMMA} as the average mass of TIPS-Pn and PMMA, respectively, in a NP.
$m_{\text{NP}} = m_{\text{TIPS-Pn}} + m_{\text{PMMA}}$ as the average total mass of a NP.
$V_{\text{TIPS-Pn}}$ and V_{PMMA} as the average volume of TIPS-Pn and PMMA, respectively, in a NP.
$V_{\text{NP}} = V_{\text{TIPS-Pn}} + V_{\text{PMMA}}$ as the average total volume of a NP.
$\rho_{\text{TIPS-Pn}}$ and ρ_{PMMA} as the density of TIPS-Pn and PMMA, respectively.
ρ_{NP} as the average total density of a NP.
$N_{\text{TIPS-Pn}}$ as the average number of TIPS-Pn molecules in a NP.
$c_{\text{TIPS-Pn}}$ as the average concentration of TIPS-Pn in a NP.
$n_{\text{TIPS-Pn}}$ as the average number of moles of TIPS-Pn in a NP.
$MW_{\text{TIPS-Pn}}$ as the molecular weight of TIPS-Pn.
N_A as Avogadro's number.

For a NP sample with a TIPS-Pn:PMMA mass ratio of 1:α,

$$m_{\text{PMMA}} = \alpha m_{\text{TIPS-Pn}}. \tag{S26}$$

S4.2 Average Voronoi Volume of TIPS-Pn in a NP

To define some average distance between TIPS-Pn molecules, we first define a volume around each TIPS-Pn such that no other particles are in this volume. This is illustrated as a Voronoi diagram in Figure S46. We envision TIPS-Pn as points, and define regions of volume around each TIPS-Pn for which any point within this volume is closest to that specific TIPS-Pn molecule.

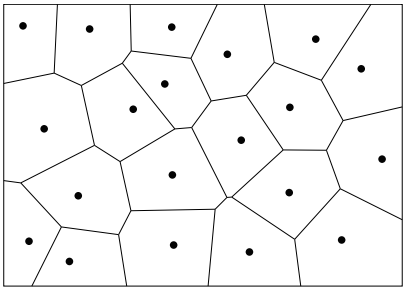

Figure S46: Voronoi diagram for a system with randomly distributed TIPS-Pn molecules represented by points. Note that this diagram is a 2D representation of the 3D NP system.

The average Voronoi volume for a TIPS-Pn, $V_{V_{\text{TIPS-Pn}}}$, is equal to the sum of all Voronoi volumes (i.e. the total volume of the NP, V_{NP}) divided by the number of TIPS-Pn molecules in the NP, $N_{\text{TIPS-Pn}}$.

$$\begin{aligned} V_{V_{\text{TIPS-Pn}}} &= \frac{V_{\text{NP}}}{N_{\text{TIPS-Pn}}} \\ &= \frac{\frac{m_{\text{NP}}}{\rho_{\text{NP}}}}{\frac{m_{\text{TIPS-Pn}}}{MW_{\text{TIPS-Pn}}} N_A} \\ &= \frac{m_{\text{NP}} MW_{\text{TIPS-Pn}}}{\rho_{\text{NP}} m_{\text{TIPS-Pn}} N_A} \end{aligned} \tag{S27}$$

Making use of Equation S26,

$$\begin{aligned} V_{V_{\text{TIPS-Pn}}} &= \frac{(1+\alpha) m_{\text{TIPS-Pn}} MW_{\text{TIPS-Pn}}}{\rho_{\text{NP}} m_{\text{TIPS-Pn}} N_A} \\ &= \frac{(1+\alpha) MW_{\text{TIPS-Pn}}}{\rho_{\text{NP}} N_A}. \end{aligned} \tag{S28}$$

We must now find the total density of the NP, ρ_{NP}, which is given by

$$\begin{aligned} \rho_{\text{NP}} &= \frac{m_{\text{NP}}}{V_{\text{NP}}} \\ &= \frac{m_{\text{TIPS-Pn}} + m_{\text{PMMA}}}{V_{\text{TIPS-Pn}} + V_{\text{PMMA}}} \\ &= \frac{m_{\text{TIPS-Pn}} + m_{\text{PMMA}}}{\frac{m_{\text{TIPS-Pn}}}{\rho_{\text{TIPS-Pn}}} + \frac{m_{\text{PMMA}}}{\rho_{\text{PMMA}}}} \\ &= \frac{m_{\text{TIPS-Pn}} + m_{\text{PMMA}}}{\frac{m_{\text{TIPS-Pn}} \rho_{\text{PMMA}} + m_{\text{PMMA}} \rho_{\text{TIPS-Pn}}}{\rho_{\text{TIPS-Pn}} \rho_{\text{PMMA}}}}. \end{aligned}$$

Again, using Equation S26,

$$\rho_{\text{NP}} = \frac{(1+\alpha)m_{\text{TIPS-Pn}}}{\frac{m_{\text{TIPS-Pn}}\rho_{\text{PMMA}}+\alpha m_{\text{TIPS-Pn}}\rho_{\text{TIPS-Pn}}}{\rho_{\text{TIPS-Pn}}\rho_{\text{PMMA}}}}$$

$$\therefore \rho_{\text{NP}} = \frac{(1+\alpha)\rho_{\text{TIPS-Pn}}\rho_{\text{PMMA}}}{\rho_{\text{PMMA}}+\alpha\rho_{\text{TIPS-Pn}}}. \tag{S29}$$

Substituting Equation S29 into S28 gives

$$V_{V_{\text{TIPS-Pn}}} = \frac{(1+\alpha)MW_{\text{TIPS-Pn}}}{\left(\frac{(1+\alpha)\rho_{\text{TIPS-Pn}}\rho_{\text{PMMA}}}{\rho_{\text{PMMA}}+\alpha\rho_{\text{TIPS-Pn}}}\right)N_A}$$

$$\therefore V_{V_{\text{TIPS-Pn}}} = \frac{(\rho_{\text{PMMA}}+\alpha\rho_{\text{TIPS-Pn}})MW_{\text{TIPS-Pn}}}{\rho_{\text{TIPS-Pn}}\rho_{\text{PMMA}}N_A}. \tag{S30}$$

S4.3 Average Intermolecular TIPS-Pn Separation in a NP

As working in average volumes is confusing, we aimed to convert this volume into an average distance. For simplicity, we consider all TIPS-Pn molecules to be placed in a 3D cubic lattice structure, with each TIPS-Pn contained in a simple cubic unit cell (refer to Figure S47). Then the length of the side of each cell, d, is what we define as the "average intermolecular TIPS-Pn separation". Therefore,

$$d^3 = V_{V_{\text{TIPS-Pn}}}$$

$$d = \sqrt[3]{V_{V_{\text{TIPS-Pn}}}}. \tag{S31}$$

The average Voronoi volume can be used to calculate a different definition of average intermolecular TIPS-Pn separation, by assuming a different positional distribution of TIPS-Pn molecules within a NP.

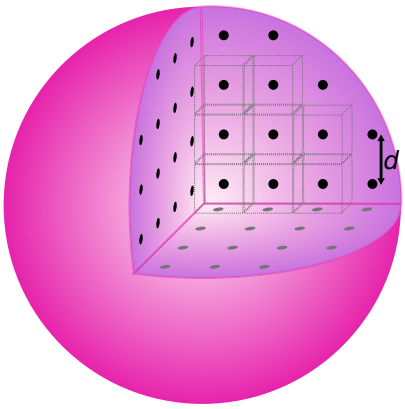

Figure S47: Evenly spaced TIPS-Pn molecules (represented by points) inside a NP. Each molecule can be surrounded by a cube of width d (where d is termed the "average intermolecular TIPS-Pn separation"). This means the TIPS-Pn molecules are surrounded by a volume of d^3, which we call the "average Voronoi volume" of TIPS-Pn within a NP.

S4.4 Average Concentration of TIPS-Pn in a NP

Although the TIPS-Pn concentration in all samples was ∼100 ppm (refer to Table S1), we wanted a measure of an average concentration of TIPS-Pn within a NP, $c_{\text{TIPS-Pn}}$, which is given by

$$\begin{aligned} c_{\text{TIPS-Pn}} &= \frac{n_{\text{TIPS-Pn}}}{V_{\text{NP}}} \\ &= \frac{N_{\text{TIPS-Pn}}}{N_A V_{\text{NP}}}. \end{aligned}$$

Now substituting for V_{NP} using Equation S27,

$$\begin{aligned} c_{\text{TIPS-Pn}} &= \frac{N_{\text{TIPS-Pn}}}{N_A N_{\text{TIPS-Pn}} V_{V_{\text{TIPS-Pn}}}} \\ &= \frac{1}{N_A V_{V_{\text{TIPS-Pn}}}}. \end{aligned} \tag{S32}$$

Or alternatively, if we use our definition of the average intermolecular TIPS-Pn separation, d,

$$c_{\text{TIPS-Pn}} = \frac{1}{N_A d^3}. \tag{S33}$$

S4.5 Summary of Equations

We summarise all useful equations here:

The average Voronoi volume of a TIPS-Pn molecule in a NP

$$V_{V_{\text{TIPS-Pn}}} = \frac{(\rho_{\text{PMMA}} + \alpha\rho_{\text{TIPS-Pn}})}{\rho_{\text{TIPS-Pn}}\rho_{\text{PMMA}}} \frac{MW_{\text{TIPS-Pn}}}{N_A} \tag{S34}$$

The "average intermolecular TIPS-Pn separation"

$$d = \sqrt[3]{V_{V_{\text{TIPS-Pn}}}} \tag{S35}$$

The average concentration of TIPS-Pn within a NP

$$c_{\text{TIPS-Pn}} = \frac{1}{V_{V_{\text{TIPS-Pn}}}} \frac{1}{N_A} \tag{S36}$$

where
α is the given by the $1 : \alpha$ TIPS-Pn:PMMA mass ratio
$\rho_{\text{TIPS-Pn}} = 1104\,\text{g}\,\text{L}^{-1}$
$\rho_{\text{PMMA}} = 1188\,\text{g}\,\text{L}^{-1}$
$MW_{\text{TIPS-Pn}} = 639.07\,\text{g}\,\text{mol}^{-1}$
$N_A = 6.022 \times 10^{23}\,\text{mol}^{-1}$

We now have all relevant information to determine the average Voronoi volume of TIPS-Pn molecules in our NPs, the average intermolecular TIPS-Pn separation and the average concentration of TIPS-Pn within a NP (refer to Table S15).

Table S15: Average Voronoi volume of TIPS-Pn, average intermolecular TIPS-Pn separation and average concentration of TIPS-Pn in a NP, determined for each TIPS-Pn:PMMA NP sample (calculated using Equations S34 and S35, S36).

Sample (TIPS-Pn:PMMA mass ratio ($1:\alpha$))	**Average Voronoi volume of TIPS-Pn,** (nm^3)	**Average intermolecular TIPS-Pn separation, d,** (nm)	**Average concentration of TIPS-Pn in a NP** ($\mathrm{mol\,L^{-1}}$)
1:0	0.96	0.99	1.73
1:1	1.85	1.23	0.90
1:3	3.64	1.54	0.46
1:5	5.43	1.76	0.31
1:7	7.21	1.93	0.23
1:10	9.89	2.15	0.17
1:100	90.29	4.49	0.02

S4.6 Estimation of Rotational Correlation Time

The rotational correlation time, τ_c, of a sphere is the average time for it to rotate one radian, and is given by[S5]

$$\tau_c = \frac{\eta V}{RT} = \frac{\eta(\frac{4}{3}\pi r^3)}{RT}, \tag{S37}$$

where η is the viscosity, T is temperature, R is the gas constant, V is the volume of the rotating unit and r is the radius of the rotating unit.

S4.6.1 TIPS-Pn Molecules

TIPS-Pn molecules can be considered to be around 1.2 nm long (refer to Figure S5). Using the viscosity of THF, $4.8 \times 10^{-4}\,\mathrm{Pa\,s}$, we estimate the rotational correlation time of TIPS-Pn molecules to be

$$\begin{aligned}\tau_c &= \frac{4.8 \times 10^{-4}\,\mathrm{Pa\,s}\ (\frac{4}{3}\pi(0.6 \times 10^{-9}\,\mathrm{m})^3)}{8.314\,\mathrm{m^3\,Pa\,K^{-1}\,mol^{-1}} \times 294\,\mathrm{K}} \times 6.022 \times 10^{23}\,\mathrm{mol^{-1}} \\ &\approx 108\,\mathrm{ps}\end{aligned}$$

S4.6.2 Nanoparticles

The NPs have been found to have a diameter of >40 nm.[S10] Using the viscosity of water, $8.90 \times 10^{-4}\,\mathrm{Pa\,s}$, we estimate the rotational correlation time of our NPs to be

$$\begin{aligned}\tau_c &= \frac{8.90 \times 10^{-4}\,\mathrm{Pa\,s}\ (\frac{4}{3}\pi(20 \times 10^{-9}\,\mathrm{m})^3)}{8.314\,\mathrm{m^3\,Pa\,K^{-1}\,mol^{-1}} \times 294\,\mathrm{K}} \times 6.022 \times 10^{23}\,\mathrm{mol^{-1}} \\ &\approx 7\,\mu\mathrm{s}\end{aligned}$$

Using a NP radius of 20 nm gives a lower bound on this correlation time. This is significantly larger than the 3 nanosecond time window of the anisotropy measurements, so the rotation of TIPS-Pn molecules can be assumed to have negligible effect on the anisotropy of the NP samples.

S5 Experimental Data Sets and Simulation Code

The experimental data, plus simulation code and inputs are available online at:

`https://universityofadelaide.box.com/v/Schrefl2022-Source-Material`.

References

(S1) Tapping, P. C.; Kee, T. W. Optical Pumping of Poly(3-hexylthiophene) Singlet Excitons Induces Charge Carrier Generation. *J. Phys. Chem. Lett.* **2014**, *5*, 1040–1047.

(S2) Harada, T.; McTernan, H. L.; Pham, D.-T.; Lincoln, S. F.; Kee, T. W. Femtosecond Transient Absorption Spectroscopy of the Medicinal Agent Curcumin in Diamide Linked γ-Cyclodextrin Dimers. *J. Phys. Chem. B* **2015**, *119*, 2425–2433.

(S3) Tapping, P. C.; Roseli, R. B.; Kee, T. W. Liberation of Charge Carriers by Optical Pumping Excitons in Poly(3-hexylthiophene) Aggregates. *J. Phys. Chem. C* **2018**, *123*, 3441–3448.

(S4) Stuart, A. N.; Tapping, P. C.; Schrefl, E.; Huang, D. M.; Kee, T. W. Controlling the Efficiency of Singlet Fission in TIPS-Pentacene/Polymer Composite Nanoparticles. *J. Phys. Chem. C* **2019**, *123*, 5813–5825.

(S5) Lakowicz, J. R. *Principles of Fluorescence Spectroscopy*, 3rd ed.; Springer US, 2006.

(S6) Tapping, P. C.; Clafton, S. N.; Schwarz, K. N.; Kee, T. W.; Huang, D. M. Molecular-Level Details of Morphology-Dependent Exciton Migration in Poly(3-hexylthiophene) Nanostructures. *J. Phys. Chem. C* **2015**, *119*, 7047–7059.

(S7) Torii, H. Time-Domain Calculations of the Polarized Raman Spectra, the Transient Infrared Absorption Anisotropy, and the Extent of Delocalization of the OH Stretching Mode of Liquid Water. *J. Phys. Chem. A* **2006**, *110*, 9469–9477.

(S8) Schalk, O.; Brands, H.; Balaban, T. S.; Unterreiner, A.-N. Near-Infrared Excitation of the Q Band in Free Base and Zinc Tetratolyl-porphyrins. *J. Phys. Chem. A* **2008**, *112*, 1719–1729.

(S9) Berera, R.; van Grondelle, R.; Kennis, J. T. M. Ultrafast Transient Absorption Spectroscopy: Principles and Application to Photosynthetic Systems. *Photosynth. Res.* **2009**, *101*, 105–118.

(S10) Hudson, R. J.; Stuart, A. N.; de la Perrelle, J. M.; Huang, D. M.; Kee, T. W. Nanoparticle Size-Dependent Singlet Fission and Exciton Dynamics in Amorphous TIPS-Pentacene. *J. Phys. Chem. C* **2021**, *125*, 21559–21570.

(S11) Mark, J. E., Ed. *Polymer Data Handbook*; Oxford University Press, Inc., 1999.

(S12) Kim, C. H.; Yaghmazadeh, O.; Tondelier, D.; Jeong, Y. B.; Bonnassieux, Y.; Horowitz, G. Capacitive Behavior of Pentacene-based Diodes: Quasistatic Dielectric Constant and Dielectric Strength. *J. Appl. Phys.* **2011**, *109*, 083710.

(S13) Vaklev, N. L.; Müller, R.; Muir, B. V. O.; James, D. T.; Pretot, R.; van der Schaaf, P.; Genoe, J.; Kim, J.; Steinke, J. H. G.; Campbell, A. J. HighPerformance Flexible BottomGate Organic FieldEffect Transistors with Gravure Printed Thin Organic Dielectric. *Adv. Mater. Interfaces* **2014**, *1*, 1300123.

(S14) Izadnia, S.; Schonleber, D. W.; Eisfeld, A.; Ruf, A.; LaForge, A. C.; Stienkemeier, F. Singlet Fission in Weakly Interacting Acene Molecules. *J. Phys. Chem. Lett* **2017**, *8*, 2068–2073.

(S15) Barford, W.; Bittner, E. R.; Ward, A. Exciton Dynamics in Disordered Poly(p-phenylenevinylene). 2. Exciton Diffusion. *J. Phys. Chem. A* **2012**, *116*, 10319–10327.

(S16) Yamagata, H.; Norton, J.; Hontz, E.; Olivier, Y.; Beljonne, D.; Brédas, J. L.; Silbey, R. J.; Spano, F. C. The Nature of Singlet Excitons in Oligoacene Molecular Crystals. *J. Chem. Phys.* **2011**, *134*, 204703.

(S17) Pensack, R. D.; Tilley, A. J.; Grieco, C.; Purdum, G. E.; Ostroumov, E. E.; Granger, D. B.; Oblinsky, D. G.; Dean, J. C.; Doucette, G. S.; Asbury, J. B.; Loo, Y.-L.; Seferos, D. S.; Anthony, J. E.; Scholes, G. D. Striking the Right Balance of Intermolecular Coupling for High-efficiency Singlet Fission. *Chem. Sci.* **2018**, *9*, 6240–6259.

(S18) Grieco, C.; Kennehan, E. R.; Kim, H.; Pensack, R. D.; Brigeman, A. N.; Rimshaw, A.; Payne, M. M.; Anthony, J. E.; Giebink, N. C.; Scholes, G. D.; Asbury, J. B. Direct Observation of Correlated Triplet Pair Dynamics during Singlet Fission Using Ultrafast Mid-IR Spectroscopy. *J. Phys. Chem. C* **2018**, *122*, 2012–2022.

(S19) Walker, B. J.; Musser, A. J.; Beljonne, D.; Friend, R. H. Singlet Exciton Fission in Solution. *Nat. Chem.* **2013**, *5*, 1019–1024.

(S20) Hudson, R. J.; de la Perrelle, J. M.; Pensack, R. D.; Kudisch, B.; Scholes, G. D.; Huang, D. M.; Kee, T. W. Organizing Crystalline Functionalized Pentacene Using Periodicity of Poly(Vinyl Alcohol). *J. Phys. Chem. Lett.* **2020**, 516–523.

(S21) Hudson, R. J.; Huang, D. M.; Kee, T. W. Anisotropic Triplet Exciton Diffusion in Crystalline Functionalized Pentacene. *J. Phys. Chem. C* **2020**, *124*, 23541–23550.

(S22) Pensack, R. D.; Grieco, C.; Purdum, G. E.; Mazza, S. M.; Tilley, A. J.; Ostroumov, E. E.; Seferos, D. S.; Loo, Y.-L.; Asbury, J. B.; Anthony, J. E.; Scholes, G. D. Solution-processable, Crystalline Material for Quantitative Singlet Fission. *Mater. Horiz.* **2017**, *4*, 915–923.

(S23) James, D. T.; Frost, J. M.; Wade, J.; Nelson, J.; Kim, J.-S. Controlling Microstructure of Pentacene Derivatives by Solution Processing: Impact of Structural Anisotropy on Optoelectronic Properties. *ACS Nano* **2013**, *7*, 7983–7991.

(S24) Wu, Y.; Liu, K.; Liu, H.; Zhang, Y.; Zhang, H.; Yao, J.; Fu, H. Impact of Intermolecular Distance on Singlet Fission in a Series of TIPS Pentacene Compounds. *J. Phys. Chem. Lett.* **2014**, *5*, 3451–3455.

(S25) Thorley, K. J.; Finn, T. W.; Jarolimek, K.; Anthony, J. E.; Risko, C. Theory-Driven Insight into the Crystal Packing of Trialkylsilylethynyl Pentacenes. *Chem. Mater.* **2017**, *29*, 2502–2512.

(S26) Folie, B. D.; Haber, J. B.; Refaely-Abramson, S.; Neaton, J. B.; Ginsberg, N. S. Long-Lived Correlated Triplet Pairs in a π-Stacked Crystalline Pentacene Derivative. *J. Am. Chem. Soc.* **2018**, *140*, 2326–2335.

(S27) Wan, Y.; Guo, Z.; Zhu, T.; Yan, S.; Johnson, J.; Huang, L. Cooperative Singlet and Triplet Exciton Transport in Tetracene Crystals Visualized by Ultrafast Microscopy. *Nat. Chem.* **2015**, *7*, 785–792.

(S28) Ramanan, C.; Smeigh, A. L.; Anthony, J. E.; Marks, T. J.; Wasielewski, M. R. Competition between Singlet Fission and Charge Separation in Solution-Processed Blend Films of 6,13-Bis(triisopropylsilylethynyl)pentacene with Sterically-Encumbered Perylene-3,4:9,10-bis(dicarboximide)s. *J. Am. Chem. Soc.* **2012**, *134*, 386–397.

(S29) Smith, M. B.; Michl, J. Recent Advances in Singlet Fission. *Annu. Rev. Phys. Chem.* **2013**, *64*, 361–386.

(S30) Yost, S. R.; Lee, J.; Wilson, M. W. B.; Wu, T.; McMahon, D. P.; Parkhurst, R. R.; Thompson, N. J.; Congreve, D. N.; Rao, A.; Johnson, K.; Sfeir, M. Y.; Bawendi, M. G.; Swager, T. M.; Friend, R. H.; Baldo, M. A.; Voorhis, T. V. A Transferable Model for Singlet-Fission Kinetics. *Nat. Chem.* **2014**, *6*, 492–497.

(S31) Tayebjee, M. J. Y.; Schwarz, K. N.; MacQueen, R. W.; Dvořák, M.; Lam, A. W. C.; Ghiggino, K. P.; McCamey, D. R.; Schmidt, T. W.; Conibeer, G. J. Morphological Evolution and Singlet Fission in Aqueous Suspensions of TIPS-Pentacene Nanoparticles. *J. Phys. Chem. C* **2016**, *120*, 157–165.

(S32) Pensack, R. D.; Tilley, A. J.; Parkin, S. R.; Lee, T. S.; Payne, M. M.; Gao, D.; Jahnke, A. A.; Oblinsky, D. G.; Li, P.-F.; Anthony, J. E.; Seferos, D. S.; Scholes, G. D. Exciton Delocalization Drives Rapid Singlet Fission in Nanoparticles of Acene Derivatives. *J. Am. Chem. Soc.* **2015**, *137*, 6790–6803.

(S33) Dvořák, M.; Prasad, S. K. K.; Dover, C. B.; Forest, C. R.; Kaleem, A.; MacQueen, R. W.; Petty, A. J.; Forecast, R.; Beves, J. E.; Anthony, J. E.; Tayebjee, M. J. Y.; Widmer-Cooper, A.; Thordarson, P.; Schmidt, T. W. Singlet Fission in Concentrated TIPS-Pentacene Solutions: The Role of Excimers and Aggregates. *J. Am. Chem. Soc.* **2021**, *143*, 13749–13758.

(S34) Min, C.-K.; Joo, T.; Yoon, M.-C.; Kim, C. M.; Hwang, Y. N.; Kim, D.; Aratani, N.; Yoshida, N.; Osuka, A. Transient Absorption Anisotropy Study of Ultrafast Energy Transfer in Porphyrin Monomer, Its Direct Meso–meso Coupled Dimer and Trimer. *J. Chem. Phys.* **2001**, *114*, 6750–6758.

(S35) Wallin, S.; Davidsson, J.; Modin, J.; Hammarström, L. Femtosecond Transient Absorption Anisotropy Study on $[Ru(bpy)3]^{2+}$ and $[Ru(bpy)(py)4]^{2+}$. Ultrafast Interligand Randomization of the MLCT State. *J. Phys. Chem. A* **2005**, *109*, 4697–4704.

(S36) McDonough, T. J.; Zhang, L.; Roy, S. S.; Kearns, N. M.; Arnold, M. S.; Zanni, M. T.; Andrew, T. L. Triplet Exciton Dissociation and Electron Extraction in Graphene-templated Pentacene Observed with Ultrafast Spectroscopy. *Phys. Chem. Chem. Phys.* **2017**, *19*, 4809–4820.

(S37) Ester, M.; Kriegel, H.-P.; Sander, J.; Xu, X. A Density-Based Algorithm for Discovering Clusters in Large Spatial Databases with Noise. kdd. 1996; pp 226–231.